DESIGN AND FABRICATION OF SOLID STATE TiO_2|Ag STRUCTURE FOR DEVELOPING EFFICIENT PLASMONIC PHOTO - ELECTRIC CONVERSION DEVICE

A Thesis

Submitted in partial fulfilment of the requirements for the award of the degree

of

Doctor of Philosophy

by

Ksh Priyalakshmi Devi

(Roll no. 176151102)

School of Energy Science and Engineering

Indian Institute of Technology Guwahati,

Guwahati – 781039, Assam, India

March 2024

INDIAN INSTITUTE OF TECHNOLOGY GUWAHATI

School of Energy Science and Engineering

Guwahati – 781039

STATEMENT

I do hereby declare that the work incorporated in this thesis entitled, "**Design and fabrication of solid-state TiO_2|Ag structure for developing efficient plasmonic photo-electric conversion device**" is the result of investigations carried out by me in the School of Energy Science and Engineering, Indian Institute of Technology Guwahati, Assam, India under the guidance of (Late) Dr. Harsh Chaturvedi and Prof. Pranab Goswami.

In keeping with the general practice of reporting scientific observations, due acknowledgments have been made wherever the work described is based on the findings of other investigators. I further declare that this work has not been submitted in part or full to any other university or institute for the award of any degree or diploma.

Ksh. Priyalakshmi

Date: 05/03/2024 Ksh Priyalakshmi Devi

INDIAN INSTITUTE OF TECHNOLOGY GUWAHATI

School of Energy Science and Engineering

Guwahati – 781039

CERTIFICATE

This is to certify that the work included in this thesis entitled "**Design and fabrication of solid-state TiO_2|Ag structure for developing efficient plasmonic photo-electric conversion device**" by Ksh Priyalakshmi Devi (Roll No. 176151102) for the award of degree of Doctor of Philosophy is an authentic record of results obtained from the research work carried out under our supervision in School of Energy Science and Engineering, Indian Institute of Technology Guwahati, Assam, India.

The results embodied in this thesis have not been submitted to any other University or Institute for the award of any degree.

Prof. Pranab Goswami
School of Energy Science and Engineering &
Department of Biosciences and Engineering
Indian Institute of Technology Guwahati,
Guwahati – 781039, Assam, India

(Late) Dr. Harsh Chaturvedi
School of Energy Science and Engineering
Indian Institute of Technology Guwahati,
Guwahati – 781039, Assam, India

ACKNOWLEDGEMENT

It has been a wonderful experience for me during the entire span of my research work. Many people have inspired, motivated and helped me during the entire course of this work and it is my heartfelt desire to acknowledge their immense goodwill and valuable support.

I wish to express my sincere and deep appreciation to my supervisors, ***(Late)Dr. Harsh Chaturvedi and Prof. Pranab Goswami*** *for their unwavering support, invaluable guidance, and constant encouragement. I am especially thankful to them for critically reviewing the reports and research papers despite their busy academic and other administrative work schedules. Their expertise and dedication have been instrumental in shaping this research's direction and helping me navigate the challenges along the way. I owe them a lot for the valuable advice they have given me whenever I needed. I am deeply saddened by the untimely demise of Dr. Harsh Chaturvedi, and I offer my prayers for his soul to find eternal peace.*

I am also indebted to my doctoral committee members, ***Prof. V.V. Goud, Dr. Kalyan Raidongiya and Dr. Pankaj Kalita*** *for their insightful feedback, constructive criticism, and valuable contributions to this work. Their collective wisdom and expertise have enriched the quality of this thesis.*

Furthermore, I would like to express my sincere gratitude to ***Prof. P. K. Iyer*** *and* ***Prof. Pratima Agarwal*** *for allowing me to use their laboratory facilities to carry out my research experiments.*

I would like to express my sincere gratitude to present and former Heads, School of Energy Science and Engineering, Indian Institute of Technology Guwahati, for providing various laboratory facilities and sanctioning funds without which completion of the work would not have been possible. I am also grateful to all the faculty members and staff of the School of Energy Science and Engineering.

I would also like to thank the Ministry of Human Resource and Development (MHRD), Government of India for providing financial support. I sincerely thank Indian Institute of Technology Guwahati for providing all sorts of infrastructural facilities to carry out this research work. I would also like to acknowledge Centre of Excellence, BSBE, Centre for Nanotechnology and Central Instruments Facility of Indian Institute of Technology Guwahati

and all scientific officers and staff members for providing instruments and helping me to carry out the research work.

I deeply acknowledge the persistent support and counselling provided by my colleagues and friends Aparupa, Caroline, Debika, Dr. Deepika Bisnoi, Brijesh, Siddhart bhaiya, Jeet, Arup, Dr. Abdul Bhaiya, Dr. Priyanki Di, Dr. Lightson Ngasangva, Dr. Smita Das, Dr. Phurpa Di, Vinay and all other lab members throughout my studies.

I am also grateful to my friends and seniors, Dr. Sanasam Sunderlal, Dr. Th. Binota, Dr. Franco, Dr. Somorjit, Mr. Th. Birjit, Dr. Amit Kumar Rohit and Jaishree Bharadwaj for their constant support.

I extend heartfelt appreciation to my husband, ***Thingom Robichandra Singh*** *and our beloved daughter,* ***Thingom Chancynavya Devi*** *for their unwavering support and boundless love throughout the completion of this thesis. Their encouragement, patience, and presence have been instrumental in my journey, inspiring me to overcome challenges and strive for excellence. To my husband, thank you for your constant support and belief in me. To our precious baby, your laughter and innocence have brought immeasurable joy and motivation. Together, you have been my guiding lights, reminding me of the importance of perseverance and resilience. I am forever grateful for your love and encouragement.*

My most sincere gratitude and appreciation go to my father ***Mr. Ksh Sideswor Singh, and my mother Mrs. Ksh(o) Netalini Devi*** *for their patience, continuous encouragement and moral support over the past difficult years. I extend my heartfelt thanks to my brother* ***Ksh Satyaswor Singh*** *and all my other family members for their endless love, encouragement, and understanding. Their unwavering belief in me has been a constant source of motivation, and I am truly grateful for their support throughout my academic journey.*

Last, but not the least, I shall always be grateful to Almighty for providing me with such an awesome aura for research work.

Date: 05/03/2024 ***Ksh Priyalakshmi Devi***

TABLE OF CONTENTS

ABSTRACT

The habitat destruction and greenhouse effect caused by the acquisition and use of fossil fuels compelled the global research community to explore renewable green energy sources to safeguard that Mother Earth is habitable for lives. Over the last few decades, there has been a significant shift in energy research from non-renewable to renewable energy sources, with a major focus on solar energy through photovoltaic (PV) technology. However, converting a broad spectrum of sunlight, including near-infrared wavelengths, through PV is challenging. Traditional amorphous silicon solar cells are only efficient within 700 nm of wavelength, despite 40% of solar energy being in the longer-wavelength infrared region. Hence, there is an urge to explore more efficient technology, and one such promising technology is the plasmonic-based energy harvesting device.

This thesis work aims to design and fabricate a solid-state plasmonic energy harvesting device using cost-effective techniques. Several sub-objectives guide this endeavour, encompassing the development of numerical models for noble metal plasmonic nanomaterials, the synthesis of semiconductor substrates using a simplified chemical approach, and the design and fabrication of the plasmonic energy harvesting device with nanomaterials synthesized via physical methods. Initially, a finite element method (FEM) based numerical model was developed to analyse plasmonic modes and properties of noble metal nanoparticles. The critical parameters in this study include nanoparticle geometry (shape and size), material properties (dielectric functions of silver and gold), excitation wavelength, and the surrounding medium's refractive index. The simulation study liedemonstrated excellent agreement with experimental data with a less than 2% difference in the plasmonic resonance peak wavelength range. The study also reveals that silver nanoparticles exhibited higher sensitivity to size variations than gold, prompting us to select silver to proceed further toward our objective. This is due to their partially filled d-band, leading to more pronounced changes in electronic properties, surface plasmon resonance, and quantum confinement effects, as well as increased susceptibility to surface-related effects like oxidation and ligand binding. In the next step, semiconductor substrates, namely nanocrystalline TiO_2 thin films, were synthesized using a novel, cost-effective Sol-Gel spin coating technique. TiO_2 thin films fabricated through this technique were homogeneous and

uniform nanocrystalline with band gaps reaching up to 3.99 eV (direct) and 2.69 eV (indirect) and of entirely anatase phase. Except for the film annealed at 400°C, all thin films displayed the anatase phase. Elevating the annealing temperature resulted in larger crystallite sizes, which reduced microstrain and dislocation density. Optical analysis revealed that films annealed at 450°C and 550°C achieved a transmittance of over 80% in the visible range (450 nm and above). These films have band gaps suitable for solar energy applications. After synthesizing the semiconductor substrate and concluding our previous research, we advanced to the next stage, which involved the production of our Plasmonic Energy Harvesting Device. This endeavour successfully developed a solid-state energy harvesting device that incorporates a thin, adjustable Ag layer as the light-absorbing component positioned on top of the layer of TiO_2. Although depositing Ag nanoparticles into semiconductor layers can be complex and time-consuming due to intricate techniques, our study has explored a simplified approach known as Thermal Vapor Deposition (TVD). These devices exploited metal/semiconductor heterojunctions to enhance photovoltaic activity. Our J-V measurements reveal promising cell performances, with a short-circuit current of 1.6 mA cm^{-2} , open-circuit voltage of 440 mV, and fill factor of 0.3, resulting in an efficiency of 0.2%. In the concluding phases of our study, we developed an environmentally friendly method for synthesizing silver-graphene nanocomposites, offering potential applications in various fields. Silver-graphene nanocomposites were synthesized efficiently using a green and cost-effective method with sodium citrate as the reducing agent, known for its mild and non-toxic properties, making the process environment-friendly.

The findings of this research provide insights into the design and fabrication of efficient plasmonic energy harvesting devices, promising advancements in sustainable solar power generation. This work bridges the gap in computational studies of plasmonic materials, particularly in the context of solid-state energy harvesting. Moreover, exploring silver-graphene nanocomposites opens new horizons for enhancing plasmonic device performance. In conclusion, this research contributes significantly to pursuing clean and sustainable energy solutions. The thorough investigation of plasmonic materials, semiconductor substrates, and device fabrication techniques lays a strong foundation for further innovations in renewable energy.

LIST OF ABBREVIATIONS

NPs	Nanoparticles
SPPs	Surface Plasmon Polaritons
LSP	Localized Surface Plasmon
LSPR	Localized Surface Plasmon Resonance
AFM	Atomic Force Microscopy
STM	Scanning Tunnelling Microscopy
TEM	Transmission Electron Microscopy
DDA	Discrete Dipole Approximation
BEM	Boundary Element Method
SERS	Surface-Enhanced Raman Spectroscopy
FDTD	finite-difference time-domain
FEM	finite element method
CPUs	Central Processing Units
SPR	Surface Plasmon Resonance
EBE	electron-beam evaporation
SGD	sol-gel dip-coating
XRD	X-ray diffraction
HRTEM	High-resolution transmission electron microscopy

EDX	Energy-dispersive X-ray analysis
CBD	Chemical Bath Deposition
SEM	Scanning Electron Microscopy
PL	Photoluminescence
FT-IR	Fourier Transform - Infra – red
XPS	X-ray photoelectron spectroscopy
NBE	Near-band-edge emission
DLE	Deep-level emission
PEC	Photo-electrochemical cell
ALD	Atomic Layer Deposition
PEG	Polyethylene Glycol
HF	Hydrofluoric acid
FTO	Fluorinated tin oxide
DSSC	Dye-Sensitized Solar Cells
RPD	Radiation protection
IPCE	Incident Photon to Current Conversion Efficiency
NSs	Nanostars
NIR	Near-infrared
HTMs	Hole-Transport Materials

ITO	Indium Tin Oxide
MNP	Metal Nanoparticle
SIS	Semiconductor-Insulator-Semiconductor
RET	Resonant Energy Transfer
EQE	External Quantum Efficiencies
PML	Perfectly Matched Layer
UV	Ultraviolet
CVD	Chemical Vapour Deposition
ICDD	International Centre for Diffraction Data
FWHM	Full Width Half Maximum
VBM	Valence band maximum
CBM	Conduction band minimum
CCG	Chemically converted graphene
GO	Graphene Oxide
FETEM	Field Emission Transmission Electron Microscope

NOMENCLATURE

Nm	Nanometre
E_p	Plasmon Energy
N	Conduction Electron Density
E	Elementary Charge
m^*	Effective Mass
$\mathscr{E}_0$	Permittivity Of Free Space
Ħ	Reduced Planck's Constant
ω_p	Plasmon Frequency
$\mathscr{E}_b$	Background Permittivity
Ɣ	Drude Relaxation Rate
$\mathscr{E}'$	Real Part Of Dielectric Function
$\mathscr{E}''$	Imaginary Part Of Dielectric Function
Au	Gold
Ag	Silver
kJ/mol	Kilo joules per mole
TiO_2	Titanium dioxide
Ti	Titanium
O	Oxygen
eV	Electron – volt
Eg	Band gap energy

K	Kelvin
^{o}C	Degree Celcius
J_{sc}	Short-Circuit Current Density
V_{OC}	Open Circuit Voltage
FF	Fill factor
mA cm^{-2}	Milli ampere per centimetre square
mV	Milli volt
NiO	Nickel oxide
Λ	Wavelength
E_{inc}	Incident field
S_{sca}	Poynting vector of the scattered field
S_0	Power density of the incident field
Z_0	Characteristic impedance of vacuum
σ_{ext}	Extinction cross-section
σ_{abs}	Absorption cross-section
σ_{sca}	Scattering cross-section
Q_h	Total power dissipation density
Ml	Milli litre
µL	Micro litre
µm	Micro metre
kV	Kilo volt

Å	Angstrom
kHz	Kilo Hertz
N/m	Newton per metre
FWHM	Full Width Half Maximum
Θ	Diffracting angle
μ	Microstrain
D	Crystallite size
Δ	Dislocation density
R_{mean}	Mean roughness
R_{rms}	Root Mean Square Roughness
D_f	Fractal dimensions
Å/s	Angstrom per second
mB	Milli bar
A	Stacking fault
E_f	Energy of the Fermi level
E_{VBM}	Energy of the valence band maximum
Fs	Femtoseconds

LIST OF FIGURES

LIST OF TABLES

CHAPTER 1

INTRODUCTION

CHAPTER 1

INTRODUCTION

1.1 Background

In a world increasingly reliant on energy, the relentless depletion of fossil fuel reserves and the escalating levels of greenhouse gas emissions have thrust the world into an era of unprecedented environmental challenges, and the quest for sustainable and efficient energy sources has become paramount. The formidable challenges of climate change, dwindling fossil fuel reserves, and environmental degradation have spurred a global endeavour to discover innovative and eco-friendly energy conversion technologies. Among these, photovoltaics (PV) stands as a beacon of hope, offering a promising solution to meet our energy demands while mitigating the adverse impacts of traditional energy sources. By converting sunlight into electricity, these devices offer the potential to harness a virtually limitless and clean energy source. Over the years, a multitude of PV technologies have been developed, each with its unique set of advantages and limitations. One technology that has captured the imagination of researchers and engineers alike is the plasmonic photoelectric conversion device.

1.2 Plasmonic Photo-Electric Conversion Devices

Plasmonic photoelectric conversion devices have emerged as a captivating niche within the broader photovoltaic landscape in recent years (Liu et al., 2023). These devices leverage the fascinating properties of plasmons, which are collective oscillations of electrons in conductive materials, to enhance light-matter interactions and boost the efficiency of solar energy conversion. These devices promise enhanced light absorption, as they can absorb light from visible to near-infrared wavelengths without deteriorating photoelectric conversion and adaptability to various wavelengths. Also, plasmonic materials can be incorporated into existing solar cell technologies, reducing the need for expensive material replacements. This cost-effective integration makes them an attractive option for scaling up renewable energy production. Moreover, plasmonic materials often consist of noble metals like gold and silver, which are non-toxic and environmentally caring. These attributes make plasmonic a rapidly evolving field with ongoing research and innovation, compelling avenues for advancing

green energy generation, and addressing the global need for sustainable and renewable energy sources.

Among the various plasmonic systems, solid-state plasmonic photoelectric conversion devices have garnered significant attention for their potential to revolutionize the energy landscape. These devices employ a solid-state structure, often combining semiconductors with plasmonic nanoparticles, to harness the benefits of both materials. In particular, integrating plasmonic elements into solid-state photoelectric devices offers unique advantages, including enhanced light absorption, improved charge separation, and the potential for efficient, low-cost energy conversion.

1.3 Working Principle of Solid State Plasmonic Photo-Electric Conversion Device: Metal-Semiconductor Structure

Following steps collectively describe the process of hot carrier transport in a plasmonic device, which involves the absorption of light, generation of hot carriers, their subsequent transport, and their eventual injection into thin semi-conductor layer to harness their energy for specific applications.

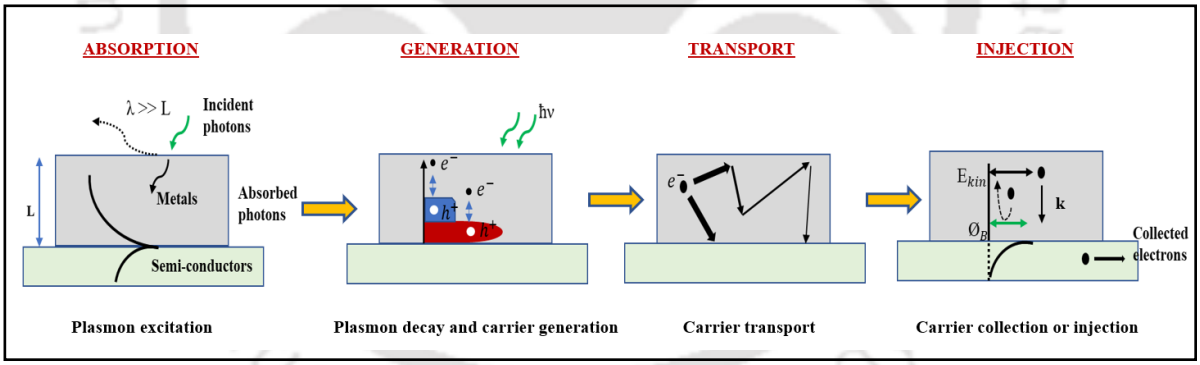

Figure 1.1: Schematic representation of the electronic processes in photoexcited metal nanostructures.

Absorption: Incident photons interact with the plasmonic nanostructure, leading to the generation of surface plasmon resonances. These surface plasmon resonances cause the rapid and efficient absorption of photon energy within the plasmonic nanostructure.

Generation of hot carriers: The absorbed photon energy elevates the energy levels of electrons in the metal nanostructure, creating highly energetic or "hot" carriers. These hot

carriers are typically in the form of electron-hole pairs with significantly higher energy than the electrons in their equilibrium state.

Transport: The hot carriers are rapidly transported within the metal nanostructure due to their elevated energy levels. This transport is driven by the energy gradient, with carriers moving from regions of higher energy to lower energy. During this process, the hot carriers can lose some of their energy through scattering events, collisions, and interactions with lattice vibrations.

Injection: Once the hot carriers reach the interface or junction with another material (e.g., a semiconductor or another metal), they can be injected into the adjacent material. This injection can lead to various effects, such as the generation of charge carriers (hot electrons or hot holes) in a semiconductor or the initiation of chemical reactions at the interface. The injection of hot carriers is a crucial step in utilizing their energy for various applications, such as photodetectors, photocatalysis or photovoltaics.

1.4 Challenges and Strategies to Meet through this Thesis Work

In addition to aforementioned several attributes of plasmonic materials, it also possess the intriguing capability of customization, allowing adjustments in parameters like size, shape, and composition to fine-tune their performance for specific applications. This flexibility allows for customization to suit various environmental and energy generation requirements. However, there are some challenges, as described below, towards the successful development of solid-state plasmonic photo-electric conversion devices.

Fabrication of quality semiconductor substrate: While TiO_2 holds promise for solar energy harvesting due to its wide band gap, it has been observed that structural flaws and defects in TiO_2 hinder the exciton-related recombination process. Hence, there is a need to create higher-quality films for constructing more efficient photovoltaic devices. A suitable method for depositing the film needs to be explored to achieve superior optical and electrical properties in TiO_2 thin films.

Integration: Manufacturing plasmonic noble metal nanoparticles poses difficulties, demanding meticulous control over environmental factors and the use of stabilizing agents

to ensure their stability. Integrating the plasmonic nanoparticles into the active layers is complex and time-consuming, necessitating intricate synthesizing/deposition methods.

Quick and reliable approach to optimizing some of the physical properties of nanoparticles: Nanoparticle dimensions and morphology modifications induce variations in absorption, scattering, extinction spectra, and sensitivity toward the surrounding dielectric medium. Experimentally altering these properties can be a challenging task and a time-consuming effort. Therefore, it is crucial to identify a swift and dependable method for fine-tuning certain physical characteristics of nanoparticles by controlling their size and shape during and after manufacturing. A synergistic approach integrating advanced computational methods with empirical observations is essential to bridge the gap between theoretical predictions and experimental validation. This synergy will ultimately drive progress in nanophotonic and its diverse applications.

Hence, our thesis revolves around gaining a more profound insight into plasmonic phenomena, and our work embarks on a comprehensive journey to unravel the intricacies of solid-state plasmonic photoelectric conversion devices. Through systematically exploring their underlying principles, fabrication techniques, performance enhancements, and real-world applications, this work aims to shed light on the immense potential of these devices in the realm of renewable energy. Therefore, our thesis can potentially drive further progress in green energy technology. The subsequent chapters of this thesis will delve deeper into the various facets of solid-state TiO_2|Ag plasmonic photoelectric conversion devices, from their fundamental operating principles to their integration into practical energy systems. We will discuss the latest advancements, challenges, and prospects driving innovation in this exciting field. The solid-state TiO_2|Ag plasmonic photoelectric conversion device may well be a cornerstone in achieving this vision; through a multidisciplinary approach, we shall make an effort to uncover the science, engineering, and innovation driving the development of these ground-breaking technologies.

1.5 Organization of the Thesis

The overall thesis work is organized into seven chapters as discussed below:

Chapter 1 presents a brief introduction to plasmonic solid state photo electric conversion device, its working mechanism and some challenges while fabricating the device.

Chapter 2 present a literature survey of the various computational techniques used for studying the optical properties of plasmonic materials and various methods used in the fabrication of thin wide band gap, TiO_2, semi-conductor layer. A summary of current status and progress in the area of solid state plasmonic photo-electric conversion device/solar cell is also presented.

Chapter 3 describe the development of a finite element method (FEM) based numerical model for the analysis of plasmonic modes and optical properties of noble metals plasmonic nanoparticles– Ag and Au in different dimensions and its experimental validation.

Chapter 4 elucidate the experimental study on fabrication of semi-conductor thin film that is nanocrystalline TiO_2 thin films and its characterization.

Chapter 5 describe the study and analysis of the design and fabrication of the solid state plasmonic energy harvesting device – Metal – Semiconductor structure.

Chapter 6 deals with the experimental study on the synthesis and characterization of silver-graphene hybrid nanocomposites.

Chapter 7 presents overall conclusion of the thesis work. Additionally, the future scope of the work is also included in this chapter.

CHAPTER 2

LITERATURE REVIEW

CHAPTER 2

LITERATURE REVIEW

The utilization of solar energy to generate electricity or heat could serve as the ultimate solution for addressing the energy crisis, particularly in situations where fossil fuels fall short of meeting the energy requirements. Solar energy is available free of cost and is abundant, exceeding our current power consumption by a factor of 5000 (Abbott, 2010). Using solar energy can also reduce the environmental problems caused by the consumption of fossil fuels by reducing dust, greenhouse gases, and linked haze, acid rain, and global warming. The worldwide installed capacity of solar harvesting devices is 60 GW in electric energy and 300 GW in thermal energy (Weiss et al., 2017), with an annual rapid increase. For the existing technology, there is room for further improvement by enhancing the light absorption or avoiding loss of electricity or heat after absorption. The realm of photovoltaics, which involves transforming sunlight into electricity, represents a swiftly advancing technology with the potential to address the continually growing global demand for energy substantially. Recently, new advances in nanotechnology and material fabrication methods have resulted in an emerging field of plasmonics by properly introducing metallic nanostructures to manipulate light, enabling light trapping in active layers and thereby enhancing the performance of energy-harvesting devices (Atwater & Polman, 2010).

The progress on the development of the solid state plasmonic solar energy harvesting device is central to the literature described in this chapter. The initial phase involves the literature concerning plasmonic materials, with a specific emphasis on noble metals such as gold (Au) and silver (Ag). Following this, the research direction turns towards the examination of processes for fabricating thin-film semiconductors. Lastly, the research agenda includes a literature survey aimed at investigating the latest developments in plasmonic photoelectric conversion devices.

2.1 Noble Metal Plasmonic Materials and its Numerical Simulation

In technical applications involving metal nanoparticles, it is typically necessary to integrate an assortment of these nanostructures with varying size distributions. Consequently, it becomes essential to comprehend the optical characteristics of an individual nanoparticle and the impact of the coupling between the Localized Surface Plasmon Resonance (LSPR) of adjacent particles.

Optical spectroscopies can serve as complementary tools to structural characterization techniques such as atomic force microscopy (AFM), scanning tunnelling microscopy (STM), transmission electron microscopy (TEM), and others. These techniques offer insight into small sample segments, providing information on local properties and characterizing a limited number of nanoparticles at a time.

The optical behaviour of a nanoparticle, characterized by its dielectric function (ε), is determined by solving Maxwell's equations within the material. In 1908, Gustav Mie achieved the precise solution to Maxwell's equations for the optical response of a sphere of arbitrary size immersed in a uniform medium and exposed to a plane monochromatic wave (Mie, 1908) (Kreibig & Vollmer, 1995). On the other hand, rigorous solutions of the Maxwell equations for non-spherical particles are not straight forward. Only few exact solutions are known: the case of spheroids by Asano and Yamamoto (Asano & Yamamoto, 1975) and for infinite cylinders by Lind and Greenberg (Lind & Greenberg, 1966). Hence, obtaining the optical characteristics of nanoparticles with arbitrary shapes often involves approximations. For instance, the Gans approximation can be employed for ellipsoids composed of highly transparent materials, where the refractive index is significantly low, and the size is much smaller than the wavelength (Van de Hulst, 1958). Due to the intricate nature of the systems under examination, efficient computational techniques capable of handling large-sized materials become indispensable. Over recent years, various numerical methods have been developed to ascertain the optical properties of non-spherical particles, including but not limited to the discrete dipole approximation (DDA), the T-matrix method, spectral representation, finite differences methods, among others. (Mishchenko et al., 2000).

Due to their distinct optical characteristics, the primary materials commonly employed in plasmonics are gold and silver, with aluminium being used to a lesser extent. These materials exhibit plasma frequencies within the visible or ultraviolet spectral ranges, making them highly influential in the realm of optics and photonics applications.

Kelly et al., (2003) studied the optical properties mainly extinction spectra of metal nanoparticles, primarily focusing on silver nanoparticles, in complex environments. Extinction spectra describe how much light is absorbed and scattered by nanoparticles. Simple analytical theories, like the Mie-Lorentz-Wisconsin Approximation (MLWA), are emphasized for providing qualitative insights into how plasmon resonance properties vary with particle size, shape, and environment. These theories have traditionally focused on dipole plasmon resonances but can be extended to quadrupole resonances, which are shown to be important for certain non-spherical particles. The Discrete Dipole Approximation (DDA) method is described as a workhorse for studying non-spherical/non spheroidal particles. It is particularly suited for complex particles in heterogeneous environments and for calculating far-field properties like extinction and scattering spectra. The method relies on defining grids to represent the environment and ensuring fine grid resolution for accurate results. He also mentions two weaknesses of the DDA approach. First, it has limitations in terms of the total volume of material it can describe, constrained by available computational resources. Second, it may produce inaccurate electric field calculations close to particle surfaces. On a similar front, Sosa et al., 2003 also studied the optical properties of metallic nanoparticles of varying sizes and shapes, primarily composed of silver and gold, were comprehensively explored using the DDA. The research uncovered distinct optical signatures associated with each nanoparticle's geometry, size, and material composition, highlighting their potential for unique characterization. As nanoparticles exhibited less symmetry or increased vertices, their optical spectra became more intricate. Surface plasmon resonances, including dipolar and high-multipolar excitations, were identified and attributed to both shape and size variations. Optical spectroscopy emerged as a valuable tool for nanoparticle characterization, emphasizing the importance of studying absorption and scattering efficiencies in addition to extinction efficiency. While a challenge remains in comparing theoretical results to experimental measurements with broader size and shape distributions, the study underscores the desirability of controlled samples for precise correlations between

optical properties and nanoparticle characteristics, with implications for nanotechnology and materials science.

Khlebtsov et al., (2005) investigated how the size, shape, and structure of gold and silver nanoparticles affect their dependence on the dielectric environment in terms of extinction and integral scattering spectra. The study employed different theoretical methods for various nanoparticle shapes, including Mie theory for spheres and nano shells, and the T-matrix method for bispheres, spheroids, and s cylinders with hemispherical ends. For nanoparticles with an equivolume diameter of 15 nm, the study observed that the maximal shifts in plasmon resonances due to changes in the refractive index of the environment were most pronounced for bispheres. The shifts in plasmon resonances decreased in the order of nano shells, cylinders, spheroids, and spheres. The study also explored how variations in the thickness of the metal layer in nano shells affected plasmon resonances. Notably, the study found that, under similar conditions, silver nanoparticles exhibited greater sensitivity to changes in the dielectric environment compared to gold nanoparticles.

Liaw, (2006) mentions the development of surface integral equations, specifically Fredholm equations of the second kind, derived from the Stratton–Chu formulation of Maxwell's equations. These equations are designed to analyze the behavior of electromagnetic waves when interacting with nanostructures. The equations are employed to simultaneously solve for the surface components on the boundary, including the tangential magnetic field, the normal displacement, and the tangential electric field. This is done numerically using the Boundary Element Method (BEM).

Zhao et al., (2008) provides a comprehensive examination of the techniques currently utilized to investigate the electromagnetic characteristics of silver and gold nanoparticles, with particular emphasis on the assessment of extinction and the acquisition of Surface-Enhanced Raman Scattering (SERS) spectra. Analytical methods discussed in the account either stem from Mie theory, which was originally developed for spheres, or from the quasistatic (Gans) model as applied to spheres and spheroids. Mie theory, for instance, is employed to ascertain electromagnetic contributions to SERS enhancements, including effects related to retarded dipole emission. Meanwhile, the quasistatic approximation finds application when dealing with spheroidal particles that interact with adsorbate layers of dyes.

This account also discusses numerical techniques, including the DDA, the finite-difference time-domain (FDTD) method, and the finite element method (FEM) based on Whitney forms. The discussion covers various applications, such as using DDA to characterize the interaction between two gold disks to define electromagnetic hot spots, employing FDTD for investigating light interaction with metal wires that transition from particle-like plasmonic responses to film-like transmission as wire dimensions change, and utilizing FEM to study electromagnetic fields in proximity to cubic particles. FEM is well-suited for modelling irregular geometries, efficiently simulating large domains with fine details, and can often handle problems that would typically require multiple CPUs on a single machine.

McMahon et al., (2009) discusses FEM calculations conducted on 90-nanometer (nm) gold (Au) nanoparticle dimers, designed to resemble experimental nanotags. The findings from this study on 90-nanometer gold nanoparticle dimers reveal crucial insights into their electromagnetic properties and their impact on SERS. Notably, the distance between these nanoparticle dimers, particularly when it falls below 1 nanometre, significantly influences their electromagnetic behaviour, leading to substantial red-shifting of extinction spectra. Remarkable electromagnetic field enhancement, exceeding 10^{10} fold is produced by extremely small spacings, even down to 0.5 nanometres, and minor fusing causing microscopic fissures. These calculations underscore the dominant role of electromagnetic fields in enhancing SERS signals. Furthermore, the research highlights that only a small fraction of molecules, often less than 3%, substantially contribute to over 90% of the observed SERS signal, indicating a spatial selectivity in SERS enhancement. The findings are in good agreement with experimental observations obtained from transmission electron microscopy and localized surface plasmon resonance spectra.

Amendola et al., (2010) delved into the examination of the Surface Plasmon Resonance (SPR) of silver nanoparticles (AgNPs) through the discrete dipole approximation method. The research considered various factors, including nanoparticle shapes, sizes, dielectric surroundings, and supra-particle assemblies. Of particular interest were AgNPs with sizes less than 10 nm, where accounting for the correction of the silver dielectric constant due to intrinsic size effects becomes crucial. The study revealed that the shape and assembly of AgNPs can introduce distinct features in the extinction spectra, with SPR being more intense when AgNPs have discoid or flat shapes and are enveloped in a dielectric shell with

a high refractive index. However, these distinctive features diminish when size effects and stabilizing molecules cause significant broadening of the extinction bands, a phenomenon often observed in thiolated AgNPs smaller than about 5 nm. These findings offer valuable insights for characterizing and monitoring AgNPs synthesis in real-time and for tailoring AgNPs with specific plasmonic properties through engineering.

Alsawafta et al., (2012) discusses the use of the DDA for modelling the plasmonic behaviour of Au and Ag ellipsoidal nanoparticles. These nanoparticles exhibit various plasmonic modes, including longitudinal and transverse modes, influenced by their size and orientation. Notably, AgNPs have higher-energy and well-separated plasmonic modes compared to AuNPs. The text also mentions the effect of length distribution on plasmonic properties, emphasizing a linear relationship between axis length and band position. Experimental data on single AuNPs supports the simulation results, and the study suggests conducting similar experiments with AgNPs, particularly to explore their interactions with nearby molecules.

Kluczyk & Jacak, (2016) also investigate how the size of metal nanoparticles influences plasmon resonance using both theoretical and numerical approaches. They aim to enhance the precision of optical methods for identifying the size and shape of metallic nanoparticles. Their theoretical approach involves using the quantum random phase approximation model to describe plasmons in metallic nanoparticles. This model accounts for plasmon damping caused by electron scattering and radiative losses (Lorentz friction). The numerical aspect of the study employs the finite element method to solve Maxwell's equations, considering incident planar waves interacting with nanoparticles of various shapes (spherical, nano-rod, spheroid). The researchers use software like COMSOL and apply the Mie treatment, complemented by a phenomenologically modelled dielectric function for the metallic nanoparticles. The study includes a comparison of their theoretical and numerical results with experimental data, focusing on light extinction in colloidal solutions containing Au and Ag nanoparticles of different sizes. A significant finding of the research is the critical role played by Lorentz friction in the size-dependent behavior of plasmon resonance, particularly in larger metallic nanoparticles, such as those ranging from 20 to 60 nm in diameter for AuNPs in a vacuum environment. This observation highlights the importance of

accurately considering Lorentz friction in understanding plasmon resonance in metallic nanoparticles.

Pathak, (2020) focuses on investigating the optical properties of metal nanostructures and their potential applications in the field of energy. Metal nanostructures have the unique property of supporting plasmonic resonances, and these resonances can be controlled or "tuned" within specific regions of the solar spectrum by altering factors such as the nanostructure's size, shape, and surrounding environment. The study examines two different systems: isolated gold metal nanospheres and coupled gold metal nanospheres. The primary objective is to analyze the optical properties of these nanostructures in terms of their surface plasmon resonances, which play a crucial role in their interaction with light. The research employs the Boundary Element Method (BEM) to study these optical properties and how they can be adjusted within various parameter domains. The main focus of this work is on tuning surface plasmon resonances and exploring their potential applications in the field of energy. One of the key outcomes of the study is the simulation of the extinction spectrum, which provides insights into how these metallic nano geometries interact with and absorb light. The corresponding spectral width is also examined. The findings from this research have the potential to be applied in various energy-related applications, including solar stills, solar collectors, and solar cells. Essentially, the work contributes to our understanding of how metal nanostructures can be optimized for harnessing solar energy efficiently.

Kavita & Verma, (2021) employs theoretical simulations conducted using MATLAB. The primary focus is on determining the variation of the extinction cross-section, which provides information about the absorption coefficient, with respect to the wavelength of incident light. The study specifically investigates graphene-coated silver nanoparticles. Graphene is a two-dimensional material with unique properties, and it is employed alongside silver nanoparticles to manipulate their optical properties. To gain insights into the optical response of this arrangement, the Maxwell-Garnett (MG) theory is analytically applied. This theory helps calculate the effective dielectric constant of the composite material, taking into account the presence of both graphene and silver nanoparticles.

Technical applications of metal nanoparticles normally require incorporating an assembly of those nanostructures of different size distributions, and thus understanding the

optical behaviour of an isolated nanoparticle and the effect of the coupling between the LSPR of nearby particles is required.

Table 2.1: Comparative analysis of computational methods used in plasmonics. (Gonçalves, 2014)

Methods	**Method description**	**Advantage**	**Limitations**
Mei based analytical solutions	Analytic solutions for fields and cross sections for sphere and infinite cylinders	Rigorous solution, no approximations; some analytical solutions valid for particles close to a substrate	Only valid for two particle shapes
Discrete Dipole Approximation	Approximate solution based on coupled dipoles	Arbitrary particle; stratified media; periodic scattering targets; far and near field can be calculated	Time consuming; large particles with small details require huge memory space; not supporting particles on infinite substrates
Boundary Element Method	Numeric solution of integral equations with surface discretization	Fast calculation, comparing to volume methods; general application	Complex parametrization; few codes available for electromagnetic
Finite Element Method	Differential equations solved for adaptive space discretization of the computational domain	General application: arbitrary shape and dielectric function; periodic structures; permits coupling between fields and other physical quantities (COMSOL Multiphysics)	Time consuming; large memory space required for complex structures

Finite Difference Time Domain	Numerical solution with cubic discretization (Yee cell)	General application; periodic and non-periodic structures; simple algorithm and many codes available; broadband spectra obtained from the Fourier transform of the system response to a short pulse	Staircase artefacts on non-rectangular geometries of particles; time consuming for spectral calculations

In conclusion, the extensive research on metal nanoparticles' optical properties, as discussed in the provided paragraph, underscores their critical role in various technical applications. Understanding the complex interplay of factors, including nanoparticle size, shape, material composition, and dielectric environment, is essential for optimizing nanoscale devices and materials. Numerical simulation techniques, ranging from the DDA to FEM, have proven indispensable for modelling and predicting nanoparticle optical behaviour. These simulations provide vital insights into phenomena such as LSPR and enable researchers to tailor optical properties for applications like sensors, SERS, and energy-related technologies. Controlled experiments are highlighted as crucial for bridging theory and practice, promising advancements in these fields and furthering our understanding of nanoscale phenomena. Overall, this body of research emphasizes the pivotal role of numerical simulations in advancing the study of metal nanoparticles' optical characteristics.

2.2 Fabrication of TiO_2 Thin Films

Kumar et al., (1999) synthesized nanophase TiO_2 through two distinct routes using different organic solvents (propanol or ethanol) along with acetonitrile, resulting in rutile and anatase phases with complex structural compositions, including Ti_2O_3 overlays. Characterization techniques such as UV-vis spectroscopy, transmission electron microscopy, and X-ray diffraction confirmed nanoscale particle sizes and structural diversity. Unique optical properties, including red-shifted peaks and vibrational features in the photo-luminescence spectra, were observed. Fourier transform infrared analysis unveiled surface

complexities with Ti^{3+}-OH and Ti^{4+} -O sites, while X-ray photoemission spectra highlighted sub-valence states and adsorbed sites. These findings not only enhance our understanding of nanoscale TiO_2 materials but also reveal opportunities for diverse applications, particularly in catalysis and nanotechnology, while noting nuanced differences from existing literature reports.

Oh et al., (2003) discusses a study comparing transparent TiO_2 thin films deposited on soda lime glass using two methods: electron-beam evaporation (EBE) and sol-gel dip-coating (SGD). The films underwent structural changes from amorphous to nanocrystalline anatase as the calcination temperature increased. Both film types exhibited reduced transmittance at higher temperatures due to particle growth, with SGD films showing a more significant increase in refractive index than EBE films. While EBE films had better optical properties, SGD films displayed superior photocatalytic activity attributed to their higher porosity and the formation of Ti^{3+} ions during calcination, highlighting the importance of film preparation methods in tailoring the properties of TiO_2 thin films for specific applications.

Tian et al., (2006) discusses the preparation and characterization of TiO_2 coatings on fused silica using electron beam evaporation deposition, followed by annealing at different temperatures. Various properties of these coatings were investigated using techniques such as X-ray diffraction (XRD), spectrometer, photoelectron spectroscopy (XPS), and atomic force microscopy (AFM). With increasing annealing temperature, transmittance decreased, accompanied by a shift in the cut off wavelength towards longer values in the near-ultraviolet range, indicating reduced transparency and increased optical loss at higher temperatures. The crystalline phase transformed from amorphous to polycrystalline anatase after annealing, and XPS analysis identified slight chemical shifts attributed to oxygen vacancies around Ti^{+4} ions. AFM revealed that higher annealing temperatures led to increased surface roughness, suggesting the granulation of the coating surface. These findings enhance our understanding of the annealing's impact on TiO_2 coatings and their potential applications in optical devices and materials.

Senthil et al., (2010) TiO_2 films were prepared through a sol-gel spin coating process using Titanium isopropoxide, ethanol, and acetic acid at room temperature. Initially, the

pristine films were amorphous, but after annealing, they transitioned into nanocrystalline structures with improved crystallinity. Multiple techniques, including XRD, high-resolution transmission electron microscopy (HRTEM), and Raman spectroscopy, confirmed the presence of the anatase phase in the films. The films exhibited nanocrystalline domains with grain sizes of 19 nm and 22 nm for annealing temperatures of 450°C and 550°C, respectively. The Raman spectra of the films were distinct, with no overlapping peaks, indicating a low level of impurity sites. Specific vibration peaks at 145 cm^{-1}, 394 cm^{-1}, 513 cm^{-1}, and 635 cm^{-1} were identified as Raman active modes of the anatase phase of TiO_2. Based on the favourable properties of the anatase TiO_2 films, they are considered highly suitable for the fabrication of quantum dot solar cells.

Study conducted by Arıer & Tepehan, (2011) revolves around the preparation and analysis of pure nanobrookite titania (TiO_2) thin films by dissolving Titanium butoxide (Ti(OC4H9)4) in ethanol, and adding water for hydrolysis reaction, which is followed by drop wise addition of acetic acid (AcAc), which were deposited onto glass substrates via the spin-coating method. The research primarily explores the influence of heat treatment temperatures on the particle size of these TiO_2 films. Notably, higher heat treatment temperatures resulted in larger particle sizes due to increased crystallization, correlating with increased film roughness. Moreover, the thin films exhibited a consistent single-orientation crystal structure, specifically (211) orientation, across various heat treatment temperatures. The optical properties of these nano brookite films varied with particle size; reduced particle size led to higher optical transmittance and lower reflectance values. Importantly, the bandgap of the films increased in the shorter wavelength region, indicating altered electronic properties compared to bulk material. The study also calculated an activation energy of approximately 23.1 kJ/mol for particle growth in nano brookite TiO_2 films, a value not previously reported in the literature. This value reflects the lower energy required for particle growth in the films, possibly attributed to their higher surface area-to-volume ratios in comparison to bulk material.

Sönmezoğlu et al., (2012) describes a research study involving the growth and characterization of nanostructured TiO_2 thin films deposited on glass substrates using the sol-gel dip coating technique at room temperature (ambient conditions). The study focuses on the effects of annealing these thin films at temperatures ranging from 200°C to 700°C and

how it affects the structural, morphological, and optical properties of nanostructured TiO_2 thin films. The films transformed into triangular pyramids with larger grain sizes, exhibited high transmittance, and showed a decrease in the optical band gap with increasing annealing temperature. Additionally, the refractive index of the films increased as a result of the annealing process, making them potentially useful for various optical and optoelectronic applications.

Vishwas et al., (2012) in their work, TiO_2 thin films were meticulously fabricated on fused quartz substrates using the electron beam evaporation method at room temperature. These films were then subjected to a series of annealing processes at different temperatures in ambient air. The investigation primarily focused on assessing how annealing temperature influenced various properties of the TiO_2 films. Notably, the study observed a significant enhancement in the films' crystallinity as the annealing temperature increased, indicating improved crystal quality with higher temperatures. The films' surface morphology and roughness were examined through AFM, revealing likely changes in surface topography resulting from the annealing treatments. Furthermore, by determining the refractive index of the TiO_2 films using the envelope method and reflectance spectra, the study highlighted the films' possession of a high refractive index, which holds relevance for optical applications. Photoluminescence measurements disclosed that the films exhibited heightened photoluminescence intensity in the green emission spectrum with increasing annealing temperatures, indicative of alterations in their optical properties. Moreover, Raman spectra analysis identified the presence of the anatase crystal phase in the TiO_2 films after annealing at temperatures exceeding 300°C. These collective findings suggest that these TiO_2 films, known for their homogeneity, transparency, uniformity, and stability, exhibit promising characteristics for application in opto-electronic and optical coating technologies, where a high refractive index, superior optical quality, and photoluminescence characteristics are highly advantageous.

Ranjitha et al., (2013) Nanocrystalline TiO_2 thin films were fabricated using the sol-gel dip coating technique and subjected to comprehensive characterization to unveil their structural and optical attributes. X-ray diffraction analysis affirmed the existence of the anatase phase of TiO_2 within the films, with nanocrystals displaying grain sizes spanning from 18 to 26 nm. HRTEM further affirmed the presence of TiO_2 nano crystallites, possessing

an average particle dimension of 24 nm. EDX analysis validated the presence of Titanium (Ti) and oxygen (O) elements in the samples, affirming their TiO_2 composition. Notably, optical absorption spectra indicated a redshift in the absorption edge as the annealing temperature increased, resulting in a reduction in the films' band gap. These results emphasize the significant impact of annealing temperature on both the structural and optical characteristics of nanocrystalline TiO_2 thin films, with potential applications spanning photovoltaics, photocatalysis, and sensors, where such films are commonly utilized.

Wang et al., (2015) study addresses a common limitation of anatase TiO_2 as a photocatalyst due to its large bandgap (3.2 eV), which restricts its light absorption primarily to the UV region of the solar spectrum, limiting its industrial applications. The traditional approach to enhance visible light activity through doping can introduce defect states that hinder the efficiency of photogenerated charge carriers. Instead, the study presents a simple soft-chemical method using ethanol as the sole solvent to modify the surface properties of TiO_2 crystals. In this process, individual TiO_2 nanocrystals are synthesized initially, and their affinity with ethanol molecules leads them to assemble through interfacial Ti-Ti bonding during ethanol evaporation-induced self-assembly. This bonding reduces the surface oxygen atoms in TiO_2, altering the electronic structure and extending light absorption to around 550 nm, making it responsive to visible light. Notably, this approach doesn't involve doping or additives. The resulting assembly of TiO_2 exhibits notable photocatalytic activity under visible light, owing to its narrower bandgap compared to individual nanocrystals. The study also confirms the generation of reactive •OH radicals on the surface of assembled TiO_2 under visible-light irradiation, further enhancing its photocatalytic capabilities. In summary, this work presents a dopant-free method for narrowing the bandgap of TiO_2 through surface engineering. It involves the assembly of individual nanocrystals using ethanol as a solvent, which extends its light absorption into the visible spectrum. This approach offers potential applications in harnessing solar energy through visible light-responsive materials.

Govindasamy et al., (2016) focuses on the fabrication and comprehensive characterization of TiO_2 thin films prepared via the Chemical Bath Deposition (CBD) method. Various analytical techniques were employed to assess the structural, morphological, optical, and electrical properties of these films. XRD analysis provided insights into the film's crystal structure and crystallite size, shedding light on its overall quality. Scanning Electron

Microscopy (SEM) was used to examine the surface morphology and identify any surface features or defects. Optical properties were studied through UV-Visible and photoluminescence (PL) spectra, offering valuable data on absorption, emission, bandgap, and luminescence characteristics. Furthermore, optical constants such as refractive index, extinction coefficient, and electric susceptibility were determined to provide a comprehensive view of the film's optical behaviour. FT-IR spectroscopy confirmed the presence of TiO_2 in the films, elucidating chemical composition and bonding. Dielectric properties were assessed across different frequencies and temperatures, revealing how the material responds to electric fields under varying conditions. The AC electrical conductivity analysis highlighted that conduction depended on both frequency and temperature. Additionally, the study confirmed the positive photoconductivity of the TiO_2 thin films, indicating their potential utility in photodetectors and sensors. In summary, this research presents a thorough exploration of TiO_2 thin films, encompassing their structural, optical, electrical, and photoconductivity characteristics, essential for evaluating their suitability for diverse technological applications.

Quiroz & Dussan, (2016) In their work, TiO_2 nanotubes were fabricated using an electrochemical anodization method on Titanium foils. The research explored the impact of different parameters, including water and fluoride concentrations in ethylene glycol solutions (ranging from 1% to 3% and 0.15% to 0.5%, respectively), on the morphological, optical, and crystalline attributes of TiO_2 nanotubes. Subsequently, annealing procedures were applied to all samples within a temperature range spanning from 273 K to 723 K. Various characterization methods, including scanning electron microscopy, XRD, and transmission electron microscopy, were utilized to assess both the morphology and structural properties of the nanotubes. XRD patterns showed reflection peaks corresponding to various phases of TiO_2, including Brookite, Anatase, and Rutile, with the presence of Ti_3O_5 also observed in detail via XRD measurements. The optical properties of the TiO_2 nanotubes were analysed through transmittance spectra in the UV-Vis range, revealing strong absorption in the UV region. The optical band gap values (Eg) for the Anatase and Rutile phases were determined to be 3.7 eV and 3.4 eV, respectively, based on absorption coefficient spectra. Overall, this study demonstrates the controllable synthesis of TiO_2 nanotubes with varying morphologies and optical properties by adjusting synthesis conditions, offering valuable insights into the relationship between synthesis parameters and physical characteristics of these nanotube

arrays. The nanotubes remained stable even after annealing, making them promising for various applications.

Dussan et al., (2017) investigates the characteristics of TiO_2 thin films fabricated using the chemical bath deposition technique, placing specific emphasis on the changes in their structural, morphological, and optical attributes after undergoing annealing processes at varying temperatures spanning from 373K to 723K. The XRD analysis consistently identified the presence of the Rutile phase in all tested samples. However, as the annealing temperature was increased to 723K, the Anatase phase became evident. Scanning electron microscopy (SEM) observations unveiled the formation of intriguing nanoflower structures. These flower-like formations were composed of nanorods approximately 10 nm in length. As the annealing temperature was raised, these nanoflowers transformed into platelets that covered the entire surface. The optical properties of the TiO_2 thin films were explored, and an optical band gap energy (Eg) of 3.0 eV was determined initially. However, this band gap value decreased slightly to 2.98 eV after annealing at 723K, coinciding with the emergence of the Anatase phase. In summary, this investigation provides insights into how annealing at various temperatures induces changes in the structure, morphology, and optical properties of TiO_2 thin films. The identification of Rutile and Anatase phases, the evolution of nanoflower structures into platelets, and the subtle change in the optical band gap provide valuable insights into the properties of these thin films under varying thermal conditions.

Şilik et al., (2017) worked on the production of Titanium dioxide (TiO_2) thin films on substrates composed of fluorine tin oxide/glass and indium tin oxide/glass using the thermionic vacuum arc deposition technique. Examination of the deposited films using XRD unveiled the existence of two distinct phases, namely anatase and rutile. Additionally, the bandgap of these thin films was determined to be approximately 3.0 eV. The research delved into the electrochromic properties of these TiO_2 thin films, employing various electrochemical techniques such as cyclic voltammograms, chronoamperometry, and chronocoulometric studies. Notably, one of our key findings was the favourable electrochromic performance of the TiO_2 thin film on fluorine tin oxide/glass (TiO_2/FTO). This particular sample exhibited a noteworthy coloration efficiency of 18.68 cm^2/C and an 8% optical modulation.

Kite et al., (2018) work involved the deposition of TiO_2 thin films through a CBT method on both conducting and non-conducting glass substrates, followed by annealing at temperatures of 300°C, 400°C, and 500°C. Key findings and observations include the characterization of the films using XRD, which provided insights into their structural properties, including crystallite size and microstrain. Optical absorption spectra indicated a decrease in the bandgap energy as the annealing temperature increased. Photoluminescence (PL) analysis revealed the presence of two luminescence centers, one associated with near-band-edge emission (NBE) and another with deep-level emission (DLE). FT-IR spectroscopy confirmed the presence of anatase TiO_2 in the films annealed at 400°C. Morphological and compositional analysis using FESEM and energy dispersive X-ray (EDS) analysis focused on the film annealed at 400°C. The study also explored the performance of these TiO_2 thin films in a photoelectrochemical cell (PEC). Notably, the films annealed at 400°C demonstrated exceptional PEC performance, achieving a high photoconversion efficiency of 1.94%. This research provides valuable insights into the structural, optical, and photoelectrochemical properties of TiO_2 thin films, highlighting their potential for photovoltaic applications, particularly when annealed at specific temperatures.

Khan et al., (2020) investigates the optimization of TiO_2 thin films for photocatalytic and photovoltaic applications, where the longevity of charge carriers is crucial for device efficiency. Traditionally, high-temperature treatments have been used to ensure long carrier lifetimes, but this limits TiO_2's compatibility with organic or polymer components. To address this challenge, the researchers employed low-temperature atomic layer deposition (ALD) to fabricate 30 nm TiO_2 thin films from tetrakis(dimethyl amido)Titanium, followed by heat treatment in air to determine the minimum temperature requirements for maintaining carrier lifetime. Femto-to-nanosecond transient absorption spectroscopy and grazing incidence X-ray diffraction were employed for carrier lifetime and structural analysis. The most favourable outcome was achieved with TiO_2 thin films grown at 150°C and heat-treated at just 300°C. Initially amorphous, these films crystallized into the anatase phase at 300-500°C. Carrier lifetimes increased significantly, exceeding 400 picoseconds upon crystallization at 500°C. In contrast, films deposited at 100°C and subsequently crystallized as anatase had shorter carrier lifetimes, less than 100 picoseconds. For efficient photoelectrodes, longer carrier lifetimes are essential, and the most favourable results at the

lowest possible temperature were achieved with samples deposited at 150°C and heat-treated at 300°C. Further increases in heat treatment temperature provided only marginal improvements in carrier lifetime, making this approach particularly beneficial when the system incorporates organic or polymer components.

In this study, thin films of TiO_2 were deposited onto optical glass substrates using a coating process involving metal alkoxide precursors, chelating agents, and solvents. To control the porosity and achieve specific optical properties of the TiO_2 films, polyethylene glycol (PEG) and europium nitrate were introduced into the coating solution. The deposition was carried out using a dip-coating method, followed by annealing at 550ºC. Characterization of the precursor powders involved thermal analysis, FT-IR spectroscopy, and surface area measurements. The optical properties of the TiO_2 films were assessed through UV-Vis absorption/reflection spectroscopy and photoluminescence measurements. Additionally, the morphology of the films was examined using SEM. The study found that the composition of the coating solution, including the presence of modifiers like PEG and dopants like $Eu(NO_3)_3$, had a significant impact on the optical properties of the films, affecting transmittance and diffuse reflectance in the UV-Vis region. Specifically, the optical quality of the TiO_2 films deteriorated as the molecular weight of PEG increased. Furthermore, the introduction of PEG with varying molar weights allowed for the adjustment of film porosity, as confirmed by surface area measurements. Under ultraviolet excitation, the TiO_2:Eu thin films exhibited red luminescence attributed to the presence of Eu3+ ions. This suggests the potential utility of these films in optoelectronic applications that require luminescent properties. In summary, the study demonstrates the influence of precursor composition on the optical characteristics and porosity of TiO_2 films, with a particular focus on the role of PEG and europium nitrate as modifiers and dopants, respectively.

Sivaprakash & Narayanan, (2021) synthesized TiO_2 nanotubes through electrochemical methods with varying levels of water content and hydrofluoric acid (HF) in the electrolyte. The results revealed that the addition of HF in the electrolyte, particularly at 40 V, significantly increased the length of the nanotubes. Additionally, annealing the nanotubes at 550°C transformed their structure from amorphous to a mixed phase of anatase and rutile, leading to improved mechanical and chemical properties. High-resolution SEM analysis confirmed that nanotube dimensions increased with higher acidic electrolyte levels,

with the longest nanotubes achieved at 10 wt% water content and 0.25 wt% HF. Nanoindentation analysis indicated that longer nanotubes exhibited superior mechanical performance, while corrosion resistance analysis revealed that longer nanotubes were more resistant to corrosion. These findings underscore the importance of electrolyte composition, annealing, and nanotube length in tailoring TiO_2 nanotubes for various applications, including the promising potential for biomedical materials.

Manisha et al., (2021) used the hydrothermal method to fabricate hydrophilic Titanium dioxide (TiO_2) nanostructured surfaces. These surfaces were grown on fluorinated tin oxide coated (FTO) glass substrates, which share a crystal structure with TiO_2, promoting epitaxial nucleation and rutile evolution. Characterization was conducted using FESEM and XRD, revealing star-like TiO_2 nanorod morphology and a tetragonal rutile structure with an average crystallite size of 18.3 nm. After UV-light irradiation, the hydrophilic TiO_2 surfaces exhibited contact angles of 41 ± 5° and 48 ± 5°, confirming their hydrophilic nature. These surfaces have potential applications in self-cleaning, anti-fouling, and antifungal processes, as well as in fields like dye-sensitized solar cells (DSSC), functionalized biosensors, microfluidics, drug delivery, and biomedical technology due to their stability, durability, and non-toxicity. Additionally, they show promise for radiation protection (RPD) items and dental applications. Overall, the study highlights the versatility and utility of hydrophilic TiO_2 nanostructures across a range of fields.

In conclusion, the collection of research studies presented here offers a comprehensive exploration of TiO_2 materials in various forms, including nanophase TiO_2, thin films, nanotubes, and nanostructured surfaces. These investigations delve into the synthesis, characterization, and properties of TiO_2 materials, shedding light on their structural, morphological, optical, and electrochemical attributes. Throughout these studies, annealing temperature, precursor composition, doping, and synthesis methods emerge as critical factors influencing the properties of TiO_2 materials. Notably, the control of TiO_2 properties through these parameters opens up exciting prospects for a wide array of applications, including catalysis, nanotechnology, photovoltaics, sensors, and optoelectronic devices. The findings emphasize the importance of understanding the nuanced effects of annealing temperature on TiO_2 materials, which can lead to alterations in crystalline phases, optical band gaps, and morphological features. These research studies collectively contribute

to our understanding of TiO_2 materials and their versatility, offering valuable insights into tailoring their properties for a wide range of technological and scientific endeavours. Moreover, they underscore the significance of precise control over synthesis parameters and post-processing treatments in harnessing the full potential of TiO_2 materials across diverse applications.

2.3 Solid State Photo-Electric Conversion Device

Plasmonic solar cells, which utilize plasmonic metal nanoparticles (NPs) in conjunction with electron-accepting semiconductors, were first introduced in the pioneering work conducted by the Tatsuma group in 2004 and 2005. This research represented a significant advancement in the field of solar cell technology by harnessing the unique properties of plasmonic materials which can enhance the performance of photovoltaic devices. The integration of plasmonic metal NPs with semiconductors allowed for improved light absorption and electron transfer processes, contributing to the development of more efficient solar cells (Tian & Tatsuma, 2004).

Tian and colleagues demonstrated that AuNPs could serve as photosensitizers in place of traditional dye molecules in dye-sensitized solar cells (DSSCs). DSSCs are a type of solar cell that uses a liquid electrolyte, typically containing the I^-/I^{3-} redox pair, to transport electrons between two electrodes. Their research achieved impressive results, including nearly 100% incident photon to current conversion efficiency (IPCE) and over 10% power conversion efficiency. These metrics are crucial for evaluating the effectiveness of a solar cell in converting incoming photons into electricity. The researchers used a combination of AuNPs and TiO_2, an electron-accepting semiconductor commonly used in DSSCs. They also employed an appropriate electron donor, often in the presence of $Fe^{2+/3+}$ ions. The key to their success was the excitation of the plasmon band in the AuNPs. Plasmon resonance is a phenomenon in which the collective motion of electrons in a metal nanoparticle is excited by incident light, leading to enhanced light absorption. While their work resulted in a maximum IPCE of 26%, this value was lower than that typically achieved in DSSCs using conventional dye molecules. However, this research was still considered ground breaking due to the novel properties of AuNPs. The authors highlighted the fundamental differences in the excitation mechanisms between Au NPs and traditional dyes. AuNPs exhibit collective excitation, while

dyes undergo single-electron excitation. This distinction in excitation mechanisms has implications for charge separation and overall device performance. Another important difference was the lifetime of the LSPR in Au NPs, which was very short (about 10 femtoseconds), compared to the longer lifetime of excited dye molecules (around 1 nanosecond). This short lifetime posed challenges and opportunities for charge separation processes. The researchers provided evidence that charge separation occurred through electron transfer from the excited AuNPs into the TiO_2 semiconductor. This electron transfer process is crucial for converting visible light into electricity (Tian & Tatsuma, 2005).

In summary, Tian and co-workers demonstrated the feasibility of using plasmonic Au NPs as photosensitizers in DSSCs, achieving noteworthy IPCE and power conversion efficiency. Despite the lower IPCE compared to traditional DSSCs, their work had a significant impact on the scientific community due to the unique excitation mechanisms and properties of Au NPs, providing insights into the potential of plasmonic materials for solar energy conversion.

Misawa and colleagues conducted further research in which they used well-controlled gold nano stars (NSs) on a TiO_2 single crystal. These NSs were fabricated using electron-beam lithography. The use of NSs allowed for precise control over the shape and size of the gold nanoparticles. The researchers found that these gold NSs, when placed on the TiO_2 single crystal, could function effectively as photoelectrodes in the presence of an aqueous electrolyte. This suggests that the gold NSs had the capability to generate a photocurrent when exposed to light in the presence of the electrolyte. The key mechanism underlying this photocurrent generation was plasmon-induced electron transfer. When the gold NSs were excited by incident light, the collective oscillation of electrons in the NSs induced electron transfer from the gold NSs to the conduction band of the TiO_2 semiconductor. This process effectively separated charges and contributed to the photocurrent. An interesting aspect of their work was the ability to tune the plasmon resonance of the gold NSs to the NIR region. By modifying the structure of the gold NSs, particularly their shape (elongating the NSs along a long axis), they were able to shift the plasmon resonance to longer wavelengths. This allowed them to capture light in the NIR region, even up to 1200 nm, which is beyond the typical visible spectrum. Building upon these findings, the researchers extended their work

to explore plasmon-induced water splitting. This is a process where plasmonic materials are used to facilitate the splitting of water molecules into hydrogen and oxygen gases when exposed to light. The ability to extend plasmon resonance into the NIR region could have implications for more efficient water splitting processes, as NIR light is less energetic than visible light but still has the potential to drive chemical reactions (Nishijima et al., 2012).

In summary, Misawa and co-workers expanded on the previous research by using well-controlled gold NSs on a TiO_2 single crystal to function as photoelectrodes. They demonstrated plasmon-induced electron transfer and the ability to tune plasmon resonance to the NIR region, which could have applications in improving the efficiency of light absorption and facilitating water splitting for renewable energy generation.

Takahashi & Tatsuma, (2011) have developed solid-state photovoltaic cells harnessing the LSPR of Au and Ag NPs to enhance their performance. These photovoltaic cells have a structure comprising In/TiO_2/MNPs/ITO, with MNPs representing either AuNPs or AgNPs. Notably, two-dimensional MNP ensembles were employed in the cell design to maximize the interaction with incident light. The resulting cells exhibited significantly higher quantum efficiencies compared to those with hole-transport materials (HTMs). Importantly, the study revealed that photovoltage is generated at the interface between the TiO_2 semiconductor layer and the metal nanoparticles (AuNPs or AgNPs), indicating the crucial role of LSPR-induced charge separation in the device's operation. These findings highlight the potential of solid-state photovoltaic cells with two-dimensionally distributed photosensitizers for cost-effective and structurally simple solar cell technologies, outperforming cells with traditional HTMs.

Pradhan et al., (2012) introduces an innovative and straightforward approach to construct a photovoltaic device featuring a semiconductor-insulator-semiconductor (SIS) heterojunction. This device exploits surface plasmon polaritons (SPPs) generated within one of the semiconductor layers, specifically Al:ZnO, and guides these SPPs through a dielectric barrier composed of SiO_2 to access the other semiconductor layer (Si). This robust architectural design harnesses the potential of surface plasmon excitation within the SIS structure, facilitating electron excitation via plasmon absorption in Al:ZnO over a wide range of wavelengths, spanning from visible to infrared. This enhancement of photovoltaic activity

opens up diverse applications, not limited to photovoltaics alone but extending to sensing, waveguiding, and various other applications that can benefit from SPPs enhancement in semiconductors, all achieved without relying on noble metals.

Cushing et al., (2012) addresses the integration of plasmonic metal nanostructures into semiconductors to enhance the harvesting of solar light and improve energy conversion efficiency. Until now, the precise mechanism responsible for energy transfer from plasmonic metals to semiconductors has remained unclear. In this research, the underlying plasmonic energy transfer mechanism is unequivocally identified within $Au@SiO_2@Cu_2O$ sandwich nanostructures. This determination is achieved through transient-absorption and photocatalysis action spectrum measurements. The gold core within these nanostructures serves as the key component for converting incident photon energy into localized surface plasmon resonance oscillations. These plasmonic oscillations subsequently facilitate the transfer of energy to the Cu_2O semiconductor shell through a process known as resonant energy transfer (RET). RET operates by generating electron-hole pairs within the semiconductor via dipole-dipole interactions between the plasmonic metal (acting as the donor) and the semiconductor (serving as the acceptor). This transfer of energy significantly enhances the visible-light photocatalytic activity when compared to the performance of the semiconductor alone. The research findings reveal that RET from a plasmonic metal to a semiconductor is a viable and efficient mechanism. It has broad implications for guiding the design and optimization of various optoelectronic devices, including photocatalysts and photovoltaic systems. This insight into plasmonic energy transfer mechanisms has the potential to advance the development of more efficient and effective technologies in the field of optoelectronics.

Arquer et al., (2013) delves into the realm of plasmonic excitation in metals, an area of great interest for controlling light-matter interactions at the nanoscale, with diverse applications in enhancing light absorption, surface-enhanced Raman scattering, and biosensing. While much attention has been given to these aspects, the field of electrically active plasmonic devices has recently gained traction. Here, a novel metal-insulator-semiconductor heterostructure, all-solid state hot-electron based solar cells, consisting of a high bandgap semi-conductor (TiO_2) Schottky junction with a nanotextured metal contact is introduced for plasmo-electric energy conversion, aiming to harness hot electrons generated

from plasmonic excitations. The research showcases the achievement of external quantum efficiencies (EQE) of 4% at 460 nm using a silver nanostructured electrode and 1.3% at 550 nm with a gold nanostructured electrode. The insulator interfacial layer is revealed to have a critical role in interface passivation, a necessity in photovoltaic applications for attaining high open-circuit voltages (0.5 V), with short-circuit current density (Jsc) of 0.14 mA/cm^2 and fill-factors (0.5).

Barad et al., (2016) presents a novel approach for creating solid-state TiO_2|Ag independent plasmonic solar cells through a simple and direct sputtering deposition process. These independent plasmonic solar cells rely on the formation of a Schottky barrier between two materials: TiO_2 and Ag. In this unique configuration, Ag serves a dual role as both the absorber, generating "hot" electrons, and the contact material for the solar cell. The sputtering process for Ag is performed for varying durations, resulting in the formation of AgNPs with a wide size distribution on the surface of TiO_2, which is deposited using rough spray pyrolysis. Notably, incident photon to current efficiency (IPCE) measurements demonstrate photovoltaic activity below the TiO_2 bandgap. This behaviour is attributed to the presence of AgNPs with a broad plasmonic band, leading to the generation of "hot" electrons. XPS analysis supports the mechanism of "hot" electron injection, as it tracks the Ag plasmon band and detects local photovoltages. The measurements indicate that when illuminated, electrons are generated within the AgNPs and subsequently injected into the TiO_2, resulting in photovoltaic activity. The current-voltage (J-V) measurements reveal photocurrents of up to 1.18 mA cm^{-2} and photovoltages reaching 430 mV. The overall solar cell efficiency is reported to be 0.2%, which is noteworthy as it represents the highest performance reported for such independent plasmonic solar cells to date. In summary, this study introduces a promising approach to create solid-state plasmonic solar cells by utilizing AgNPs to harness "hot" electrons and generate photovoltaic activity below the TiO_2 bandgap. The achieved performance levels represent a significant advancement in the development of independent plasmonic solar cells.

Nakamura et al., (2016) have successfully created all-solid-state plasmonic photovoltaic devices by employing a TiO_2/NiO p-n junction as the central structure, along with the integration of AuNPs as a prototype for plasmonic solar cells. The study extensively examined both the crystalline structures and photoelectric characteristics of these devices.

During the investigation, significant alterations were observed in the crystalline structure of the NiO thin film and the interfacial structure of TiO_2/Au-NPs/NiO following an annealing treatment. These observed changes are likely to have played a pivotal role in influencing the device's performance. A significant discovery in this study was the exhibition of visible-wavelength plasmon-induced photocurrent generation. This photocurrent was ascribed to the phenomenon of plasmon-induced charge separation, wherein incident light stimulates plasmonic modes within the AuNPs, causing a separation of charge carriers. Importantly, the photoelectric conversion characteristics associated with plasmon-induced charge separation were notably impacted by the morphology of the interface within TiO_2/Au-NPs/NiO. This suggests that careful engineering of the interface can enhance the performance of plasmonic photoelectric conversion devices. Moreover, the study reported a high level of long-term stability for these plasmonic photoelectric conversion devices. Even after continuous irradiation for a period of three days, the devices maintained a stable photocurrent. This robustness underscores the potential practical applicability of these devices in various optoelectronic applications, including solar energy conversion. In summary, this work represents a significant step in the development of all-solid-state plasmonic photoelectric conversion devices, shedding light on the interplay between materials, interfaces, and plasmon-induced charge separation. The observed long-term stability is particularly promising for future applications in sustainable energy harvesting.

Ginsburg et al., (2018) discusses a novel approach in the development of photovoltaic cells using plasmonic metallic nanoparticles, particularly focusing on the use of an ultra-thin tunable gold (Au) layer as the sole light-absorbing material. While plasmonic-enhanced solar cells, which utilize metallic nanoparticles for increased light absorption and scattering, have been widely studied, there are relatively few reports on solar cells that rely solely on a plasmonic metallic layer as the primary absorber. These newly developed cells are configured in a solid-state format with the following structure: ITO|Au NP's|TiO_2. The researchers employed high-throughput methods to optimize the cell's performance, achieving a current of 1 mA/cm^2 and a voltage of 100 mV under one sun illumination conditions. Notably, the incident photon to electron conversion efficiency at 700 nm is reported to be 5.84%, which is the highest efficiency reported for a solid-state device to date. These findings represent a significant advancement in the field of plasmonic-based solar cells and serve as a

foundational step toward the development of plasmonic-based tandem cells, which have the potential to further enhance the efficiency of solar energy conversion. The fabrication process for this device is straightforward, and its durability is enhanced by incorporating nanoparticles between two layers. One key feature of this cell is its ability to generate hot electrons, which migrate to the back contact, enabling potential applications in photocatalytic reactions that require electron transfer to the electrode surface. Moreover, this cell represents the initial step towards the development of tandem-based plasmonic solar cells, which hold the promise of increased voltage and overall cell performance. Achieving tandem cells could involve combining different layers of gold nanoparticles with varying sizes, thereby enhancing light harvesting and overall cell efficiency.

Song et al., 2021 explores the potential of plasmon-induced hot carrier transfer for solar energy conversion. The research achieves an exceptional quantum efficiency of up to 53% in transferring hot electrons from 1.7 nm silver nanoparticles to nanoporous TiO_2 films upon 400 nm excitation. The efficiency is attributed to both hot electrons generated by plasmon decay within silver particles and interfacial charge-transfer transitions from silver to TiO_2. Interestingly, efficiency improves with decreasing silver particle size, suggesting size reduction as a viable strategy for enhancing plasmonic hot-carrier extraction. The findings highlight the contributions of both conventional sequential plasmon-induced hot-electron transfer and plasmon-induced interfacial charge-transfer transition pathways at the silver/TiO_2 interface, with efficiencies increasing significantly for smaller silver particles. At the largest particle size examined (approximately 5.9 nm), the total hot-electron transfer quantum efficiency reaches 28% at 400 nm excitation, primarily driven by the interfacial charge-transfer pathway. However, at the smallest nanoparticle size (around 1.7 nm), the efficiency escalates to 53%, with substantial contributions from both pathways. These results underscore the efficacy of diminishing plasmonic particle size as an effective means to augment plasmon-induced hot-electron transfer efficiency at metal/semiconductor interfaces.

Singh et al., 2024 presents the fabrication and characterization of a hot electron photodetector based on a silver (Ag)/titanium oxide (TiO_2) nano-heterojunction thin film grown via a solution-processed technique. The nano-heterojunction thin film, derived from a sol-gel derived $Na_2Ti_3O_7$ (NTO) thin film, facilitates efficient charge transport of plasmon-induced hot electrons to the semiconductor junction. The device, fabricated in a

photoconductor geometry on a glass substrate, incorporates a solution-processed SnO_2 layer as the charge transport layer. The Ag-TiO_2 nano-heterojunction thin film transfers plasmon-induced hot electrons from Ag nanoparticles to the SnO_2 layer via TiO_2, enabling high-efficiency electron transport to the respective electrode. Characterization through external quantum efficiency (EQE) measurements confirms intense photocurrent generation in the plasmonic absorption region of the nano-heterojunction thin film. The photodetector exhibits narrowband photodetection with a peak wavelength of 443 nm and a full width at half maximum (FWHM) of 50 nm. At this wavelength and under a 10 V external bias, the device achieves a maximum EQE of 1.54%, responsivity of 0.52 A/W, and detectivity of 1.25 × 1010 Jones. Transient photocurrent studies reveal rapid response times, with rise and fall times of 1.8 s and 2.3 s, respectively. Moreover, the device demonstrates good stability over a testing period of 120 days.

These comprehensive literature reviews have harnessed the unique properties of plasmonic materials, such as gold and silver nanoparticles, to significantly improve light absorption, charge separation, and solar energy conversion technology. Plasmonic solar cells have not only enhanced our understanding of light-matter interactions at the nanoscale but also offer promising avenues for more efficient, cost-effective, and sustainable energy generation. As we continue to explore and harness the unique properties of plasmonic materials, the future of photovoltaics and renewable energy looks brighter than ever.

Table 2.2: Some of the key parameters of solid state plasmonic photovoltaic devices that have been developed in recent years and their fabrication methods

Device Structure / Material	**Fabrication methods**	**Open Circuit Voltage (V_{oc}) (Volts)**	**Short Circuit Current (I_{sc}) (mA/cm^2)**	**Efficiency (η)**	**References**
ITO | Au | TiO_2	Au – Sputtering TiO_2 – Spray Pyrolysis	0.1	1	-	Takahashi & Tatsuma, (2011)
FTO|TiO_2|Al_2O_3|Ag	TiO_2 – Spin coating Ag – Sputtering Al_2O_3 – Atomic Layer Deposition	0.48	0.14	0.03%	Arquer et al., (2013)

Au@ITO|Au NR's|TiO_2	Au NR's – Electro deposition TiO_2 – Atomic Layer Deposition	0.21	0.026	-	Mubeen et al., (2014)
TiO_2|Au|NiO	Au – Thermal Evaporation NiO – Atomic Layer Deposition	0.56 (without annealing) 0.73 (with annealing)	0.108 (without annealing) 0.04 (with annealing)	0.033% (without annealing) 0.011 (with annealing)	Nakamura et al., (2016)
ITO | Au| TiO_2	Au – Sputtering TiO_2 – Spray pyrolysis	0.1	1	-	Ginsburg et al., (2018)

2.4 Research Gaps

The literature review revealed limited research on the photoelectric energy conversion of plasmon-generated hot carriers. Within this scanty literature, the following research gaps have been identified:

Experimental Validation: While extensive theoretical and numerical studies have been conducted, a comprehensive experimental validation of the predicted optical properties is mostly void. This validation is critical to ensure that theoretical models accurately represent real-world behaviour.

Enhanced Computational Efficiency: Many numerical methods are computationally intensive, especially for large-sized materials. However, to handle such larger systems, more efficient algorithms or parallel computing strategies are yet to be developed.

Systematic Annealing Studies: While several studies acknowledge the influence of annealing temperature, there is a need for more systematic investigations that comprehensively explore the range of annealing temperatures and their effects on TiO_2 properties. These findings would provide valuable insights into the optimal annealing conditions for specific applications.

Scalability and Cost-Efficiency: Scaling up the production of TiO_2 materials and exploring cost-effective synthesis methods are crucial for practical applications. Research into scalable and economically viable manufacturing processes is needed.

Safety and Environmental Impact: As TiO_2 materials find broader applications, it is essential to investigate their safety and environmental impact. Comprehensive studies on potential toxicity and eco-friendliness are necessary.

Efficiency vs. Cost: While plasmonic-enhanced solar cells show promise in improving efficiency, there is a need to address the cost-effectiveness of these technologies. The production and integration of plasmonic materials can be expensive, and future research should explore cost-efficient fabrication methods such as deposition, patterning, and integrating new materials into complex plasmonic devices.

2.5 Research Objectives

The main objective of this thesis work is to design and develop a solid-state plasmonic energy harvesting device using easy-to-make techniques. In order to achieve the objective, the following specific sub-objectives have been formulated:

- ✓ To develop a physics-based numerical model of noble metal plasmonic nanomaterials and to study the effect of various dimensions of the nanoparticles on its plasmon resonance peaks.
- ✓ To synthesize the thin film semiconductor as a substrate for the plasmonic device through a less complicated chemical method.
- ✓ To design and fabricate the solid-state plasmonic energy harvesting device by applying plasmonic nanomaterials synthesized via physical method.

CHAPTER 3

NUMERICAL STUDY OF NOBLE METALS PLASMONIC NANOPARTICLES – SILVER AND GOLD AND ITS EXPERIMENTAL VALIDATION

CHAPTER 3

NUMERICAL STUDY OF NOBLE METALS PLASMONIC NANOPARTICLES – SILVER AND GOLD AND ITS EXPERIMENTAL VALIDATION

3.1 Overview

In the domain of nano photonics and nanoscience, the intricate manipulation of electromagnetic waves by engineered nanostructures has yielded unprecedented opportunities for tailoring light-matter interactions. Within this context, noble metal plasmonic nanoparticles, specifically those fabricated from Ag and Au, have emerged as pivotal entities of investigation due to their distinctive ability to support surface plasmon resonances. This chapter undertakes a comprehensive numerical and experimental inquiry into the optical characteristics of these noble metal nanoparticles, aiming to elucidate their resonant behaviours and elucidate the underlying mechanisms. The amalgamation of rigorous computational simulations, employing finite element methods (FEM), and careful experimental validation offers a multi-faceted perspective on the intricate properties governing Ag and Au nanoparticle plasmonics. By conducting a thorough examination, this chapter not only enriches the fundamental understanding of plasmonic phenomena but also establishes a foundation for the development of novel applications across fields like sensing, imaging, and energy conversion.

The choice of simulation method plays a crucial role in our investigation. FEM have garnered significant attention as a powerful tool for the numerical simulation of plasmonic systems due to their versatility in handling complex geometries and material properties. FEM, in contrast to finite-difference time-domain (FDTD) methods, provides a broader range of applicability when dealing with intricate nanoparticle geometries and material variations (Jain et al., 2007). The capability of FEM to accurately model structures with curved surfaces and heterogeneous materials enables a more realistic representation of noble metal nanoparticles, which often exhibit non-uniform shapes and may interact with surrounding media possessing diverse dielectric constants. This aspect becomes particularly crucial when studying the resonant properties of nanoparticles in intricate configurations, such as that in

close proximity to dielectric interfaces or arranged in complex geometrical assemblies (Zhang et al., 2015).

FDTD methods are efficient and commonly used for simulating plasmonic systems due to their relative ease of implementation and computational efficiency. However, they may struggle to accurately represent complex geometries and material properties inherent in noble metal nanoparticles. This limitation arises because FDTD relies on a grid-based discretization scheme, which may not adequately capture intricate nanoparticle shapes and surface features. On the other hand, FEM offers a higher degree of flexibility and accuracy in modeling plasmonic materials. It can handle complex geometries and material complexities with greater fidelity, making it well-suited for accurately representing noble metal nanoparticles. FEM achieves this through its meshing approach, which divides the computational domain into smaller elements and allows for adaptive mesh refinement. This capability enables FEM to capture fine details and irregularities present in nanoparticle structures more effectively than FDTD. Furthermore, FEM supports sophisticated material models, including anisotropic and nonlinear materials, which are crucial for accurately describing the optical properties of plasmonic materials. This enhanced modeling capability is paramount for achieving a comprehensive understanding of the optical behavior of noble metal nanoparticles. (Lassiter et al., 2010).

In this chapter, we embark on a journey of exploration, employing finite element methods for comprehensive numerical simulations that unravel the plasmonic behaviour of noble metal nanoparticles. These simulations are conducted in parallel with meticulously designed experiments, where synthesized nanoparticles undergo rigorous optical characterization, including absorption spectroscopy. By synergizing advanced computational approaches with empirical observations, we endeavour to bridge the gap between theoretical insights and experimental verifications, ultimately advancing the frontiers of nano photonics and its manifold applications. Through this combined approach, we attempt to provide a more holistic understanding of the intricate interactions between light and noble metal nanoparticles, fostering new avenues for technological innovation.

3.2 Experimental Approach

Fig 3.1 shows the schematic diagram of the overall approach of the numerical simulation. The experimental approach for this numerical simulation can be summarized as follows:

3.2.1 Problem Statement and Objective

Problem: In this work, it is the investigation of the optical properties of noble metal plasmonic nanoparticles (gold and silver).

Objectives: Determine the behaviour of these nanoparticles concerning their absorption, scattering, and extinction coefficients based on different shapes, sizes, and surrounding di-electric media.

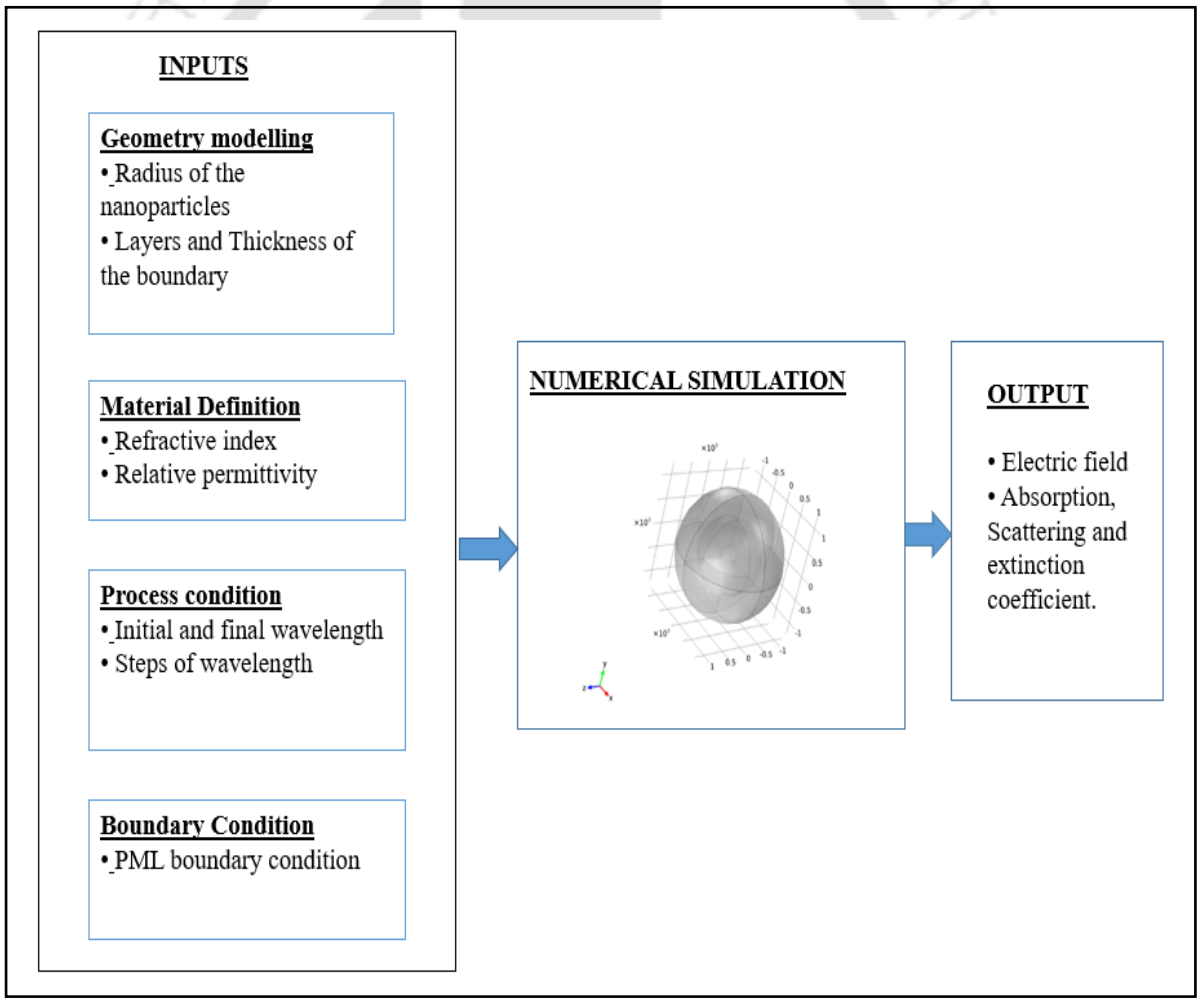

Figure 3.1: Overall approach of the numerical simulation.

3.2.2 Geometric Modelling

All parameters for simulations were set up by means of the "Electromagnetic Wave Frequency Domain" mode of COMSOL which is under the provision of Wave Optics or Radio Frequency modules. The domain in the simulation consists of a nanoparticle with an air/water domain truncated by a perfectly matched layer (PML). Perfectly Matched Layer, or PML, is a numerical technique used in electromagnetic simulations with the purpose of reducing reflections at computational domain boundaries that could potentially affect the accuracy of the results. These layers mimic an endlessly extending domain beyond the boundary by methodically absorbing outgoing waves where they are deliberately positioned at the boundaries of the domain. Properties like thickness and absorption profile can be tailored for optimization. PML improves simulation stability and convergence by efficiently reducing reflections, which is crucial for accurate modelling. For this model, the model geometry can be represented as in Figure 3.2.

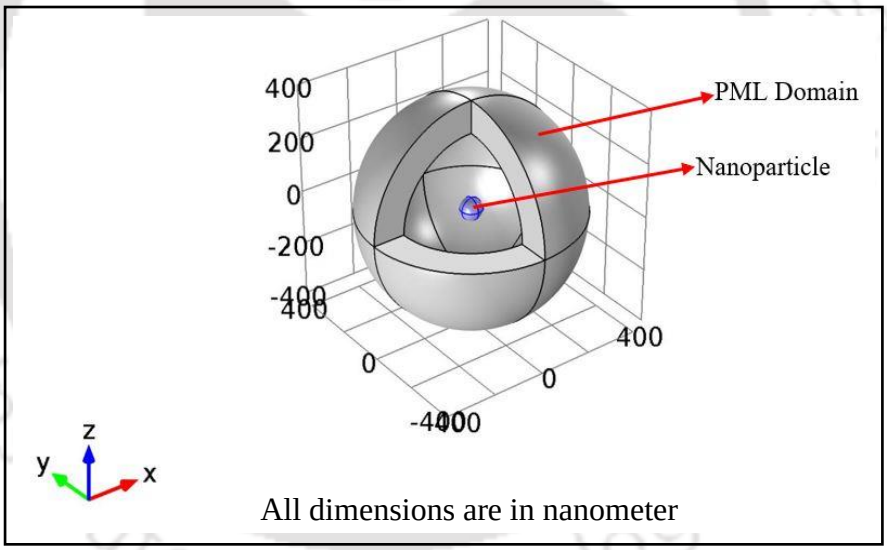

Figure 3.2: Model Geometry

3.2.3 Assumptions

The assumption is that the particle is embedded in a non-absorbing medium of relative dielectric function ε_1 and excited at a wavelength λ by an incident field $E_{inc}(r)$ consisting of a plane wave of amplitude E_0 incident along positive x-axis and polarized along z-axis.

3.2.4 Material Properties

For all the calculations, the dielectric functions of the metal nanoparticles are taken as measured on bulk silver and gold by Johnson and Christy (P. B. Johnson & R. W. Christy, 1972).

3.2.5 Governing Equation and Boundary Conditions

From the assumption, we can derive the wave vector using the equation, $k_1 = (2\pi/\lambda)\sqrt{\varepsilon_1}$ and later we can determine incident field using the equation, $E_{inc}(r) = E_0 \exp(-jk_1 z)$. Subsequently, the result can be denoted by the following equations:

$$E(r) = E_{inc}(r) + E_{sca}(r) \tag{3.1}$$

$$H(r) = H_{inc}(r) + H_{sca}(r) \tag{3.2}$$

Maxwell's wave equation is solved considering the scattered electric field, $E_{sca}(r)$:

$$\nabla \times \left(\frac{1}{\mu_r} \nabla \times E_{sca}(r)\right) - k_0^2 \left(\varepsilon_r - j\frac{\sigma}{\omega\varepsilon_0}\right) E_{sca}(r) = 0 \tag{3.3}$$

From Faraday's law, the scattered magnetic field is calculated

$$H_{sca}(r) = -\frac{1}{j\omega\mu} \nabla \times E_{sca}(r) \tag{3.4}$$

The magnetic field related to the incident electric field is given by

$$H_{inc}(r) = \frac{1}{\eta} \hat{k} \times E_{inc}(r) \tag{3.5}$$

Where $\hat{k}$ the direction of the incident wave propagation is, $\eta = \sqrt{\mu/\varepsilon}$ is the characteristic impedance of the ambient medium.

The energy flux is given by the time average Poynting vector for time harmonic fields as

$$S = \frac{1}{2} Re[E(r) \times H(r)^*] \tag{3.6}$$

In this simulation scattering boundary condition is used and the following boundary conditions were imposed on the symmetry planes:

Symmetry in electric field

$$n \times H|_{y=0} = 0 \quad (PMC) \tag{3.7}$$

Where PMC stand for Perfect Magnetic Conductor boundary conditions. PMC simulates surfaces behaving as perfect magnetic conductors, where the tangential magnetic field component at the boundary is zero, blocking magnetic fields from penetrating further.

Symmetry in magnetic field

$$n \times E|_{z=0} = 0 \qquad (PEC) \tag{3.8}$$

Where PEC stands for Perfect Electric Conductor Boundary conditions, which means that the models surfaces behaving as perfect electric conductors, where the tangential electric field component at the boundary is zero, reflecting electric fields without allowing them to penetrate beyond the boundary.

3.2.6 Solution Methodology

After the formulation of problem, governing equation and boundary conditions, FEM was used for solving the Maxwell equation for determination of absorption, scattering and extinction cross section. For determining the derived EM properties like absorption, scattering and extinction cross section post processing is carried out. The simulation was perform to investigate the optimal mesh size and thereafter, the optimal mesh size was utilized for carrying out the parametric study.

3.2.7 Post Processing for Calculation of Absorption, Scattering and Extinction Cross Section

Following the above assumptions, we can compute numerous derived EM properties of the nanoparticle as listed below. Optical properties such as absorption cross section, scattering cross section and extinction cross section which are dependent on the wavelength have been simulated using the above derived equations.

By integrating the flux of the complex Poynting vector of the scattered field, S_{sca}, across the nanoparticle surface, the scattering cross section can be computed using the equation:

$$\sigma_{sca} = \frac{1}{S_0} \iint_{NP}^{-} Re\,(S_{sca}(r).n)\,dS \tag{3.9}$$

Where $S_0 = \frac{\sqrt{\varepsilon_1} E_0^2}{2Z_0}$ represents the power density of the incident field and $Z_0 = \sqrt{\frac{\mu_0}{\varepsilon_0}} \approx 376.73\Omega$ represents the characteristic impedance of vacuum

The absorption cross section can be computed from a volume integral inside the nanoparticle:

$$\sigma_{abs} = \frac{1}{S_0} \iiint_{NP}^{-} Q_h dV \tag{3.10}$$

Where $Q_h = \frac{1}{2}\omega\varepsilon_0 I_m(\varepsilon_2(\omega))|E(r)|^2$ is the total power dissipation density, $\varepsilon_2(\omega)$ denotes the relative dielectric function of the particle (possibly complex and wavelength dependent) The extinction cross-section can be computed from energy conservation as

$$\sigma_{ext} = \sigma_{abs} + \sigma_{sca} \tag{3.11}$$

3.2.8 Mesh Model and Mesh Sensitivity Analysis

The model is non-uniformly meshed just to possess maximum mesh elements in the nanoparticle than the scattering and far field domain of nanoparticles. The nanoparticle was discretized with free tetrahedral type mesh. The PML domain was swept to 5 layers and discretized with free triangular type mesh. Figure 3.3 shows the meshed domain with element of different size. Mesh sensitivity analysis was carried out for a 50 nm radius silver nanoparticle embedded in air. Table 3.1 presents the influence of mesh on computation time and output response i.e plasmon resonance peak of the nanoparticle.

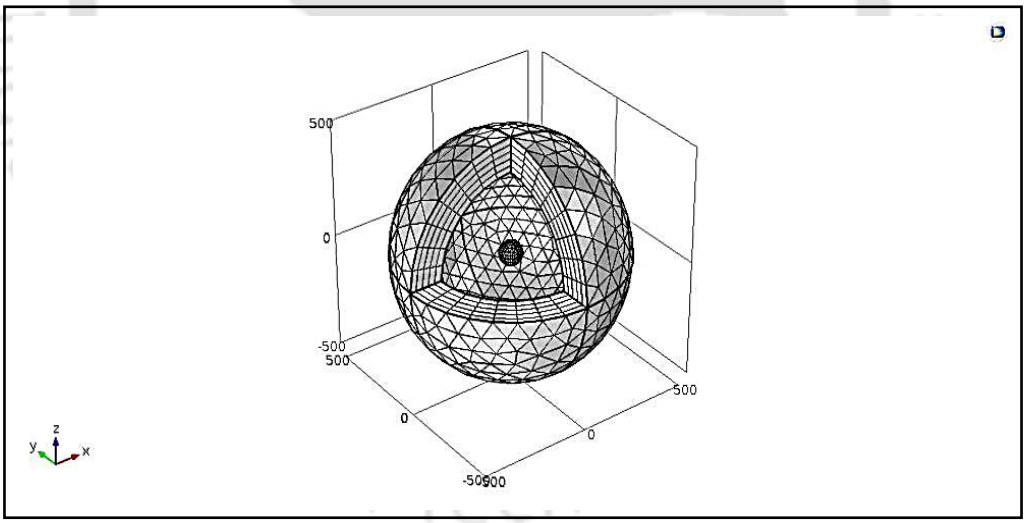

Figure 3.3: Discretization of the developed 3D model.

From Table 3.1 below, it is observed that for mesh distribution starting from coarse to extra fine mesh, the resonance peak remains the same i.e. 395 nm. The computational time is least when we used the fine mesh. Therefore, the domain with fine mesh has been chosen for the present study.

Table 3.1: Results of mesh sensitivity analysis of 50 nm radius Ag nanoparticle embedded in air medium.

Sl No.	Mesh size	Mesh elements of nanoparticle	DOF	Computational time	Resonance peak (nm)
1	Coarse	4378	88272	28 min 22 sec	395
2	Normal	5866	97690	23 min 8 sec	395
3	**Fine**	**8217**	**112584**	**20 min 3 sec**	**395**
4	Finer	18502	177766	26 min 18 sec	395
5	Extra fine	61146	447920	1 hr 10 min 26 sec	395

3.2.9 Hardware and Computational Resources

A computer system of Intel(R) Core (TM) i7-8750H CPU @ 2.20GHz with 16GB RAM processor was employed for the present numerical studies. COMSOL-Multiphysics version 5.6 is being used for the simulation studies.

3.3 Results and Discussions

3.3.1 Comparing the Simulated Absorbance Spectra with that of Experimental Results

The discrete simulation was performed using the concept of finite element analysis and is directly compared with the measured absorbance spectra of silver colloid as shown in Figure 3.4. A good level of agreement with the measured data is obtained for single isolated Ag nanoparticle of 10 nm radius. The level of agreement obtained between the two is quite high, with a difference less than 2% in the plasmonic resonance peak wavelength range (where the difference% = (Discrete Simulation - Measured)/Discrete Simulation as function of λ). At last the discrete simulation is used to model for different complex metal nanoparticles structures. Figure 3.5 shows the FESEM image of the 10 nm Ag nanoparticles taken for measuring the experimental absorbance data.

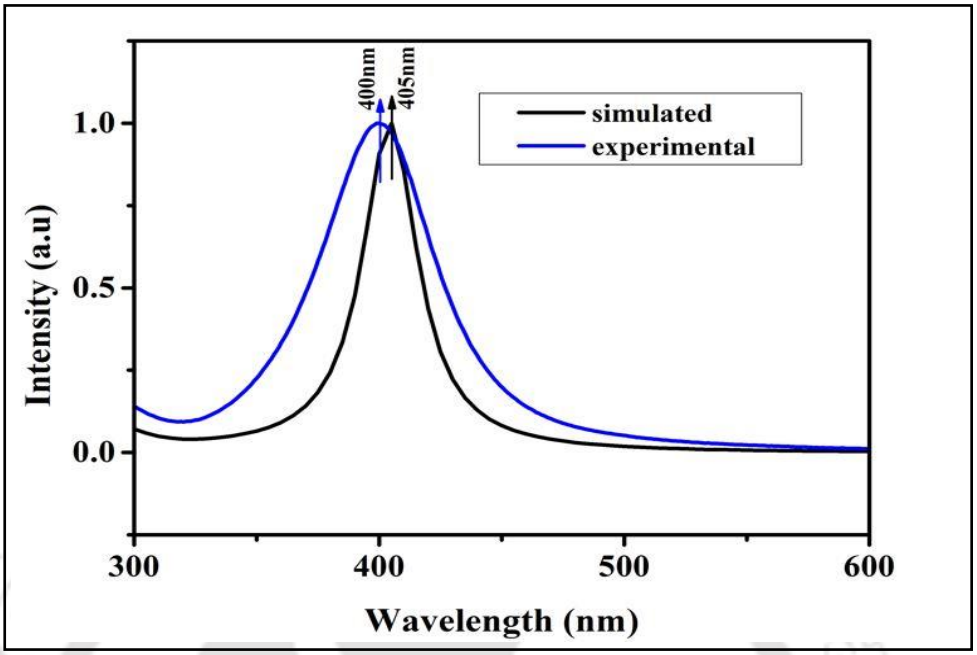

Figure 3.4: Absorbance spectra of 10 nm silver nanoparticles in an aqueous solution (n=1.33).

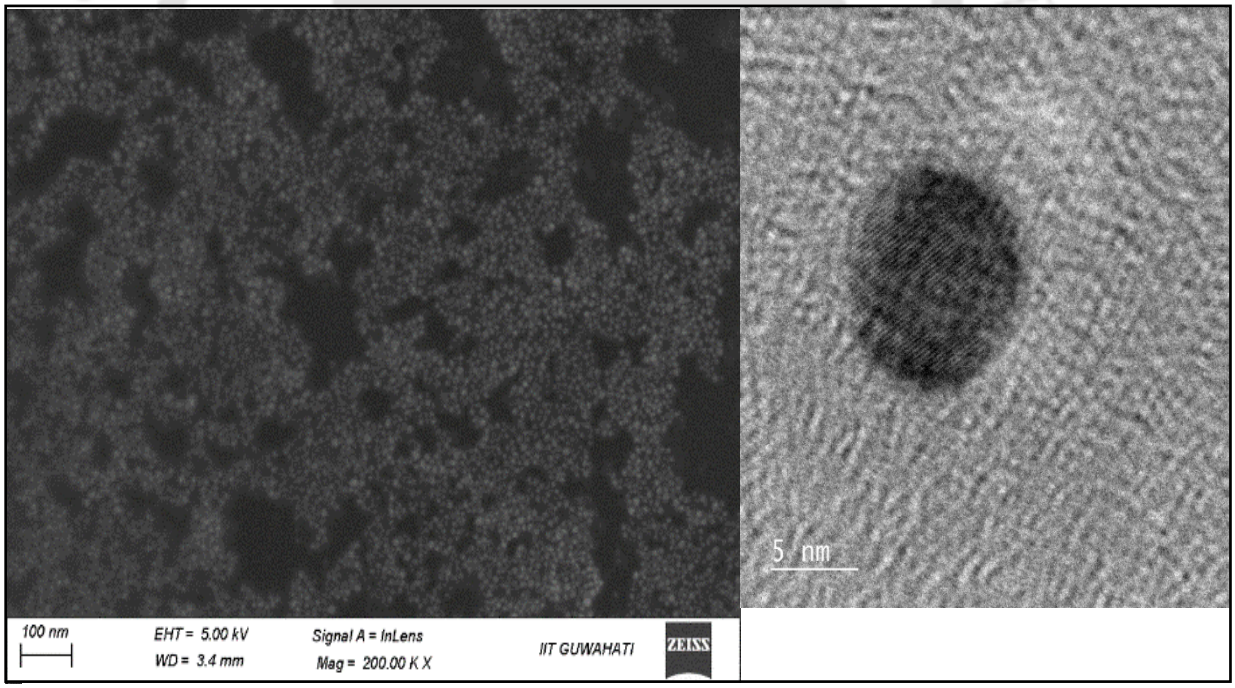

Figure 3.5: FESEM and HRTEM image of the silver nanoparticles.

3.3.2 Study the Effect of Size of the Nanoparticles on Plasmon Resonance Peak

In order to study the size effect on plasmon resonance peak, we have simulated the optical properties of Ag and Au nanospheres of different radii.

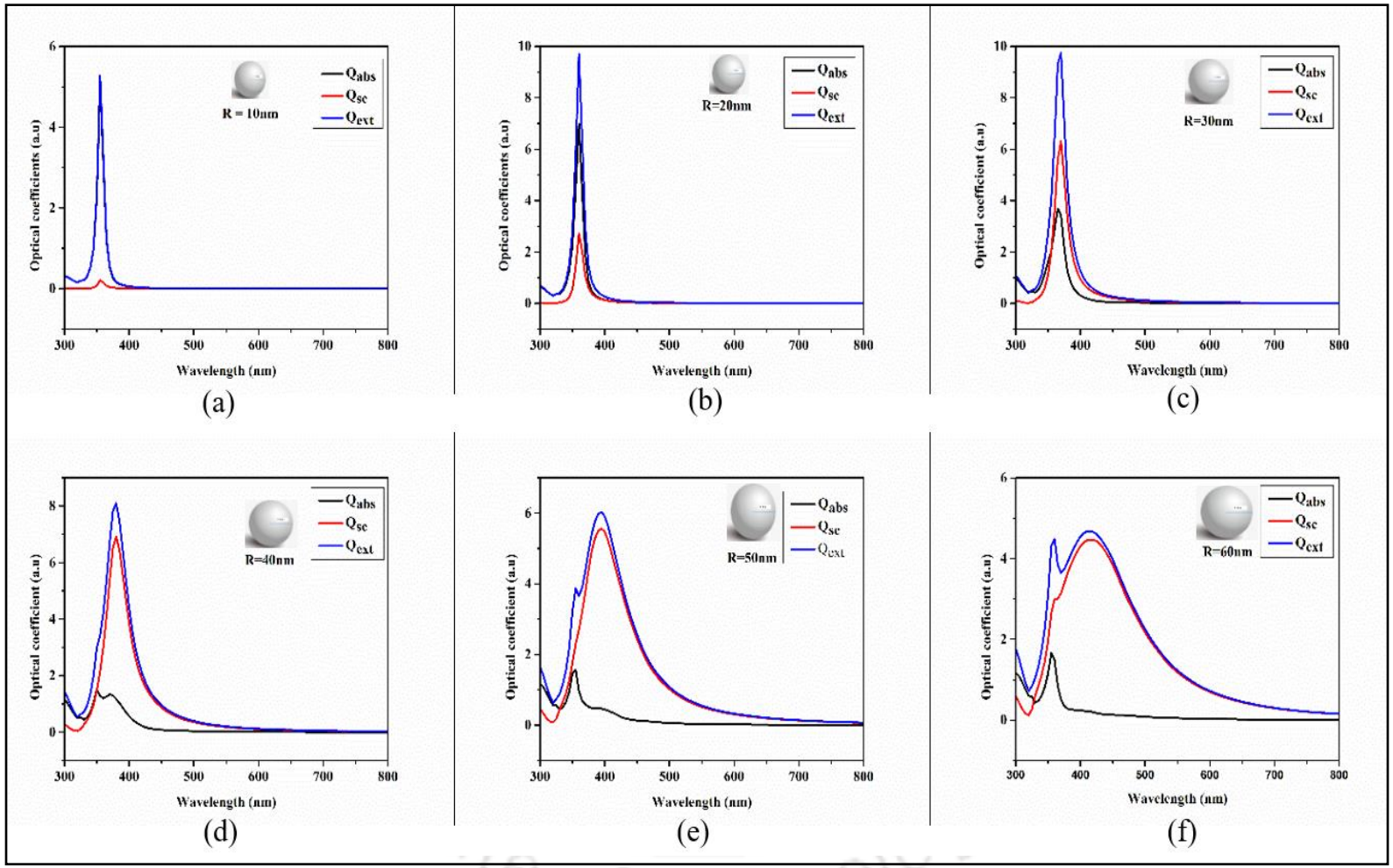

Figure 3.6: Absorption (black), scattering (red) and extinction(blue) cross section spectra of silver nanosphere of radius (a) 10 nm, (b) 20 nm, (c) 30 nm, (d) 40 nm, (e) 50 nm and (f) 60 nm.

The simulated absorption, scattering and extinction cross section spectra of silver metal nanoparticles of different size embedded in air medium are shown in Figure 3.6. In this Figure, blue, red and black lines indicate the extinction cross section spectra, scattering spectra and absorption spectra respectively. By analysing these spectra, it can be perceived that as the size of the metal nanoparticles increases, absorption decreases and scattering become more prominent. Scattering intensifies with particle size due to various factors. Larger particles possess a greater surface area, allowing more interactions with light and thereby enhancing scattering. Moreover, these particles can scatter light multiple times, amplifying the overall scattering effect. As particle size increases, Rayleigh scattering diminishes, transitioning to the Mie scattering regime, where larger particles exhibit stronger scattering efficiency. Changes in optical density and diffraction effects further augment scattering intensity in larger particles. Further, it is also noted that intensity of the extinction spectra increases as the nanoparticle radius increases from 10 nm to 30 nm whereas intensity of the extinction spectra decreases and the resonance peaks get red shifted and broadens as the size increase further from 40 nm to 60 nm. Interestingly, a quadrupole resonance peak appears as the size of silver nanoparticle exceeds a radius of 40 nm in addition to the dipole resonance peak. It is observed that this is resulted from the phase shift of the absorption spectra (Raza et al., 2015).

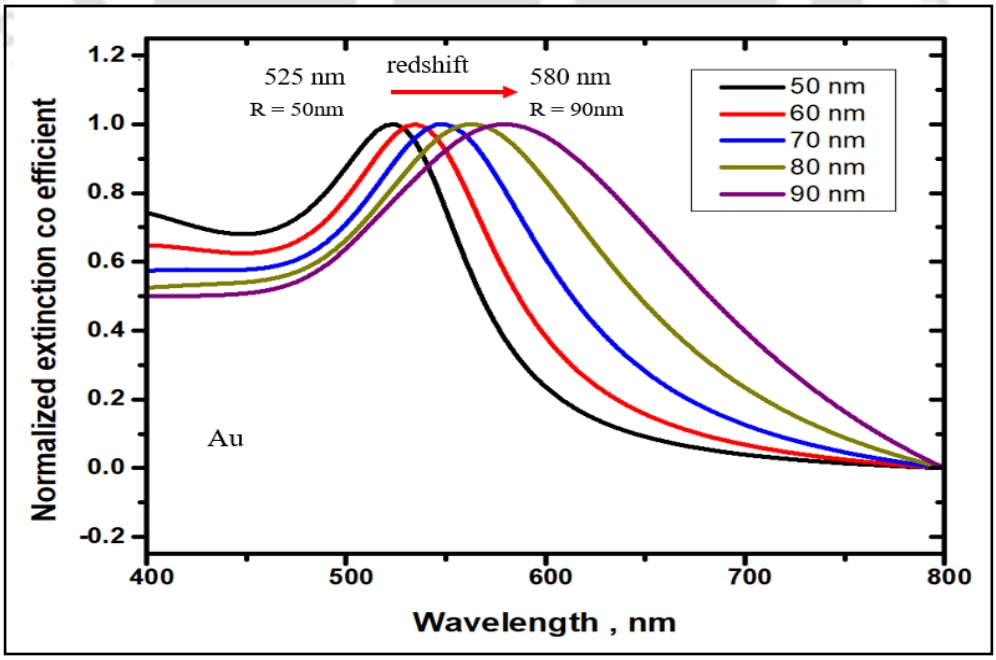

Figure 3.7: Extinction cross section of gold nanosphere of different radii of 50 nm, 60 nm, 70 nm, 80 nm and 90 nm.

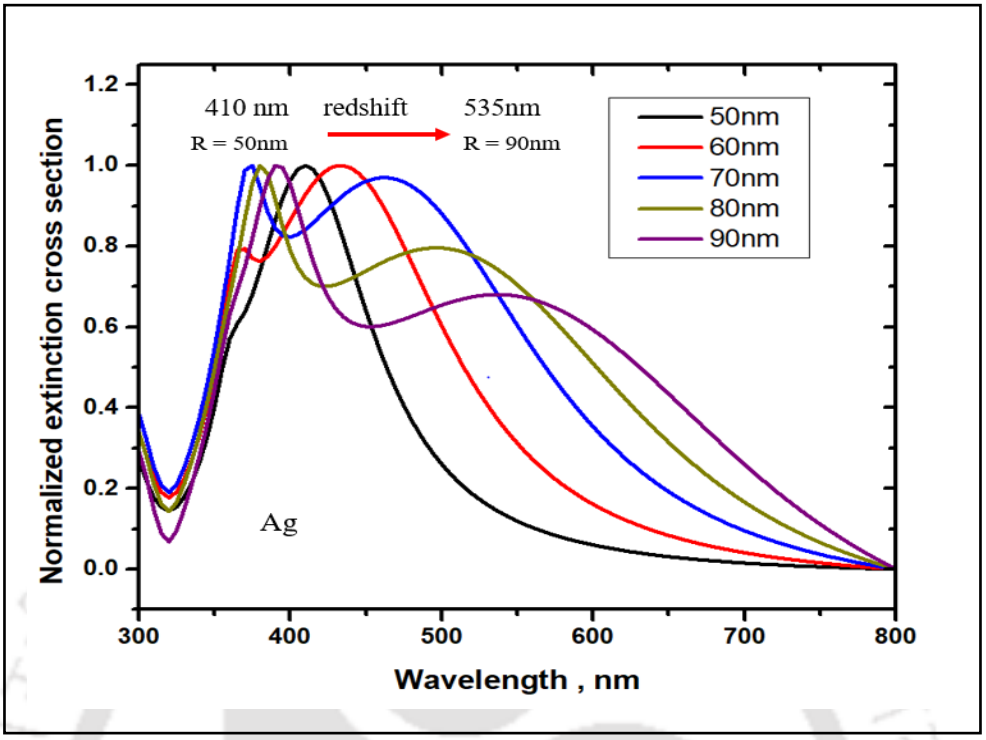

Figure 3.8: Extinction cross section of silver nanosphere of different radii of 50 nm, 60 nm, 70 nm, 80 nm and 90 nm.

The simulated extinction cross section of gold (Au) and silver (Ag) nanosphere of different radii is shown in Figure 3.7 and 3.8 respectively. Ag nanoparticles have more intense and sharp plasmonic resonance peak than Au nanoparticle. The small overlap between the inter-band transition of Ag that starts at 320 nm and its surface plasmon resonance make Ag nanoparticles to have more intense and sharper plasmonic resonance peak. But in Au nanoparticles the onset of inter-band transition partially overlaps with the resonance due to which increases and decreases its surface plasmon resonance width and intensity respectively (Noguez, 2007)(Kelly et al., 2003)(Sosa et al., 2003) . It is clearly observed that as the radius of the nanoparticle increases, the resonance peak is broadened, which means absorption band increases and also shifted towards red both in silver (Ag) and gold (Au) nanoparticle. The quadrupole resonance peak which emerges only in silver nanoparticle as the size increases from 40 nm and the peak becomes more prominent and blue shifted as the nanoparticles size increases (Alsawafta et al., 2012). The dipole resonance wavelength corresponding to simulated extinction cross section spectrum for single Ag and Au nanoparticle of various sizes embedded in air medium is shown in Figure 3.9. Ag nanoparticle is more sensitive to size variation compared to gold nanoparticle. The Ag nanoparticle have larger resonance peak

shifting band comprises from 355 nm to 415 nm to that of Au that ranges between 505 to 535 for the same size variation.

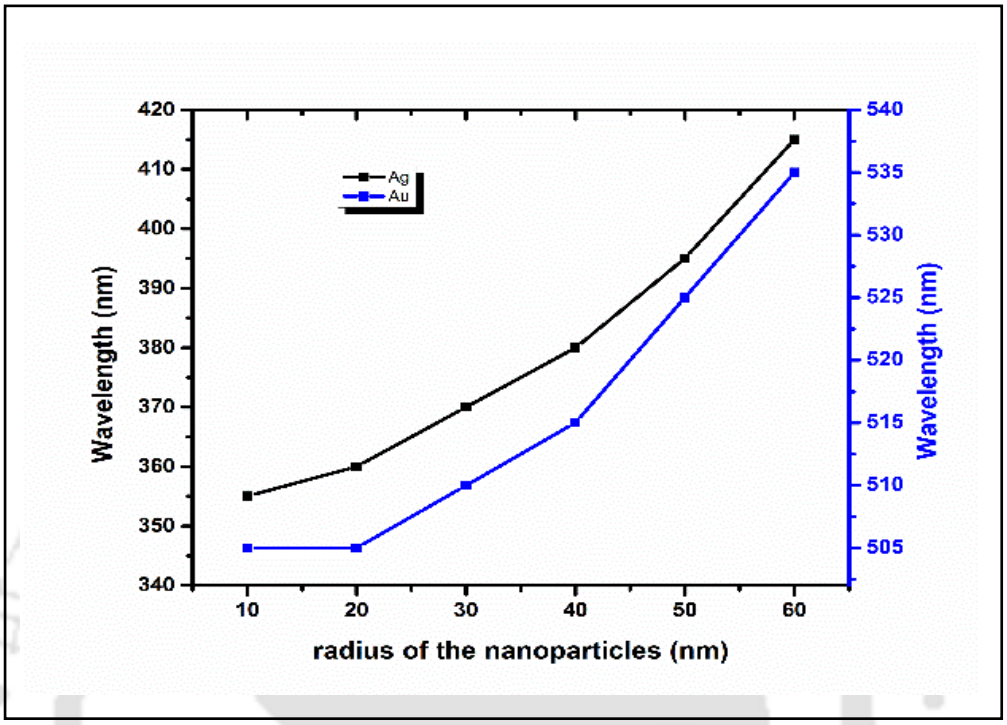

Figure 3.9: Variation of dipole plasmon resonance peaks with nanoparticle sizes of Ag (black) and Au (blue).

Table 3. 2: Comparison of extinction cross sections of Ag and Au nanoparticles.

Aspects	Extinction cross sections of Ag nanoparticles	Extinction cross sections of Au nanoparticles
Plasmonic Resonance Characteristics	More intense and sharper plasmonic resonance peak which is due to the small overlap between inter-band transition and surface plasmon resonance	Less intense and sharp plasmonic resonance peak which is due to the partial overlap between inter-band transition and surface plasmon resonance
Dipole resonance peaks	Broadens with increasing nanoparticle radius and red shifted	Broadens with increasing nanoparticle radius and red shifted
Quadrupole resonance peak	Emerges with size increase	No quadrupole resonance observed
Sensitivity to Size Variation	More sensitive to size variation	Less sensitive to size variation
Resonance peak shifting band	355 nm to 415 nm	505 nm to 535 nm

3.3.3 Study the Effect of Shapes of the Nanoparticles on Plasmon Resonance Peak

Now a days the lithography techniques are highly developed and we are able to synthesize different shapes of nanoparticle. In order to study the shape effects on the resonance peak, simulation has been carried out for different shapes of nanoparticles but of same volume enclosed within the same medium that is of air. And it is clearly observed that the shapes of the nanoparticle affect the resonance peak from the Figure 3.10 .

The peaks got red shifted as the shapes got more complicated and multipole resonance peaks are observed in cylindrical and cuboid shapes nanoparticle which is not observed in case of spherical and ellipsoid shape. This multipole resonance peak is resulted from the surface charge polarization occur on the sharp edges of nanoparticles (Ashkarran & Bayat, 2013)(Amendola et al., 2010).

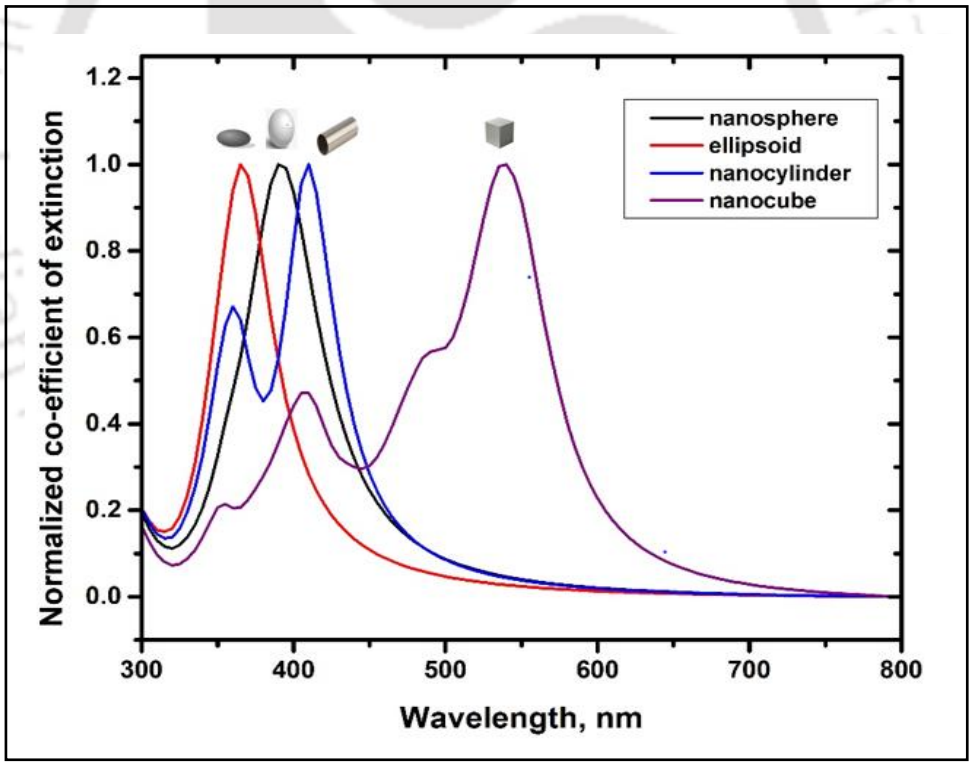

Figure 3.10: Extinction cross section spectra of Ag nanoparticle of different shapes with same volume.

3.3.4 Study the Effect of Surrounding Environment of the Nanoparticles on Plasmon Resonance Peak

The extinction spectra of Ag nanoparticle of radius 40 nm in different environment was also calculated in Figure 3.11 below to study the correlation between the resonance peak and refractive index of the ambient surrounding. Red shifting of the resonance peak with the increase in refractive index of the external medium is observed (Ivanova et al., 2016)(Khlebtsov et al., 2005).

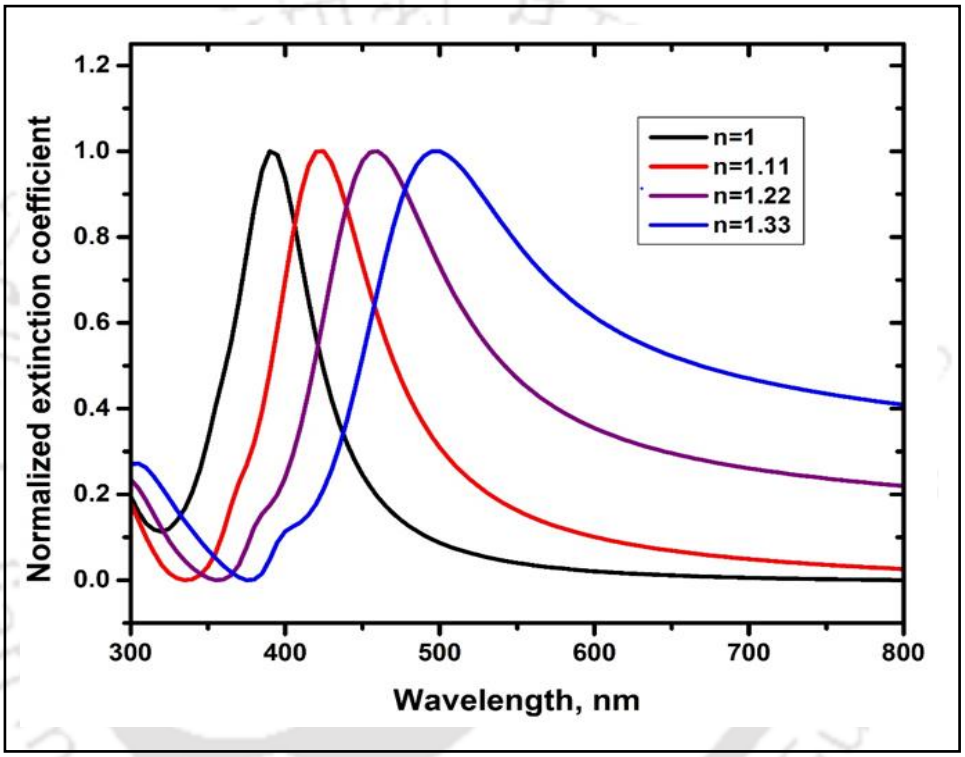

Figure 3.11: Extinction cross section spectra of Ag nanosphere of radius 40 nm embedded in different medium.

3.4 Conclusion

In conclusion, this study has delved into the fascinating world of plasmonic resonance in metallic nanoparticles, primarily focusing on silver (Ag) and gold (Au) nanoparticles. Through the application of discrete simulation based on finite element analysis, we have gained valuable insights into the optical properties of these nanoparticles. The agreement between our simulations and measured data for single isolated Ag nanoparticles of 10 nm radius demonstrates the robustness of our approach, with a remarkable difference of less than 2% in the plasmonic resonance peak wavelength range. Furthermore, our investigation

extended to examine the impact of size and shape variations on plasmon resonance. As the size of metal nanoparticles increased, we observed a decrease in absorption and an increase in scattering, along with intriguing phenomena such as red-shifting and broadening of resonance peaks. Notably, in silver nanoparticles exceeding 40 nm in radius, a quadrupole resonance peak emerged in addition to the dipole resonance, attributed to phase shifts in the absorption spectra.

Comparatively, gold nanoparticles exhibited different behavior due to the overlap of inter-band transitions, affecting their resonance peak width and intensity. The sensitivity to size variations was more pronounced in silver nanoparticles. When exploring various shapes of nanoparticles, we discovered that complex shapes led to red shifts in resonance peaks, with multipole resonance peaks appearing in cylindrical and cuboid shapes, driven by surface charge polarization along sharp edges. The study also examined the correlation between the resonance peak and the refractive index of the surrounding medium, finding that an increase in the refractive index resulted in a red shift of the resonance peak.

CHAPTER 4

EXPERIMENTAL STUDY ON FABRICATION OF NANOCRYSTALLINE TiO_2 THIN FILMS AND ITS CHARACTERIZATION

CHAPTER 4

EXPERIMENTAL STUDY ON FABRICATION OF NANOCRYSTALLINE TIO_2 THIN FILMS AND ITS CHARACTERIZATION

4.1 Overview

Among many other types of semiconductors, wide band gap type semiconductors have potential applications in numerous areas, namely laser diodes, ultraviolet (UV) light emitting devices, sensors, solar energy harvesting and other high end microelectronic devices (Haase et al., 1991)(Lester et al., 1995)(Grimes & Mor, 2009)(Qin et al., 2018) and even in some biomedical field applications (Mohan et al., 2012), which made them very attractive in present day scientific world. TiO_2 is one of such semiconductors that has gained massive recognition due to its various properties such as thermal stability, biocompatibility, non-toxicity, strong oxidizing agent and long-term photo-stability. These properties make them suitable for applications in many fields like environmental applications (Lalhriatpuia et al., 2016)(Sampaio et al., 2011)(Kääriäinen et al., 2009)(Quan et al., 2005), photocatalysis (Lalhriatpuia et al., 2016)(Sampaio et al., 2011)(Kääriäinen et al., 2009)(Livraghi et al., 2005), electrochromic devices (Sarwar et al., 2020), photovoltaic cells (Choi et al., 2012)(Barbé et al., 2005) and solid state plasmonic photoelectric conversion devices (Nakamura et al., 2016b)(Arquer et al., 2013). In dye sensitized photo-electrochemical solar cells, thin films of nanocrystalline TiO_2 are used as n-type electrode. These materials also possess remarkable properties for sensitizing quantum dot solar cells (Choi et al., 2012)(Patrocínio et al., 2008). Nonetheless, it is also one of the ingredients in optical brightener in wall colours, in bone implants and in sun cream, which are of non-electronic applications (Shams-Nateri et al., 2020)(Liao et al., 2020)(Yu et al., 2018). Moreover, nanocrystalline TiO_2 nanoparticles can be used for harnessing the excited hot electrons from metal nanoparticles and so it is widely used in plasmonic energy harvesting device (Arquer et al., 2013)(Furube et al., 2007)(Nishijima et al., 2010) .

There are three natural phases of TiO_2 namely, anatase, rutile and brookite, out of which anatase shows greater photocatalytic activity. This is due to anatase having a slightly higher Fermi level, a lower oxygen absorption capacity, and a higher degree of surface

hydroxylation. The hydroxyl group on the surface of TiO_2 plays an essential role in photo-degradation because it quickly traps photo-generated holes to create OH radicals, which are extremely reactive and subsequently implicated in oxidizing organic contaminants. As a result, the hydroxyl group is indirectly responsible for generating oxygen radicals and slowing electron–hole recombination.

So far, many studies have been performed on the light emitting properties of TiO_2 films that includes visible and ultra violet emission ranges to understand their solar energy harvesting potential (Ranjitha et al., 2013b). It has been noticed that the presence of structural imperfection and defects within TiO_2 is responsible for deteriorating the process of exciton related recombination. Therefore, there is a necessity to produce improved quality films to construct highly efficient photo electric conversion device. To obtain high quality TiO_2 thin films in terms of optical and electrical properties, it is essential to identify an appropriate fabrication method for the film deposition. In the past, TiO_2 thin films depositions could be achieved by the application of diverse techniques such as, molecular beam epitaxy (Fisher et al., 2006), chemical vapour deposition (Sun et al., 2008), chemical bath method (Kite et al., 2018b)(Dussan et al., 2017b), aerosol pyrolysis (Okuya et al., 1999)(Abou-Helal & Seeber, 2002), hydrothermal technique (Manisha et al., 2021b), electrodeposition or electrochemical anodizing (Chigane et al., 2017)(Quiroz & Dussan, 2016b)(Sivaprakash & Narayanan, 2020), and sol–gel method (Pomoni et al., 2005)(Sen et al., 2005)(Arıer & Tepehan, 2011b)(Duan et al., 2016)(Zhao & Lu, 2017)(Liu et al., 2011). With regard to these techniques, the sol-gel method with dip coating technique and electrodeposition or electrochemical anodizing technique both use a low temperature and non-vacuum technology to synthesise the films. The differences between the two techniques, despite the fact that they both operate at low temperatures and non-vacuum conditions, are as follows: (i) the electrodeposition or electrochemical anodizing technique requires two electrodes (the substrate serves as the anode and a second electrode serves as the cathode), while the sol gel method with dip coating technique does not; (ii) while covering a substrate of wide area, the process takes a lot of time. Consequently, the most widely used method is the sol gel method with dip coating technique since it is a simpler procedure. Additionally, the sol gel process has many benefits, including adaptable microstructure, simplicity in compositional changes and

functionalization, remarkable control over precursor solution stoichiometry, need for very low annealing temperatures, and the ability to cover a large area substrate.

Unlike any other previously performed sol-gel method, we have managed to achieve dopant free low band gap, homogeneous and uniform nanocrystalline TiO_2 thin films with band gap reaching up to 2.68 eV and of entirely anatase phase produced with a new technique called as Sol-Gel employing spin coating technology. This approach is having significantly higher advantages over other deposition processes namely, CVD and sputtering deposition, since it requires less budget, has fewer steps, and operates at ambient temperature and air pressure. Following that, the samples were annealed at temperatures ranging from 400 °C to 550 °C and the impacts on its structure, as well as its optical characteristics and surface morphology, were thoroughly investigated and same has been presented in this work.

The experimental studies involved during the fabrication of nanocrystalline TiO_2 thin film are described in this chapter. The fabrication of TiO_2 thin films are achieved using a method so called "sol gel spin coating method". Moreover, a detailed accounts has been presented to the changes occur in its phases, structure, optical properties and surface morphology, as a result of annealing.

4.2 Experimental Approaches

In order to successfully achieve the objective of the experiment which is the fabrication of TiO_2 thin films using a method called "sol gel spin coating method", a thorough planning were worked out in terms of obtaining the materials, preparation of Sol-Gel solution and conducting the actual fabrication of TiO_2 thin films.

4.2.1 Materials

Sourcing the right material is the most significant part of this experiment as the desired result of this experiment is depended on it. So, it is very important to procure an analytical grade material. All chemicals used in this experiment were of analytical grade and were procured from Sigma Aldrich.

4.2.2 Preparation of Sol-Gel Solution

For preparing sol-gel solution, 12 ml of isopropyl alcohol was taken in a vial and 854 µl of titanium tetra isopropoxide was added to it drop by drop and kept stirring on a magnetic

stirrer at room temperature for 1 hour to dissolve it. Following which, few drops of hydrochloric acid (HCl) were added until the solution becomes transparent and stirred for 3 hours at room temperature. The final sol-gel solution was obtained after aging the solution for 24 hours and then filtering out using Nylon syringe filter of 0.22 μm pore size.

4.2.3 Fabrication Process of Nanocrystalline TiO_2 Thin Films

To prepare various samples for this experiment, the widely available Fluorine Tin Oxide (FTO) coated glass slides were used as substrates. After having obtained sol-gel in the above step which is prime solution required during the fabrication of TiO_2 thin films, we then carried out fabrication of TiO_2 thin films on FTO glass substrates each of sample sizes 1cm x 1cm, using spin coating technique and due to this reason, we called this method or technique as "Sol-Gel method employing spin coating technology".

This process involves following steps. Firstly, the substrate was cleaned following the procedure given in Figure. 4.1. The substrate was positioned on the spin coater holder and the filtered sol-gel solution (100μL) was dropped onto the cleaned FTO glass substrates. Subsequently, these substrates were then spin-coated at 4000 rpm for 60 sec, using "SPEKTROSPIN – Spin Coater". During this process, a uniform TiO_2 thin film were evenly distributed and coated on the flat substrates. Thereafter, as-deposited TiO_2 thin film samples were annealed at different temperature ranging between 400 $^{\circ}$C and 550 $^{\circ}$C using the muffle furnace (Tanco, I). Collected samples were then allowed to cool at room temperature for film characterization purpose.

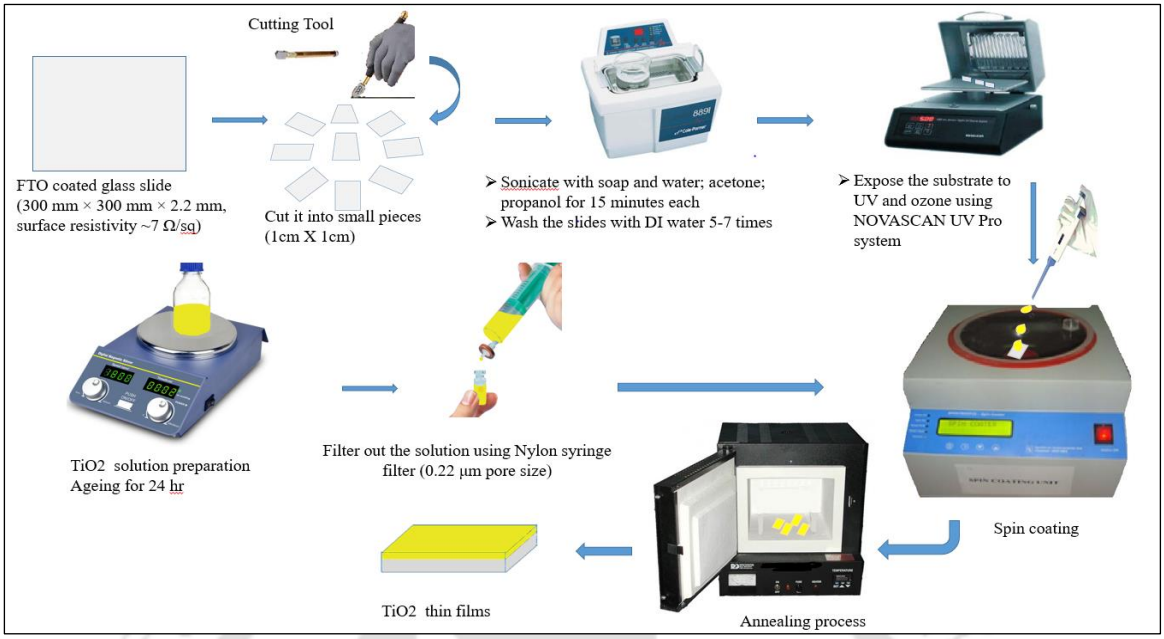

Figure 4.1: Experimental procedure for nanocrystalline TiO_2 thin film deposition by sol – gel method employing spin coating technique.

4.3 Characterization Methods of TiO_2 Thin Films

Freshly formed TiO_2 thin film samples were characterized with the help of XRD measurements at an operating voltage of 45 kV and 200 mA current using a diffractometer "Rigaku SmartLab" with Cu-Kα radiation (λ = 1.54 Å). The films were being scanned in the range from 10° to 70° of 2θ at a scan rate of 5°/min. The results were then analysed using the software known as PDXL, an Integrated X-Ray Diffraction Software. The PDF files used for the analysis of XRD patterns is the ICDD files i.e. International Centre for Diffraction Data. For further confirmation of the phases of the TiO_2, Raman spectroscopy was also taken with the help of a Spectrophotometer of Horiba Jobin Vyon make LabRam HR model excited with an Argon ion laser of 488 nm with 50X zoom with an acquisition time of 10 seconds.

Spectral absorbance measurements were also carried out with a UV-Vis spectrophotometer (Cary 5000 UV-VIS-NIR, Agilent Technologies), at wavelengths ranging between 300 and 800 nm. The film morphology was studied using FESEM of Ziess make Sigma 300 model with a magnification of 200.00 KX zoom. In addition to morphology, the mean roughness and root mean square (RMS) roughness were also computed with the help of AFM device of Oxford make Cypher model using Olympus micro cantilever tip of (resonant frequency 300 kHz, spring constant 26 N/m) and with a sweep area of 5µm × 5µm

area under tapping mode. The thickness of the thin film is measured using Stylus Surface Profilometer of Veeco (Dektak 150).

4.4 Results and Analysis

This section provides detailed accounts of the changes occur in the fabricated TiO_2 thin films in terms of its phases, structure, optical properties and surface morphology, as a result of annealing.

4.4.1 Structural Analysis of Nanocrystalline TiO_2 Thin Film

X-ray diffraction pattern was recorded and carefully studied in this experiment to investigate structures of the crystals and corresponding phases of freshly fabricated nanocrystalline TiO_2 thin films annealed at 400 ^oC, 450 ^oC, 500 ^oC and 550 ^oC, immediately after the sample is taken out from the muffle. The observed patterns from the X-ray diffraction of TiO_2 thin films resulted from annealing at various temperatures were presented in Figure. 4.2. By analysing the X-ray diffraction pattern, it was noted that diffraction pattern of TiO_2 thin films annealed at 400 ^oC shown in Figure. 4.2. (black curve), does not display any distinct crests which corresponds to crystalline TiO_2 phases which is a clear indication that the films are of non-crystalline in nature (i.e, amorphous). However, FTO peaks can still be observed for the FTO coated glass substrate. Whereas those annealed above 400 ^oC i.e. (450 ^oC, 500 ^oC and 550 ^oC) display distinct crests which is the indication of the creation of crystallized nanocrystalline TiO_2 thin films apart from the FTO peaks.

By examining the XRD pattern of the TiO_2 thin film annealed at 450 ^oC for 2 hours shown in Figure. 4.2, it was noticed that the diffraction crests at 25.31^o, 48.1^o, 54.7^o and 61.8^o were indexed in (h k l) planes to (1 0 1), (2 0 0), (1 0 5) and (2 0 4) respectively. The sharp and tall diffraction peak characterizes at 2θ = 25.31^o indicates the manifestation of crystallized TiO_2 thin films and is a distinctive peak of anatase phase (ICDD, PDF Card No.: 00-064-0863 Quality: S). Similarly, the X-ray diffraction patterns of the TiO_2 thin films annealed at higher temperatures such as 500 ^oC and 550 ^oC are shown in Figure 4.2, respectively. There is significant resemblance in their XRD patterns which revealed that all the three samples are of analogous material. Further investigation in the diffractogram, it was also revealed that there is no sign of crests which correspond to the rutile phase of TiO_2 and hence, this clearly confirms that the film formed in this process corresponds to anatase only

and does not contain any rutile phase of TiO_2. The film thickness value is measured using a stylus profilometer and it is found to be approximately 1 μm. Figure. 4.6 shows the 2D profilometer image showing the thin film surface thickness.

Moreover, in order to further investigate the crystallinity (anatase phase) of freshly fabricated TiO_2 thin films, we determined d-spacing (the interplanar spacing between atoms). So, the d-spacing of the freshly fabricated nanocrystalline TiO_2 thin films annealed at different temperature is calculated using Bragg's law equation

$$n\lambda = 2d \sin\theta \tag{4.1}$$

The observed d values of the freshly formed nanocrystalline TiO_2 thin films were compared with the standard d values of tetragonal anatase phase (ICDD, International Centre for Diffraction Data, PDF Card No.: 00-064-0863 Quality: S) assigned for the anatase TiO_2 and they were in good agreement.

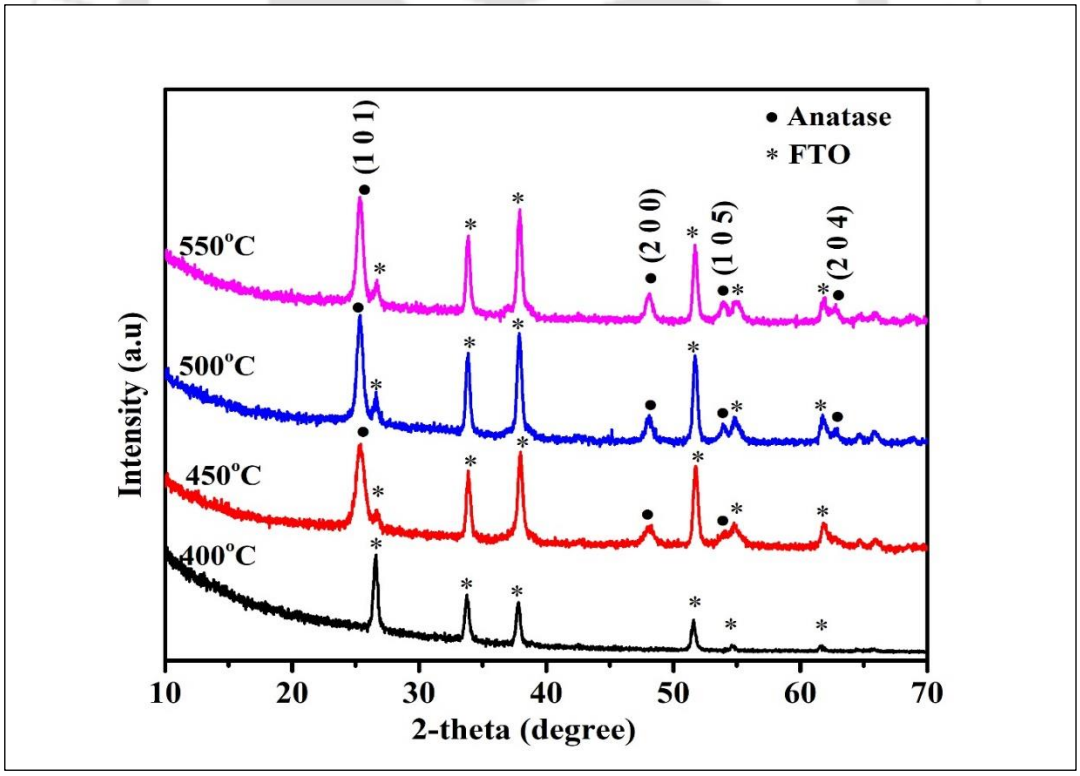

Figure 4.2: XRD patterns of nanocrystalline TiO_2 thin films annealed at 400 °C (black), 450 °C (red), 500 °C (blue) and 550 °C (pink) on FTO coated glass substrate.

Also, in order to determine geometric structure of the nanocrystalline TiO_2 thin films, the lattice constants (a, c) and the unit cell volume are obtained from d-spacing (interplanar spacing) of different (h k l) planes by using the following equations respectively

$$\frac{1}{d^2} = \frac{h^2+k^2}{a^2} + \frac{l^2}{c^2} \quad \text{(For lattice constants)} \tag{4.2}$$

$$Unit\ cell\ volume = a^2c \tag{4.3}$$

So, the lattice constants and the unit cell volume attained from TiO_2 thin films annealed at 450 ^oC are:

a = b = 3.7769 Å,

c = 9.6050 Å and

unit cell volume = 137.01 $Å^3$

These results are also in good alignment with the ICDD, International Centre for Diffraction Data (PDF Card No.: 00-064-0863 Quality: S) assigned for the anatase TiO_2. The lattice constants and unit cell volume along with the microstructural properties of TiO_2 thin films annealed at 450 ^oC, 500 ^oC and 550 ^oC are summarized in Table 4.1.

Furthermore, we then determine the crystallite size of TiO_2 thin films from the integral width of the main peak which is (1 0 1) plane using the well-known Debye-Scherrer's formula (Scherrer, 1918a):

$$D = \frac{k\lambda}{\beta\cos\theta} \tag{4.4}$$

Where;

k = 0.94,

λ = 1.5407Å,

β = Full Width Half Maximum (FWHM)

θ = Diffracting angle.

From these results, it was noticed that the crystallite size increases as annealed temperature increases although the difference is not much of a significant value when the temperature increases from 500 °C to 550 °C (Figure 4.3).

Newly formed TiO_2 thin films are accompanied with some strains and the cause of this strain is associated to lattice misfit which in turn depends upon the deposition condition. The equation used to determine the microstrain of the spin coated TiO_2 thin film is (Chenaina et al., 2021a) :

$$\mu = \frac{\beta}{4\tan\theta} \tag{4.5}$$

Where;

$'\beta'$ is the full width half wave maximum of the (1 0 1) peak, and

'θ' is the Bragg angle.

The mis-match or imperfection within the lattice of the crystal resulted into the formation of dislocations. A dislocation is an imperfection in a crystal. In fact, dislocation arises during the development of TiO_2 thin films is a matter of great importance and it is determined in term of dislocation density.

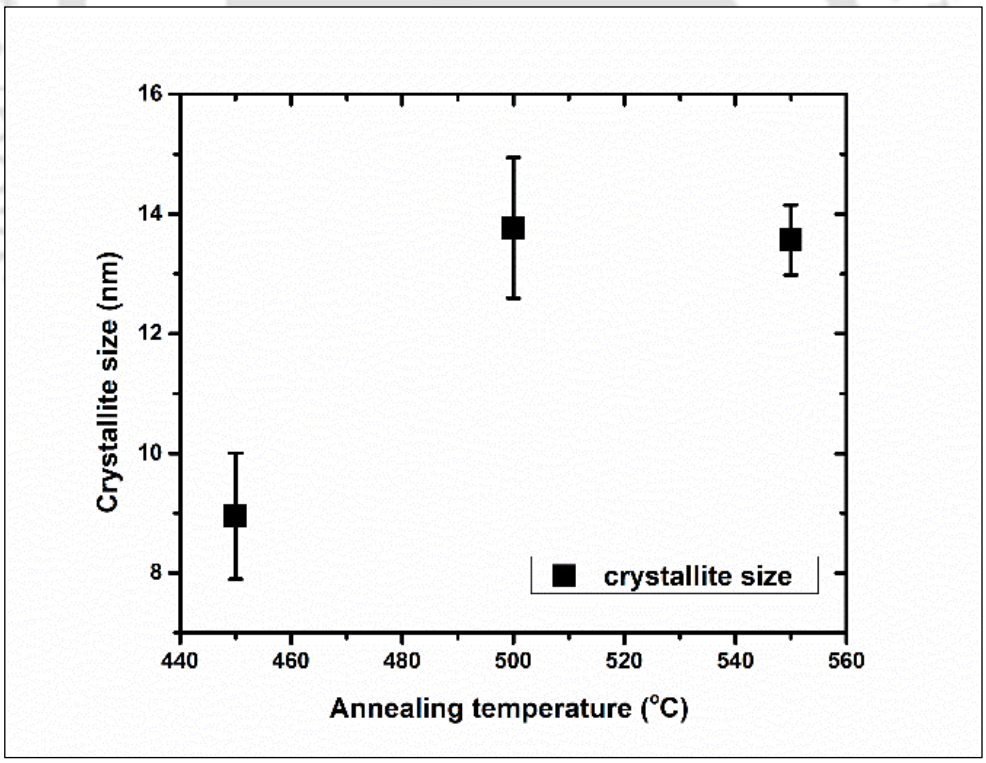

Figure 4.3: Effect of annealing temperature on the crystallite size of TiO_2 thin films annealed at 450 °C, 500 °C and 550°C.

The dislocation density is the length of dislocation lines per unit volume of the crystal. The equation used to determine dislocation density values 'δ' is as follows (Kite et al., 2018b) (Gapale et al., 2018a)

$$\delta = \frac{n}{D^2} \tag{4.6}$$

Where;

$'n'$ is the factor which is equal to unity for minimum dislocation density, and 'D' is the crystallite size in 'nm'.

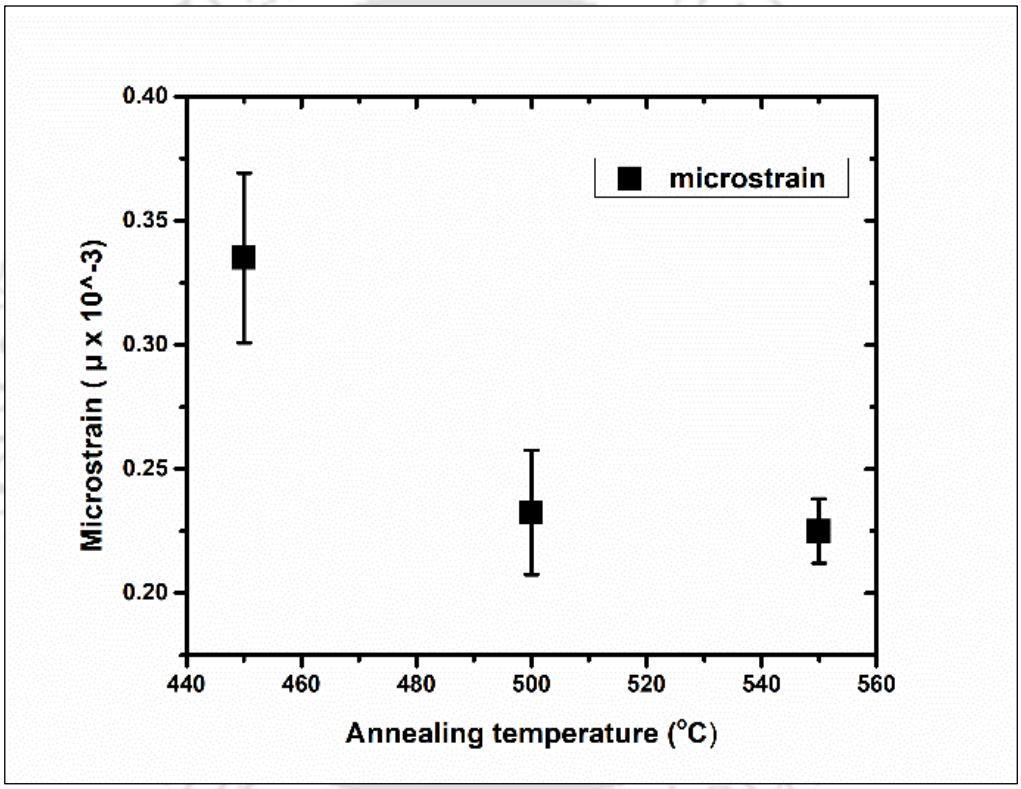

Figure 4.4: Effect of annealing temperature on the microstrain of TiO_2 thin films annealed at 450°C, 500°C and 550°C.

In general, at low annealing temperature, atoms have very low surface mobility due to possession of less energy, which resulted into formation of defects in the films. Whereas, at higher annealing temperature, atoms possess sufficient kinetic energy and high surface mobility allowing to dwell in stable positions inside the crystals. This resulted into a low lattice imperfection in the TiO_2 thin films. Therefore, with increasing annealing temperature facilitated in the formation of improved quality crystallite size and reduced dislocation

density of TiO_2 thin films (Karunagaran et al., 2002). So, relation between dislocation density of the TiO_2 thin films under the influence of annealing temperature is shown in Figure 4.5.

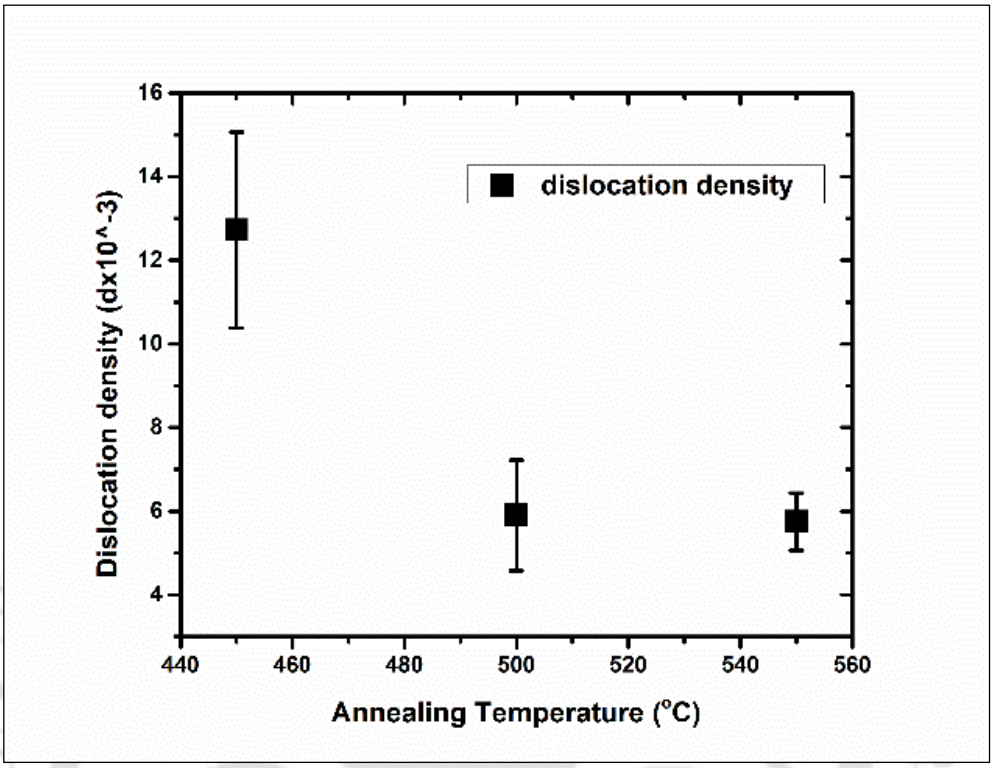

Figure 4.5: Effect of annealing temperature on the dislocation density of TiO_2 thin films annealed at 450 °C, 500 °C and 550 °C.

The key observations made from the analysis of results collected during this micro-structural analysis are crystallite size increases as the annealing temperature increases (Figure. 4.3). And both the microstrain and dislocation density decreases as the annealing temperature increases which also imply that strain and lattice defect decreases as the crystallite size increases (Figure. 4.4 and 4.5).

The lattice constants and unit cell volume along with the microstructural properties such as crystallite size, microstrain and dislocation density of TiO_2 thin films annealed at 450, 500 and 550 ^oC are summarized in Table 4.1.

Table 4.1: Microstructural properties of the nanocrystalline TiO_2 thin films annealed at various temperature.

		Units	**Annealed at 450°C**	**Annealed at 500°C**	**Annealed at 550°C**
Lattice constant	a = b c	(Å)	3.7769 9.6050	3.7814 9.5342	3.7839 9.4614
Unit Cell Volume	a^2c	($Å^3$)	137.01	136.33	135.47
Crystallite Size (D)	Scherrer's Formula	(nm)	8.95	13.77	13.57
Edge Dislocation Density (δ)	$\frac{n}{D^2}$	line/m^2	12.75×10^{15}	6.0×10^{15}	6.0×10^{15}
Microstrain (μ)	$\frac{\beta}{4\ tan\theta}$		0.33×10^{-3}	0.23×10^{-3}	0.23×10^{-3}

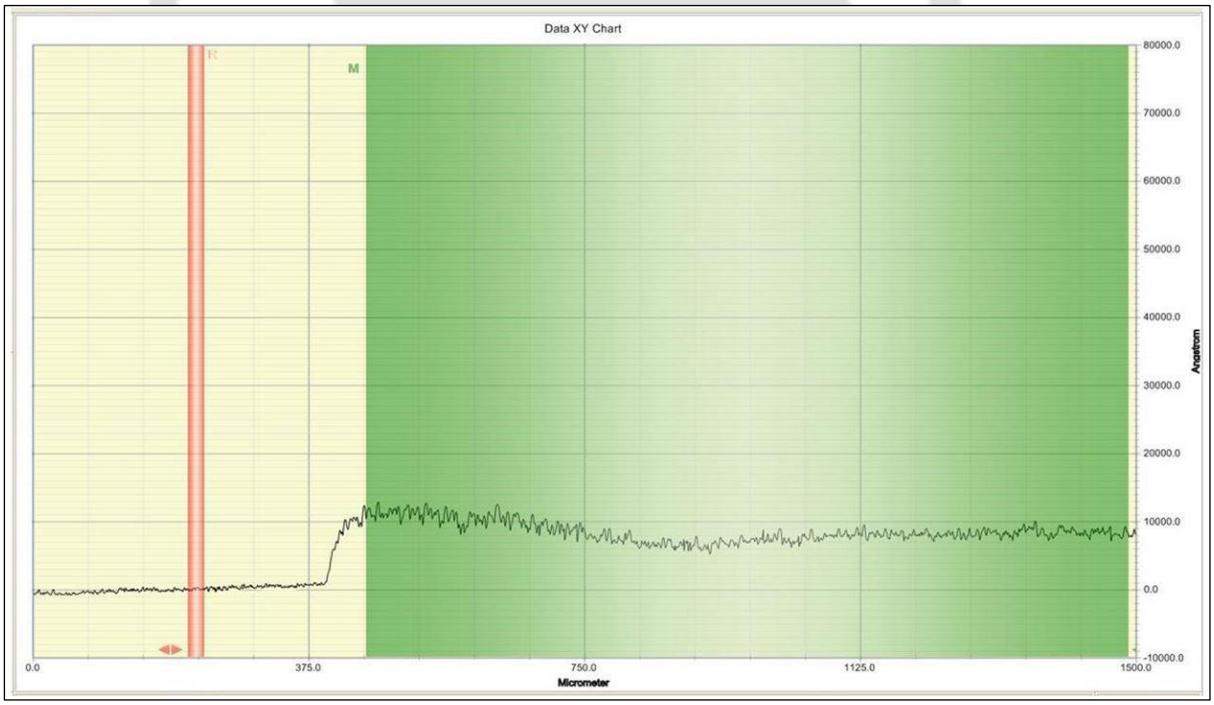

Figure 4.6: 2D Profilometer image showing nanocrystalline TiO_2 thin film thickness.

4.4.2 Raman Analysis of Nanocrystalline TiO_2 Thin Film

In order to confirm the conclusion drawn from the X-ray diffraction method, the same samples were also analysed using Raman spectroscopy. Rutile and anatase phase of TiO_2 crystalline phase exhibits a distinct peak and Raman spectroscopy (Yakovlev et al., 2000) is capable of revealing that titania structural complexity and hence they are easily distinguishable.

Following which Figure 4.7 displays the Raman spectra shifts of the freshly formed TiO_2 thin films annealed at 450 ^oC, 500 ^oC and 550 ^oC. From the Raman spectra shifts, several distinct peaks are clearly visible which is the indication of crystalline anatase phase and the non-appearance of overlying peaks further confirmed that films were crystallized with less imperfection.

There are six Raman active modes corresponding to anatase TiO_2 such as $A_{1g} + 2B_{1g} + 3E_g$. It was also learned that Ohsaka (Ohsaka et al., 1978) have reported the following allowed bands for anatase TiO_2 single crystal: i.e., 512 ± 1 cm^{-1} for A_{1g}, 519 cm^{-1} and 393 ± 2 cm^{-1} for $2B_{1g}$, 142 ± 2 cm^{-1}, 194 ± 3 cm^{-1}, and 634 ± 2 cm^{-1} for $3E_g$ respectively.

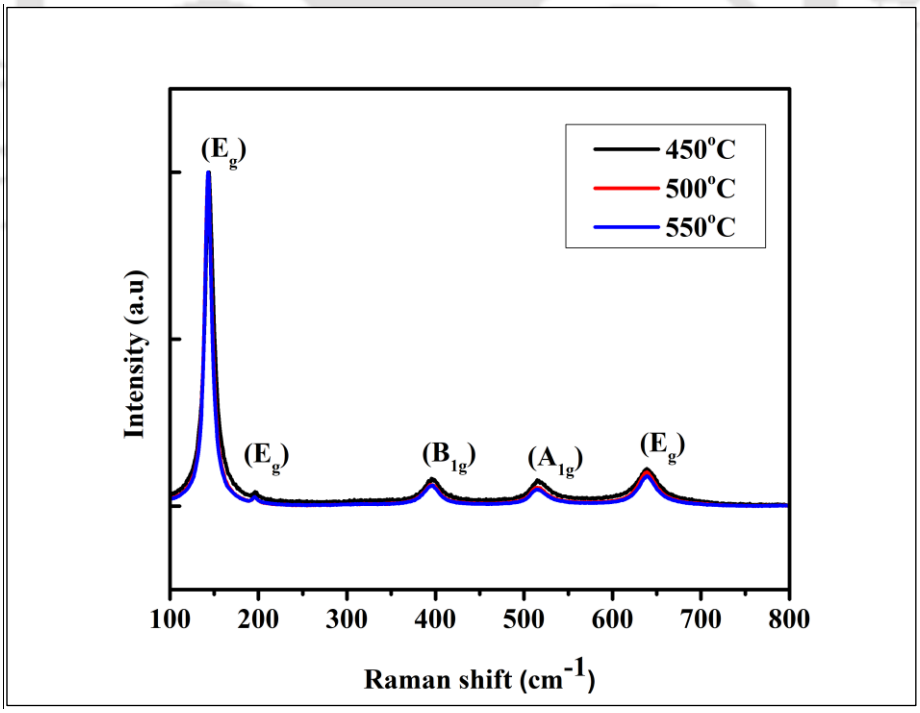

Figure 4.7: Raman spectra of the spin coated nanocrystalline TiO_2 annealed at different annealing temperature.

Therefore, the above-given allowed bands of anatase can then be allocated to the five different distinct peaks (Figure 4.7) noticed by examining Raman spectra shifts of newly formed TiO_2 thin films. As a result, it was observed that the measured peaks at 450 ^oC had bands that are centred at 144.1 cm^{-1} (E_g), 196.8 cm^{-1} (E_g), 397.2 cm^{-1} (B_{1g}), 514.9 cm^{-1} (A_{1g}), and 638 cm^{-1} (E_g), similarly for 500 ^oC; 142.9 cm^{-1} (E_g), 195.6 cm^{-1} (E_g), 395.4 cm^{-1} (B_{1g}), 514.9 cm^{-1} (A_{1g}), and 638 cm^{-1} (E_g) and for 550 ^oC peaks are at 142.9 cm^{-1} (E_g), 195.6 cm^{-1} (E_g), 396 cm^{-1} (B_{1g}), 514.9 cm^{-1} (A_{1g}), and 638 cm^{-1} (E_g) respectively. The above mentioned five distinct peaks were further elaborated individually in the Figure. 8 and by analysing these individual peaks, we then noticed that the peak intensity of the nanocrystalline TiO_2 annealed at 450 ^oC is lower than the other remaining two samples. This shows that there is inhomogeneous crystallization of the films at lower annealing temperature which supports the observation of the XRD analysis.

During the investigation, rutile phase peaks was not noticed which confirms that films formed in this process correspond to anatase only and does not contain any rutile phase of TiO_2. Therefore, it is evident that the result of X-ray diffraction analysis is further proven by the Raman spectra analysis method.

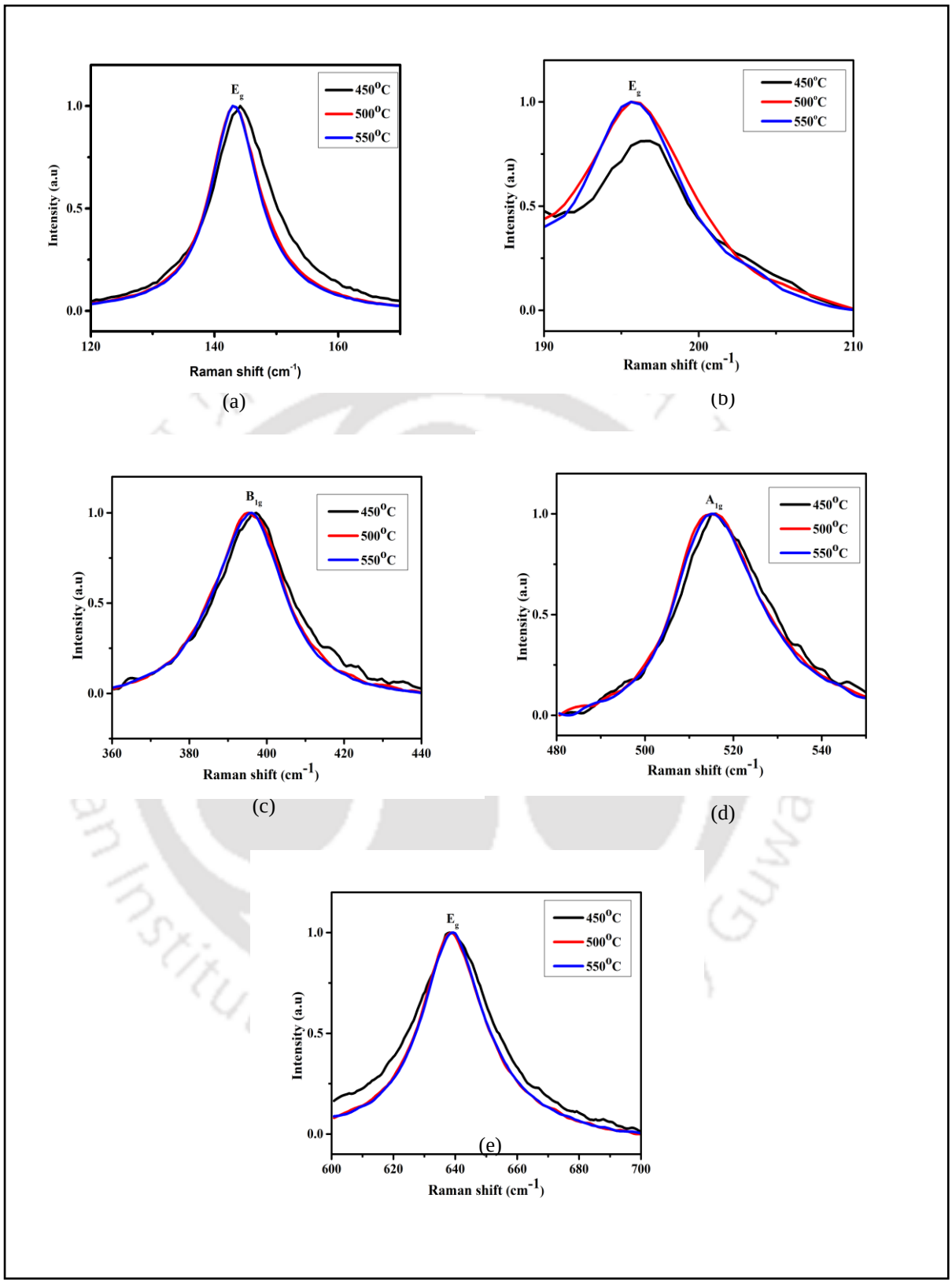

Figure 4.8: (a-e). Enlarge view of the five Raman peaks of the spin coated nanocrystalline TiO_2 annealed at different temperature.

4.4.3 Optical Properties and Band Gap Analysis of Nanocrystalline TiO_2 Thin Film

In order to investigate optical properties of the newly fabricated nanocrystalline TiO_2 thin films, UV-visible transmittance and absorbance spectra of TiO_2 thin film samples were analysed as can be seen in Figures 4.9 and 4.10.

From spectral transmittance measurements in Figure. 9, we can broadly classify the spectra in two distinct regions characterized as first region of highly transparent (≥ 80%) and second region of strong absorptions categorized by a sharp reduction in optical transmission. This sharp reduction in optical transmission is as a result of transition of electrons in between valence and conduction bands of the semiconductor materials (Kite et al., 2018b).

From this spectral transmittance, it is also observed that the transmittance value also reaches 80% and beyond for wavelengths values ranging from 450 nm and above. With increasing annealing temperature, the transmittance value decreases. This decrease is due to increases in the crystallite size and particles agglomeration thereby increases the diffusion of light which in turn decreases the transmittance (Wang et al., 2013)(Vishwas et al., 2012b).

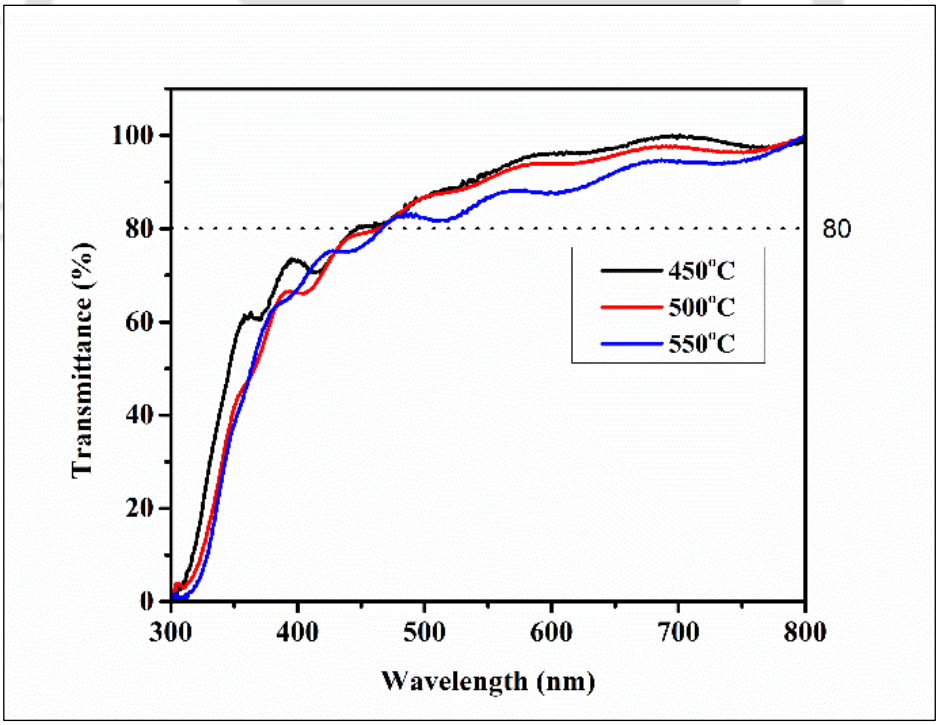

Figure 4.9: Spectral transmittance measurements as a function of wavelengths for different annealing temperature.

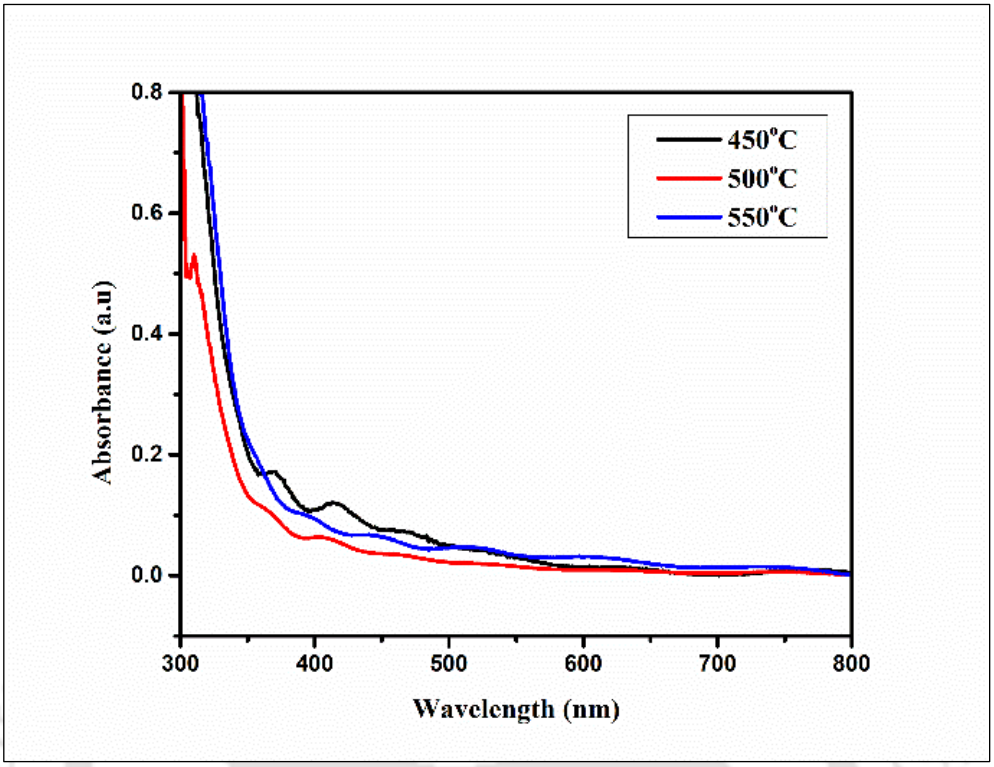

Figure 4.10: Spectral absorbance measurements as a function of wavelengths for different annealing temperature.

From the spectral absorbance measurements in Figure 4.10 and using Beer's law (Fox, 2001), the absorption coefficient, α of the films was calculated. The optical band gap energy (E_g) was estimated using Tauc's model (Bensouici et al., 2017).

$$\alpha h\nu = A(h\nu - E_g)^n \quad (4.7)$$

Where;

E_g is the separation gap between bottom of conduction band and top of the valence band.

$h\nu$ is the photon energy and,

n is a constant, which depends on the probability of transition and its values are 1/2, 3/2, 2, and 3 for direct allowed, direct forbidden, indirect allowed and indirect forbidden transitions respectively.

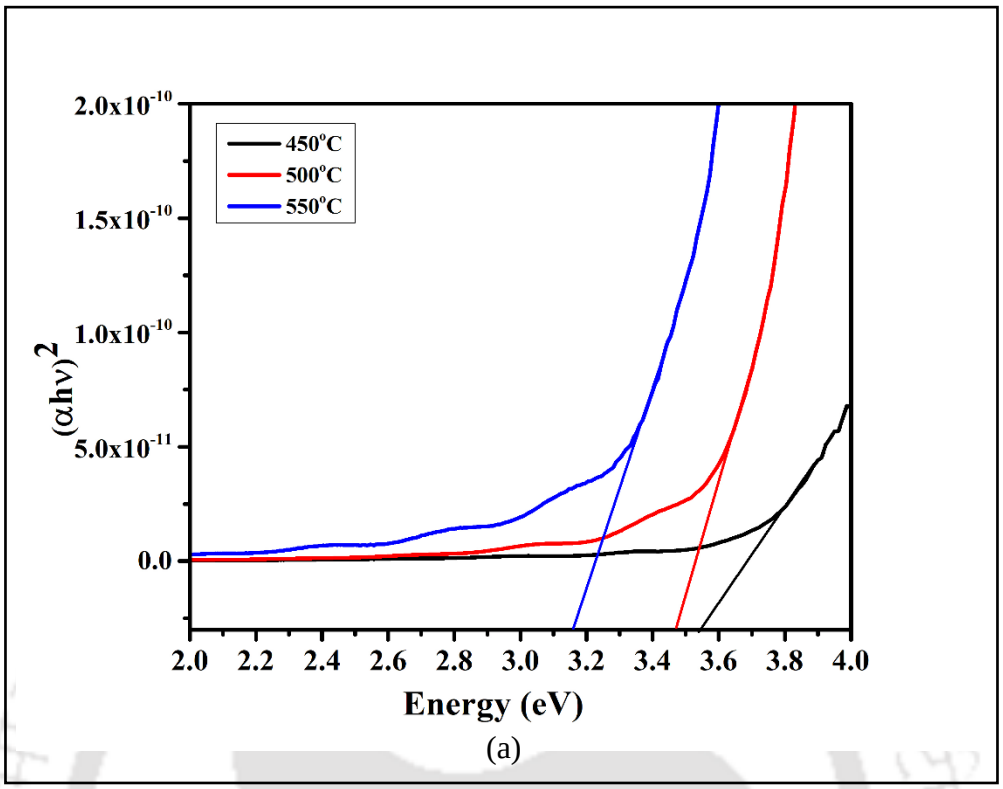

(a)

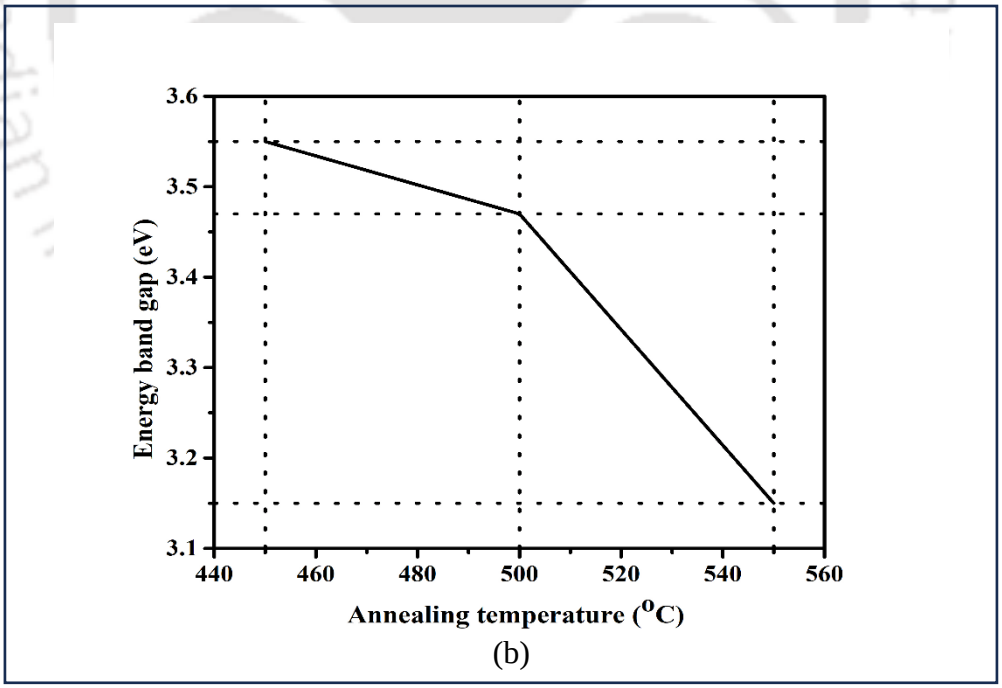

(b)

Figure 4.11(a) $(\alpha h\nu)^2$ Vs photon energy for direct band gap and (b) direct band gap vs. annealing temperature (inset) of the TiO_2 thin films annealed at different temperature.

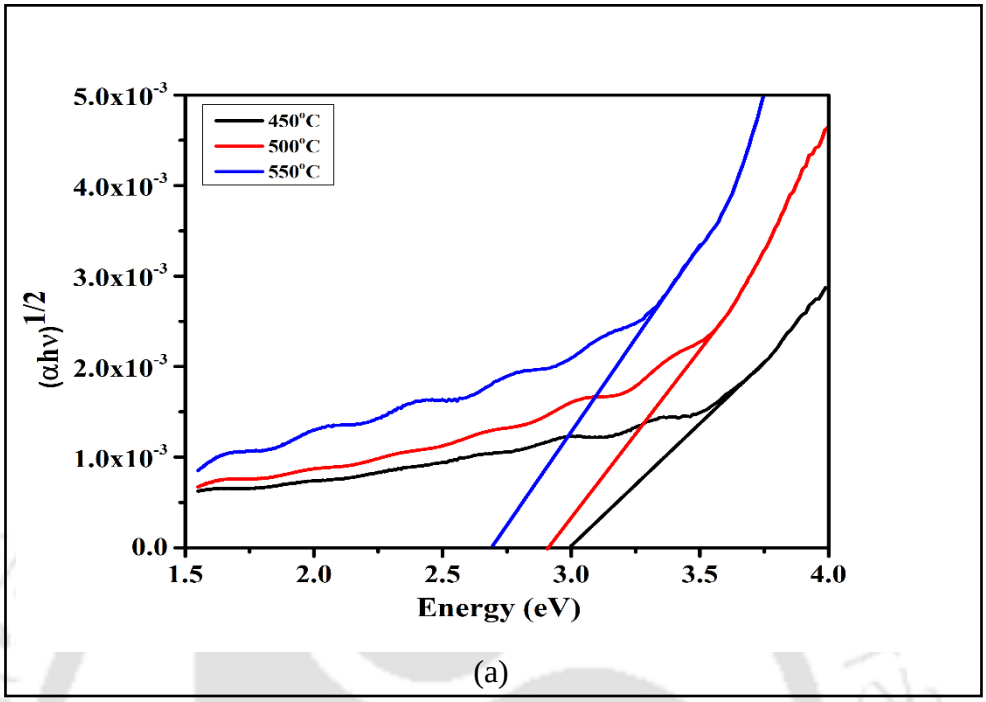

(a)

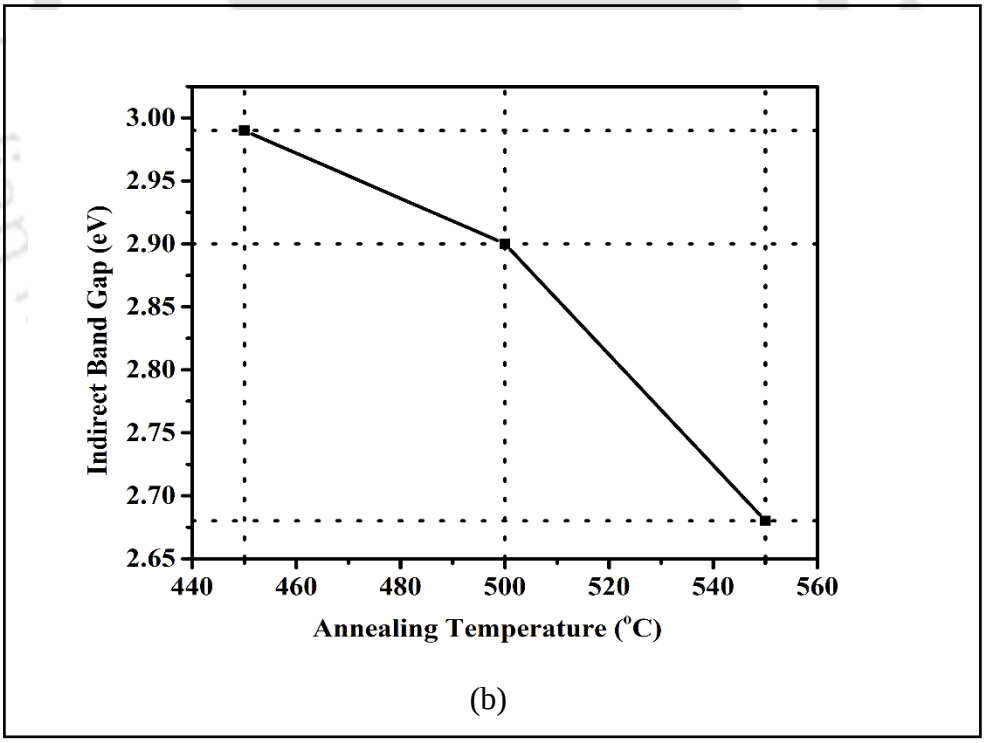

(b)

Figure 4.12: (a) $(\alpha h\nu)^{1/2}$ vs photon energy for indirect band gap and (b) indirect band gap vs. annealing temperature (inset) of the TiO_2 thin films annealed at different temperature.

Figure 4.11 and 4.12 displays the optical direct and indirect band gap. It was estimated by extrapolating the linear portion of $(\alpha h\nu)^2$ vs photon energy curve and $(\alpha h\nu)^{1/2}$ vs photon energy curve to the photon energy axis respectively. The values of the direct band gap at the annealing temperatures 450 ^oC, 500 ^oC, 550 ^oC are 3.55 eV (349 nm), 3.47 eV (357 nm), 3.15 eV (394 nm) respectively whereas indirect band gap values for the same temperature ranges are 2.99 eV (415 nm), 2.90 eV (428 nm), 2.68 eV (463 nm) respectively. From this analysis, it was determined that the energy gap reduces with the increase in annealing temperature. This narrowed band gap enables visible light absorption and thus promotes solar photon energy conversion. This decrease in the band gap is due to the structural changes of the nanocrystalline TiO_2 thin films resulted from the annealing(X. Wang et al., 2013). Annealing results in grain growth thereby increasing the packing density of the thin films. This increase in packing density increases the interfacial Ti-Ti electronic bonding, which is the main reason of band-gap narrowing (Ranjitha et al., 2013b)(Wang et al., 2015b). The narrowed band gap of the newly formed TiO_2 can utilize a larger fraction of solar energy, and the light absorption can be extended to visible region (about 40% of solar spectrum) making it more efficient for solar energy conversion.

4.4.4 Surface Morphology and Microstructural Analysis of Nanocrystalline TiO_2 Thin Film

We also analysed the samples using 2D & 3D images taken from AFM device to investigate topography of TiO_2 thin films coated over FTO glass substrates. The sample scan area is of 5μm × 5μm. During the analysis, as is observed in Figure. 4.13, it was noticed that the surface of the film has different morphology and the grain sizes for different annealing temperature. In addition, there is no sign of any cracks. So, we do confirm that the whole morphology of the deposited films is compact in nature.

Below (Figure 4.13) displayed topographic images show considerable surface roughness due to agglomerated grains on the surface of the TiO_2 thin film samples. During thorough analysis, it was noticed that surface roughness is found to be higher with those samples annealed at higher temperatures which is resulted from the crystallite size and inter particle fusion of particles.

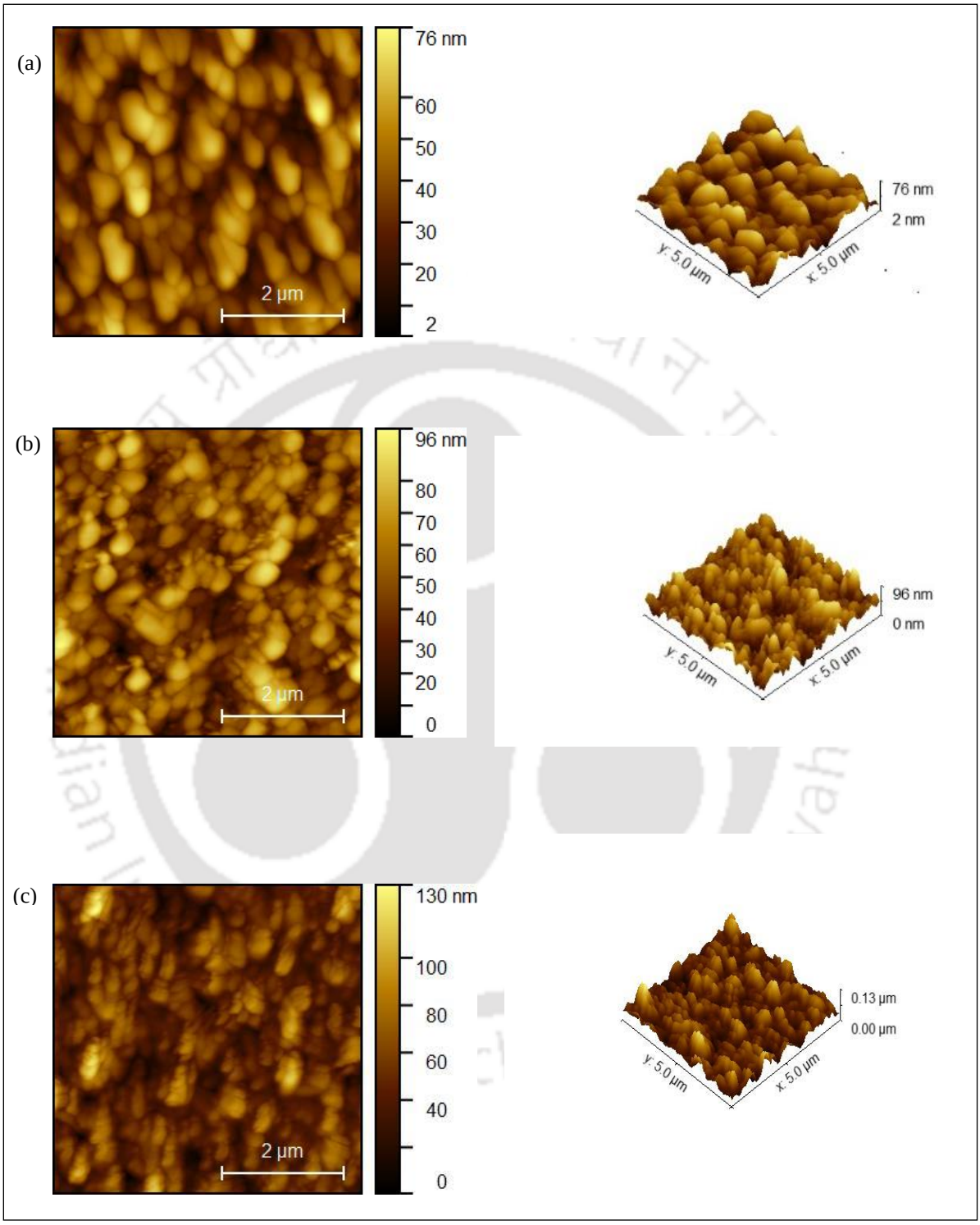

Figure 4.13: 2D (Left) and 3D (Right) images of TiO_2 thin film annealed at (a) 450°C (b) 500°C and (c) 550°C.

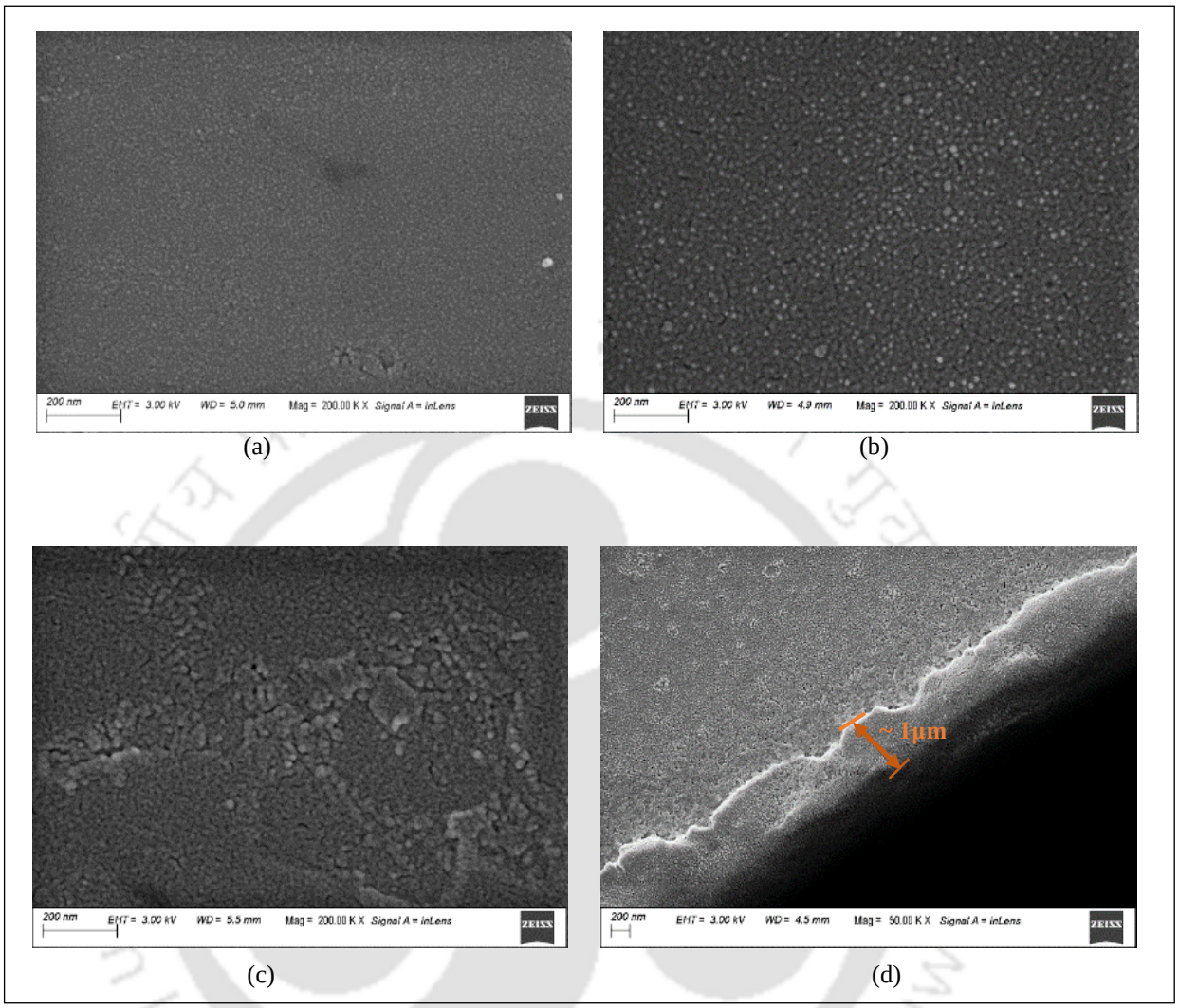

Figure 4.14: Top view of FESEM image of spin coated nanocrystalline TiO_2 thin films annealed at (a) 450°C (b) 500°C and (c) 550°C; (d) cross section view of the film annealed at 550°C

Additonally, to obtain better morphological details visually, magnified images with a magnification of 200.00 KX using FESEM were also taken for the spin coated nanocrystalline TiO_2 thin film annealed at 450 °C, 500 °C and 550 °C (Figure 4.14).

By analysing these images, we then confirm that the grain size increases and the grains are homogeneous and uniformly distributed but we can observed few agglomerated grains as the annealing temperature reaches 550°C. Further analysis of the FESEM images taken by positioning from the top of TiO_2 thin film samples annealed at 450 °C, 500 °C and 550 °C, also visually confirms well connected nanograins and the films are compact as shown

in Figure. 4.14 (a), (b) and (c). Whereas, by studying magnified FESEM image with magnification of 50.00 KX taken from the cross section of TiO_2 thin film samples annealed at 550 ^oC as shown in Figure. 4.14(d), we then confirm that a well coated nanocrystalline TiO_2 thin films are formed on the FTO glass substrate. We also measured the thickness of the coated TiO_2 thin films which is aproximately 1 μm thick which support the film thickness data measured from the stylus profilometer.

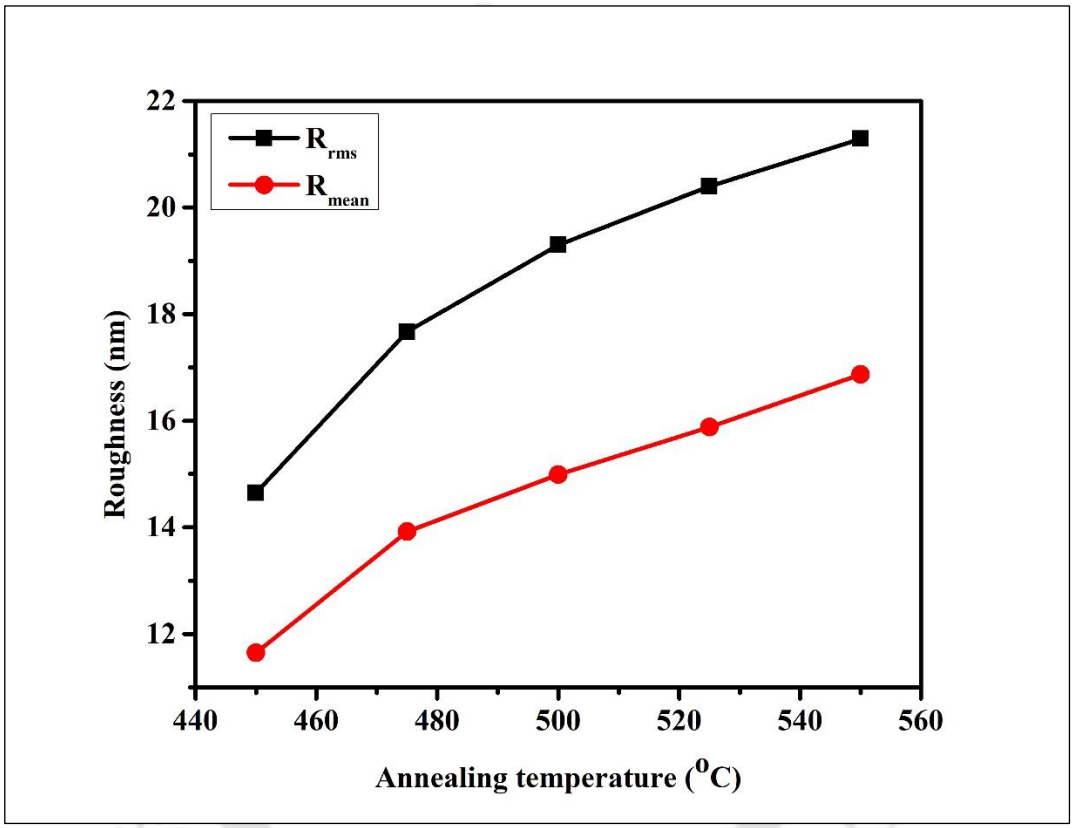

Figure 4.15: Plot of annealing temperature versus roughness of newly fabricated nanocrystalline TiO_2 thin films.

Furthermore, by using two key parameters such as mean roughness (R_{mean}) and root mean square roughness (R_{rms}), surface roughness of the TiO_2 thin film can be described through statistical methods (Trapalis et al., 2009). During the analysis, it was also observed that there is an increasing trend in the values of both R_{mean} and R_{rms} with the increase of annealing temperature from 450^oC to 550 °C (Figure 4.15). Higher annealing temperature lead to increase surface roughness due to several factors like accelerated oxidation and contamination, stress relaxation within the material, phase transformations inducing surface roughening, increased atom mobility promoting grain growth, enhanced surface diffusion

causing atom redistribution and defect formation, and differential thermal expansion resulting in mechanical stresses and surface deformation. Overall, as annealing temperatures increase, these combined effects contribute to increase surface roughness. Along with the surface roughness, fractal dimensions of these films were also studied with the help of AFM images taken in AFM) device. The fractal dimension describes the complexity of nanoparticle arrangement within a film, considering factors like size, shape, and packing. A higher fractal dimension indicates a more complex distribution, often associated with increased surface roughness or porosity. This analysis is crucial for understanding the morphology of thin films, benefiting applications like catalysis, sensing, and thin-film electronics. In order to analyse fractal dimensions of TiO_2 thin films, a method known as Cube counting was used which is based on the linear interpolation and it applies the AFM data (Zahn & Zösch, 1999)(Douketis et al., 1995). The fractal dimensions (D_f) resulting from the AFM images of TiO_2 samples are presented in Figure. 4.16. A lower value of fractal dimension means smoother surfaces whereas a higher value means irregular surfaces (Risović et al., 2008). By studying these results, it was noticed that all samples display a similar pattern and are discretely sensitive to the annealing temperature.

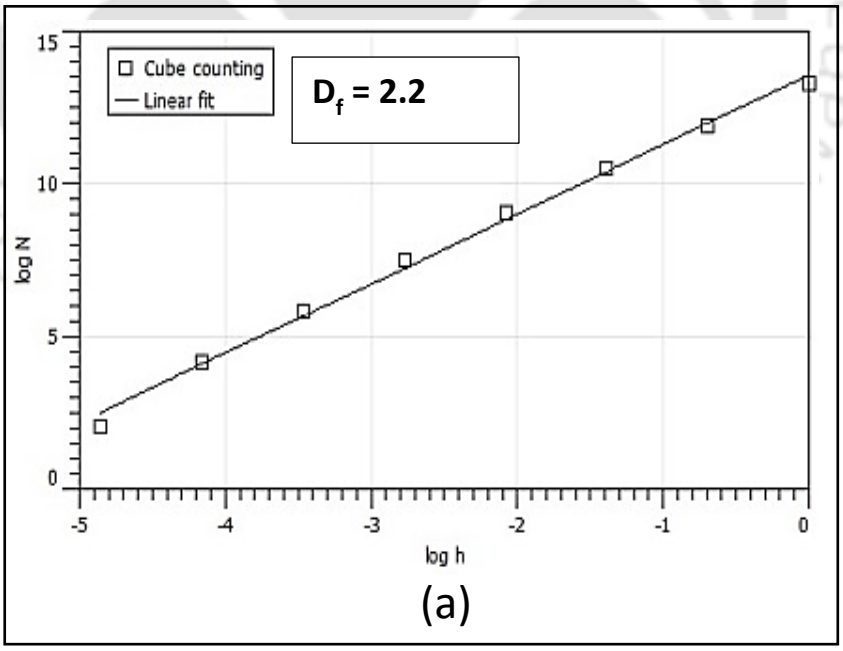

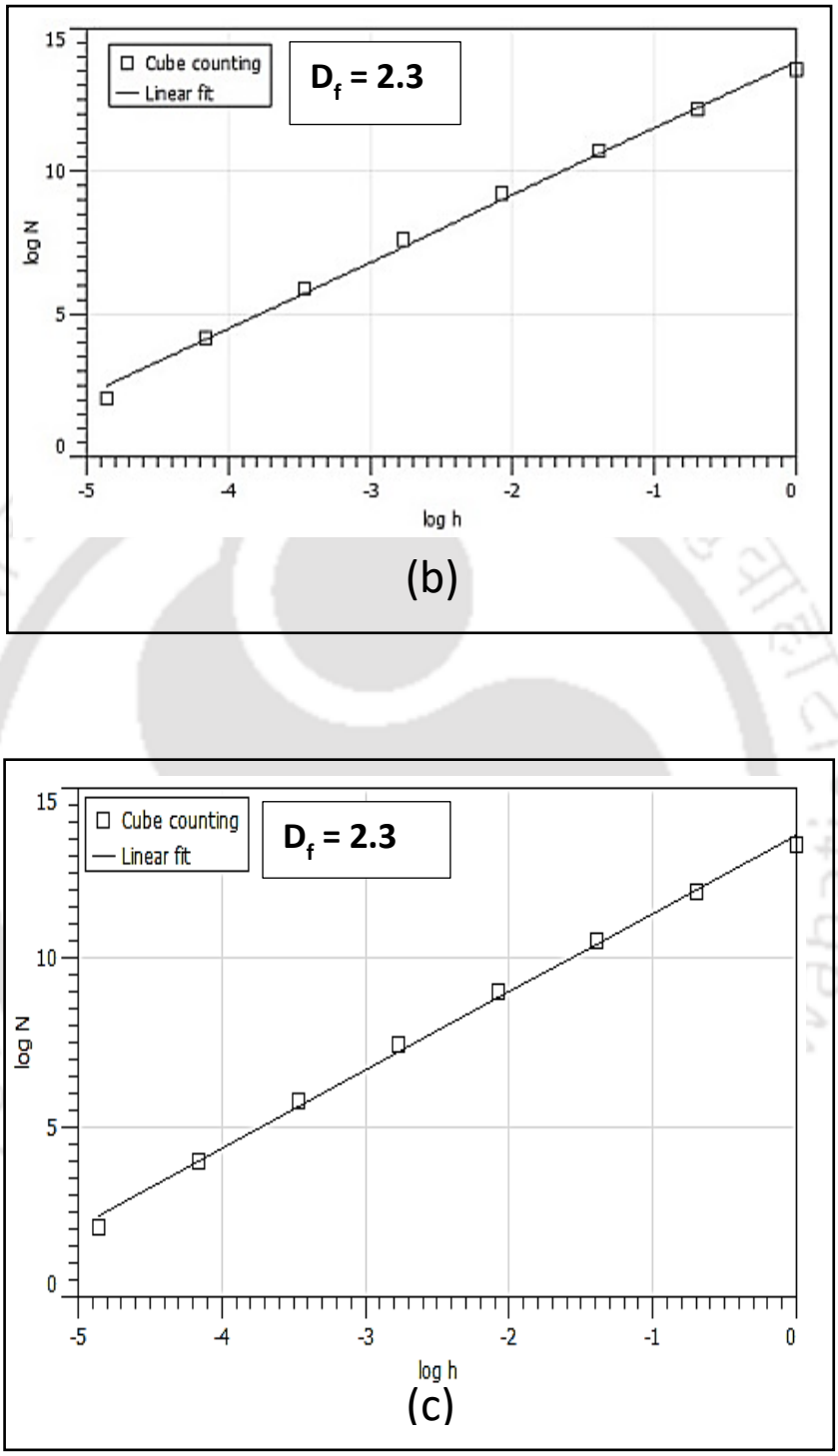

Figure 4.16: Fractal dimension for AFM images of the spin coated TiO_2 thin film (area scan = 5x5 μm) annealed at (a) 450°C (b) 500°C and (c) 550°C.

4.5 Conclusion

In order to create dopant-free, narrow band gap nanocrystalline TiO_2 thin films, a process known as Sol-Gel using spin coating technology is demonstrated in this work. TiO_2 thin films fabricated through this technique are found to be homogeneous and uniform nanocrystalline with band gap reaching up to 2.69 eV and of entirely anatase phase. Purely anatase phase TiO_2 thin film is produced via annealing procedures. It was also identified that all thin films, with the exception of the sample annealed at 400^oC, display the anatase phase by X-ray diffraction analysis and also confirmed through the Raman spectra analysis method. Raman spectra exhibits peaks which correspond to anatase phase only. Structural characterization determines that crystallite size increases as the annealing temperature increases thereby decreasing both the microstrain and dislocation density. FESEM analysis confirms the increase in grain size as the sample submitted to heat. AFM analysis determines that surface roughness is found to be higher with those samples annealed at higher temperatures which is resulted from the inter-particle fusion of particles and increase in grain size. Optical analysis determines that the thin films which are annealed at 450°C and 550°C display a transmittance higher than 80% in the visible region ranging from 450 nm and above. Due to this high transparency in nature, TiO_2 thin films are an interesting candidate for solar energy harvesting devices. The films present a band gap ranging between 2.68 eV to 3.55 eV, this variation is associated with the topography and crystalline structure. Therefore, with all these above findings, the prepared nanocrystalline TiO_2 anatase phase thin film is considered much more suitable for the fabrication of plasmonic photo-electric conversion device which is the next stage of our research.

CHAPTER 5

DESIGN AND DEVELOPMENT OF TiO_2|Ag PLASMONIC SOLAR ENERGY HARVESTING DEVICE

CHAPTER 5

DESIGN AND DEVELOPMENT OF TiO_2|Ag PLASMONIC SOLAR ENERGY HARVESTING DEVICE

5.1 Overview

The arena of photovoltaics, the conversion of sunlight to electricity, is a rapidly emerging technology that can make a significant contribution to cracking the ever-increasing energy demand. However, a new ground-breaking technology which is gaining momentum at present is the ability of metallic nanoparticles for electron generation via trapping light and scattering into the solar cells which is also known as plasmonic effect is being utilized in Plasmonic solar (photovoltaics) cells (Linic et al., 2011a). In fact, this plasmonic effect enhances the performance of solar cell in terms of electron generation and injection, charge separation and reducing recombination. Hence, it is becoming one of the most popular researched photovoltaic systems. However, the challenge is in the existing methods of deposition of metallic nanoparticles which are very complicated (Takahashi & Tatsuma, 2010). The synthesis of the Ag nanoparticles is not an easy and straightforward method. It requires a careful control over the environment and accurate amount of the solution is needed along with various capping agents to stabilize the nanoparticles (Kochuveedu et al., 2013)(Lu et al., 2013). Moreover, fabrication of the device is much more complicated and challenging since specific shapes must be fabricated, such as nanorods (as in the case of photocatalysis) for a desired set of plasmonic modes (Kazuma et al., 2011). Additionally, Ag nanoparticles have to be carefully implanted within the active layers to achieve better performance photocatalytic or photovoltaic characteristics, especially in organic photovoltaics. For implanting Ag nanoparticles within the active layers, specific techniques such as templates, nanolithography, or nanofabrication are employed (Kazuma et al., 2011). These aforementioned fabrication methods are complicated, time consuming, and sometimes they are not even suitable for photovoltaic applications. For this reason, it is essential to discover a new simple, quick and direct method of deposition to form the metallic nanoparticles and in the end, it is also essential to achieve comparatively less expensive plasmonic solar cells. Towards this direction, some reports have suggested some improvement in the photovoltaic performance of dye sensitized solar cells (DSSC), (Yun et al., 2015) quantum dot sensitized

solar cells, (Prasad et al., 2018) and hybrid polymer solar cells (Liu et al., 2014) with the application of the Ag nanoparticles along with TiO_2 as light trapping and light reflecting agents, as well as electron-hole recombination suppressors.

Unlike most of the works in the field of plasmonic solar cell, our work presents the research findings on plasmonic photovoltaics in which plasmonic material such as AgNPs is used as better absorbers for generating and injecting electrons. Further, this work explains the basic operation and enhanced performance of solar cells due to the plasmonic effect of metal nanoparticles in the cells i.e. due to the formation of charge carriers (hot electrons). In addition, a step-by-step process of device making, testing, characterization and in-depth analysis of results are also discussed.

5.2 Experimental Approaches

5.2.1 Materials

FTO coated glass slide, Titanium tetra isopropoxide, Hydrochloric acid (35%), Acetone, Propanol were procured from Sigma Aldrich. Silver wire of 1mm diameter and silver target of 3inch diameter were purchased from Ultrananotech. Nanopure water (Resistivity is 14-15 megohm) (Millipore Co.) was also used. Cleaning of FTO coated glass substrate, fabrication of TiO_2 thin film over the FTO coated glass substrate are already described in Chapter 4.

5.2.2 Deposition of Silver Nanoparticles over TiO_2 Thin Layer

In this step, our main objective is to deposit thin films of Ag nanostructure over the surface of the above synthesized TiO_2 thin film layer. This was achieved through two different techniques known as “DC Magnetron sputtering” and “Thermal Vapour Deposition”. At the end of these both processes, silver nanostructured thin films of 300 nm thickness were found to be deposited over the TiO_2 surface.

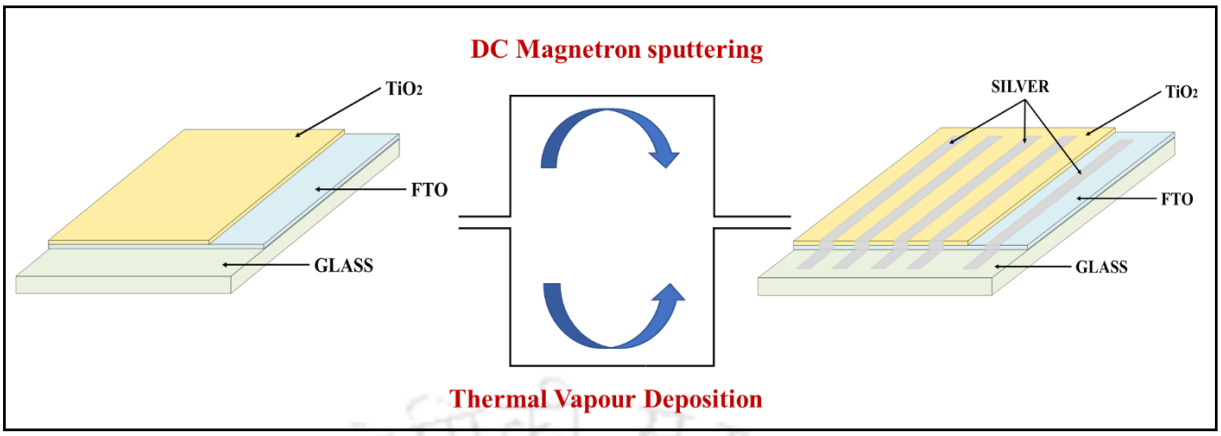

Figure 5.1: Experimental procedure for the Ag thin film deposition over nanocrystalline TiO_2 thin film.

While performing DC Magnetron sputtering technique, the sputtering system is pumped down to a base pressure of 6×10^{-6} mB. The silver was deposited from a 2″ Ag target (99.99%, Ultrananotech Pvt Ltd) under Ar gas at a flow rate of 30 sccm, and the total pressure in the chamber was 3×10^{-2} mB. The target power was kept at 10 W, and the substrate temperature was 25 °C. The substrate was masked using a stencil made of galvanized steel.

While performing the Thermal Vapour Deposition technique, Ag is deposited on the TiO_2 surface from a 1mm diameter Ag wire (99.99%, Ultrananotech Pvt Ltd). Parameters of the instrument were (Current = 33.7 A; Voltage = 2.03 V; Rate of Deposition = 3.3 Å/s; Working Pressure = 5.2×10^{-6}). The substrate was masked using a stencil made of galvanized steel.

5.3 Characterization Techniques

Before proceeding to testing of the fabricated device, it is essential to study the surface morphology, structural analysis and optical properties of the nanomaterials, in order to confirm the integrity of the nanoparticle states of the constituent materials which are TiO_2 and Ag which will be explaining in this section.

5.3.1 Structural Analysis and Surface Morphology of TiO_2 And Ag

XRD measurements of both the films were taken at an operating voltage of 45 kV and 200 mA current using a diffractometer, Rigaku SmartLab with Cu-Kα radiation (λ = 1.54 Å). The films were being scanned in the range from 10° to 70° of 2θ at a scan rate of 5°/min.

The results were then analysed using the software known as PDXL, an Integrated X-Ray Diffraction Software. The PDF files used for the analysis of XRD patterns is the ICDD files i.e. International Centre for Diffraction Data. For further confirmation of the phases of the TiO_2, Raman spectroscopy was also taken with the help of a Spectrophotometer of Horiba Jobin Vyon make LabRam HR model excited with an Argon ion laser of 488 nm with 50X zoom with an acquisition time of 10 seconds. The film morphology of the fabricated device was studied FESEM of Ziess make Sigma 300 model with a magnification of 200.00 KX zoom. In addition to morphology, the mean roughness and root mean square (RMS) roughness were also computed with the help of AFM device of Oxford make Cypher model using Olympus micro cantilever tip of (resonant frequency 300 kHz, spring constant 26 N/m) and with a sweep area of 5μm × 5μm area under tapping mode. The thickness of the thin film is measured using Stylus Surface Profilometer of Veeco (Dektak 150).
The measured results are presented in the section "Result and Discussion".

5.3.2 Optical and Device Characterization

Absorption spectra of the TiO_2 and silver thin film were obtained using a UV-Vis spectrophotometer so-called Cary 5000 UV-VIS-NIR of Agilent Technologies, at wavelengths ranging between 300 and 800 nm. A Keithley 2400 source meter was used to measure the current density−voltage (J−V) characteristic curves in an argon-filled glove box by illuminating the device under a solar simulator (AM 1.5 G, 100 mW cm^{-2}, Oriel Sol 3A solar simulator, Newport). The work function and the ionization energy of the sample were measured under ambient conditions using a scanning Kelvin probe combined with air photo emission system (ASKP150200, KP Technology Ltd.) with a 2 mm diameter stainless-steel tip. The tip was calibrated against a pure gold reference sample with a work function of 5.1 eV.

5.4 Results and Discussion

In this section, an examination of X-ray diffraction pattern recorded during the characterization was carefully executed to inspect crystalline structures and its corresponding phases. The investigation was for both freshly fabricated nanocrystalline TiO_2 thin films that were subjected to 500 ^oC annealed temperature in the muffle furnace and Ag thin film deposited by thermal vapour deposition technique as well as sputtering technique.

While examining aforesaid X-ray diffraction pattern of TiO_2 thin films as illustrated in Figure 5.2(a), several distinct peaks were noted which was the positive sign of formation of crystallized nanocrystalline TiO_2 thin films and it was also noticed that these peaks were different from the FTO peaks. Further, when indexing these diffraction peaks displayed at 25.31°, 48.1°, 54.7° and 61.8° in (h k l) planes, their corresponding value were found out to be (1 0 1), (2 0 0), (1 0 5) and (2 0 4) respectively.

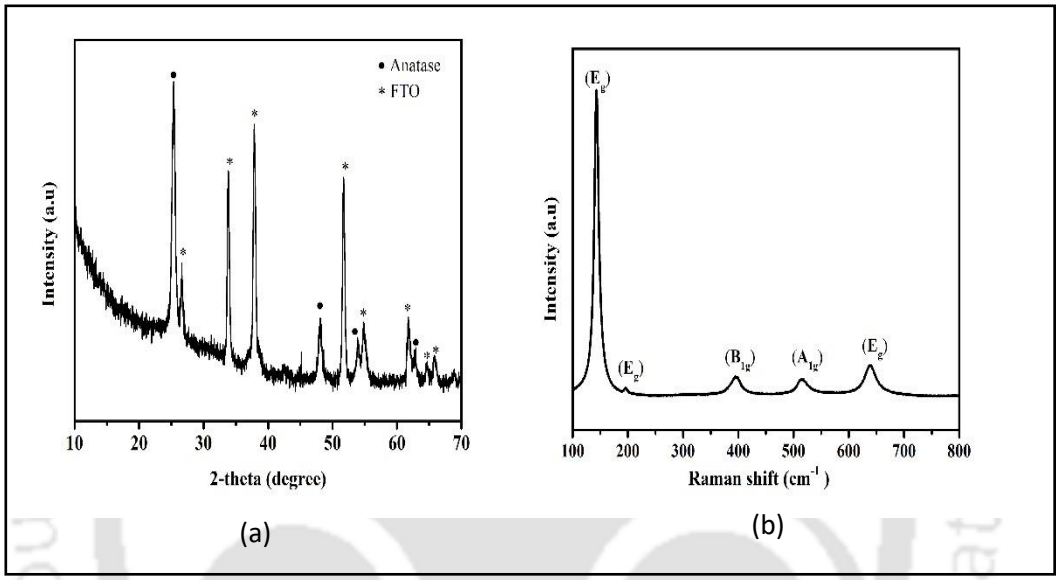

Figure 5.2: (a) XRD spectra of nanocrystalline TiO_2 thin film.
(b) Raman spectra of nanocrystalline TiO_2.

The diffraction peak characterized at $2\theta = 25.31^o$ which was the most pointed and tallest among the rest, was the positive sign of formation of crystallized TiO_2 thin films and this peak also confirmed to be of anatase phase (ICDD, PDF Card No.: 00-064-0863 Quality: S). Besides, absence of any peak that correspond to the rutile phase of TiO_2 was further confirmed though an examination in the diffractogram. It was therefore concluded that the above fabricated TiO_2 thin films were of anatase only.

Furthermore, using Raman spectroscopy the same samples were examined once again, as we learned that Raman spectroscopy (Yakovlev et al., 2000) is capable of revealing the structural complexity of TiO_2. This is due to the fact that rutile and anatase phase of TiO_2 crystalline phase displays individual distinctive peaks and therefore they are easily noticeable. This analysis was performed so that the conclusion obtained from the X-ray

diffraction method could be re-confirmed. There are six Raman active modes corresponding to anatase TiO_2 such as $A_{1g} + 2B_{1g} + 3E_g$. It was also learned that Ohsaka (Ohsaka et al., 1978) have reported the following allowed bands for anatase TiO_2 single crystal: i.e, 512 ± 1 cm^{-1} for A_{1g}, 519 cm^{-1} and 393 ± 2 cm^{-1} for $2B_{1g}$, 142 ± 2 cm^{-1}, 194 ± 3 cm^{-1}, and 634 ± 2 cm^{-1} for $3E_g$ respectively. Therefore, the above-given allowed bands of anatase can then be allocated to the five different distinct peaks Figure 5.2(b) noticed by examining Raman spectra shifts of newly formed TiO_2 thin films. As a result, it was observed that the measured peaks that are centred at 142.9 cm^{-1} (E_g), 195.6 cm^{-1} (E_g), 395.4 cm^{-1} (B_{1g}), 514.9 cm^{-1} (A_{1g}), and 638 cm^{-1} (E_g). From this investigation, there were no peaks that corresponds to rutile phase which therefore re-confirms that the fabricated TiO_2 thin films were of anatase only. Hence, the conclusion drawn from the X-ray diffraction analysis is further reinforced by the Raman spectra analysis method.

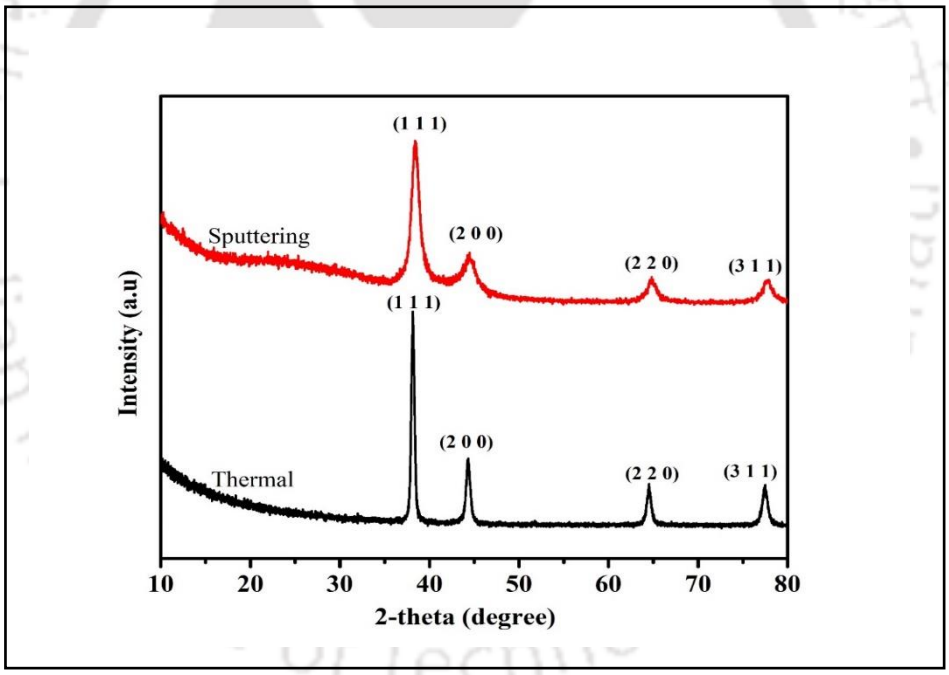

Figure 5.3: XRD spectra of Ag thin film through sputtering deposition (red) and thermal vapour deposition (black).

While examining X-ray diffraction pattern of Ag thin film as shown in Figure 5.3, four main peaks were found to be displayed at 2θ = 38.08◦, 44.26◦, 64.45◦, 77.42◦, and after indexing these peaks in (h k l) planes associated with the cubic Ag crystal planes (PDF No.: 00- 004-0783), their corresponding value were found out to be (1 1 1), (2 0 0), (2 2 0) and (3

1 1) respectively. The presence of these peaks was the confirmation of formation of metallic silver nanoparticles.

From the above X-ray diffraction pattern further structural analysis was performed. During this analysis the Bragg's law equation (1) was used to calculate the corresponding d-spacing values for both nanocrystalline TiO_2 thin films and Ag thin film deposited by thermal vapour deposition technique as well as sputtering technique

$$n\lambda = 2d \sin\theta \tag{5.1}$$

The crystallite size of all the three nanoparticles was determined from the integral width of the diffraction peaks using the well-known Debye-Scherrer's formula (Scherrer, 1918b):

$$D = \frac{k\lambda}{\beta\cos\theta} \tag{5.2}$$

Where;

k = 0.94,

λ = 1.5407Å,

β = Full Width Half Maximum (FWHM)

θ = Diffracting angle.

A dislocation is a defectiveness in a crystal. In other word, when there is defectiveness within the lattice structure of the crystal, it leads to the creation of dislocations. The dislocation density is the measurement of dislocation lines per unit volume of the crystal.

Dislocation density values 'δ' was determined by using the equation (Gapale et al., 2018b)

$$\delta = \frac{n}{D^2} \tag{5.3}$$

Where;

$'n'$ is the factor which is equal to unity for minimum dislocation density, and

'D' is the crystallite size in 'nm'.

Any displacements from the normal position of unit cells resulted into so called lattice microstrain. In Ag crystal, formation of microstrain is caused by the presence of three types of imperfections such as dislocation, stacking fault probability and lattice distortion.

The microstrain was calculated by using equation (Chenaina et al., 2021b)

$$\mu = \frac{\beta}{4\tan\theta} \tag{5.4}$$

Where;

$'\beta'$ is the full width half wave maximum of the (1 0 1) peak, and

'θ' is the Bragg angle.

The slight peak shift which can be seen while comparing the standard 2θ value with the observed 2θ value is due to stacking fault. Usually in a crystal, the fraction of layers where sequential stacking faults are taking place is denoted by stacking fault probability (α). The stacking fault probability (α) can be determined by the equation (Kite et al., 2018b)

$$\alpha = \frac{2\pi^2}{45\sqrt{3\,tan\,\theta}} \times \beta \tag{5.5}$$

Table 5.1 shows a comparative analysis of the microstructural properties of nanocrystalline TiO_2 thin film, thermal vapour deposited Ag thin film and Sputtering deposited Ag thin film.

Table 5.1: Microstructural properties of nanocrystalline TiO_2 thin film, thermal vapour deposited Ag thin film and sputtering deposited Ag thin film.

		Units	TiO_2 thin film	Ag thin film (thermal)	Ag thin film (sputtered)
Lattice constant	Tetragonal a = b c	Å	 3.7814 9.5342		
	Cubic a = b = c	Å		4.097	4.097
Unit cell volume	a^2c	$Å^3$	137.01		
	a^3	$Å^3$		69.15	68.78
Crystallite size (D)	Scherrer's formula	(nm)	13.77	14.62	9.57
Dislocation density(δ)	$\frac{n}{D^2}$	(line/m^2)	6.0×10^{15}	4.67×10^{15}	10.9×10^{15}
Microstrain (μ)	$\frac{\beta}{4\,tan\theta}$		0.23×10^{-3}	6.81×10^{-3}	10.38×10^{-3}

Stacking fault (α)	$\frac{2\pi^2}{45\sqrt{3tan\theta}}$		5.872×10^{-3}	4.04×10^{-3}	6.17×10^{-3}

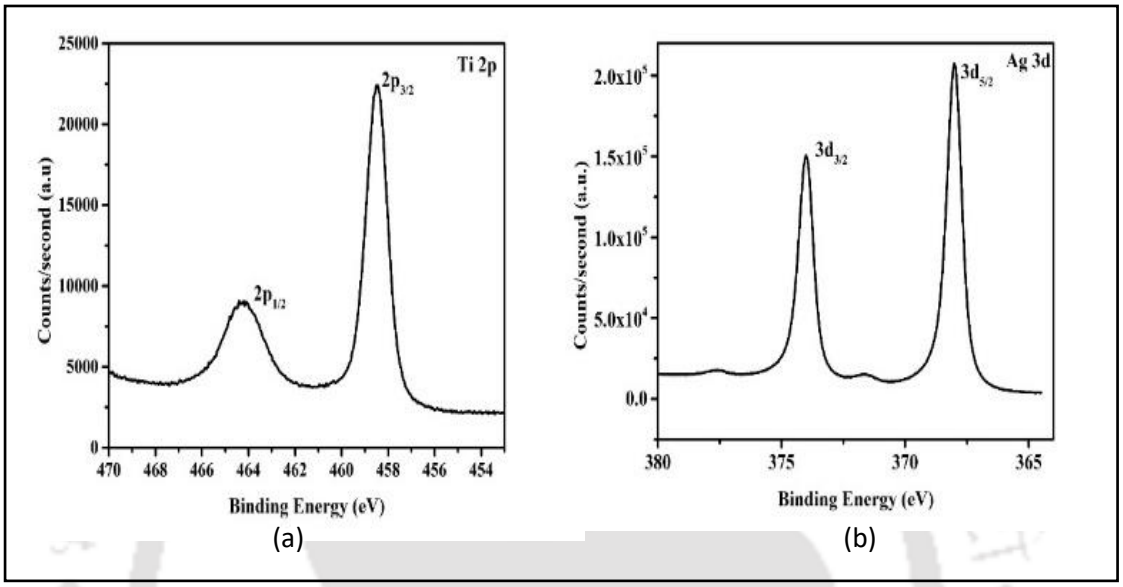

Figure 5.4: (a) XPS spectra of nanocrystalline TiO_2 thin film (b) Ag thin film deposited by thermal.

In order to confirm the integrity of the nanoparticle states of the constituent materials of the device which are TiO_2 and Ag, further investigation using XPS was performed.

The key indicator that was examined in XPS was that whether the silver nanoparticles were in the metallic Ag^0 state, and not in one of the oxidized states. Determining aforesaid indicator, the main objectives were to demonstrate that formation of silver oxides in the silver patches did not occur and also to check that the Ag did not penetrate into the TiO_2.

While examining the device using XPS, a point from the area of bare TiO_2 and a point from the area of Ag thin film over TiO_2 thin film were measured and results were shown in Figure 5.4 (a and b). Figure 5.4 (a) display XPS results for the Ti 2p core level and after analysing the result, the binding energy of the core electron corresponding to peak position Ti $2p_{3/2}$ is 459.24 eV which is a clear indication of the Ti^{+4} oxidation state and this is as expected for TiO_2 (Chashechnikova et al., 1993). Hence, this further prove that the integrity of the nanoparticle states of TiO_2 in the device remain intact which also means that Ag did

not penetrate into the TiO_2. Figure 5.4 (b) display XPS results for the Ag 3d core level and after analysing the result, the binding energy of the core electron corresponding to peak position Ag $3d_{5/2}$ is 368.30 eV, which is a clear indication of the Ag^0 metallic state (Morales et al., 2004).

While examining film topography of the TiO_2 thin films coated over FTO glass substrates, from the 2D & 3D images taken from AFM device with the sample scan area of 5μm × 5μm, it was noticed that the surface of the film has different topography and the grain sizes, which is displayed in Figure 5.5. Also, since no cracks was found during this examination, it was therefore confirm that the deposited films is compact type topography.

Similarly, topography of the Ag thin films deposited over TiO_2 by sputtering as well as thermal vapour deposition technique were examined from the 2D & 3D images taken from AFM device with sample scan area of 5μm × 5μm and noticed a larger grain sizes of the sample resulted from the thermal vapour deposition technique, which is displayed in Figure 5.5 (b) and (c) below.

The determined Rq (RMS) values of the Ag thin film samples of sputtering as well as thermal vapour deposition technique were 24.71 and 21.9 nm, respectively and from this we could conclude that surface roughness was less of the sample resulted from the thermal vapour deposition technique.

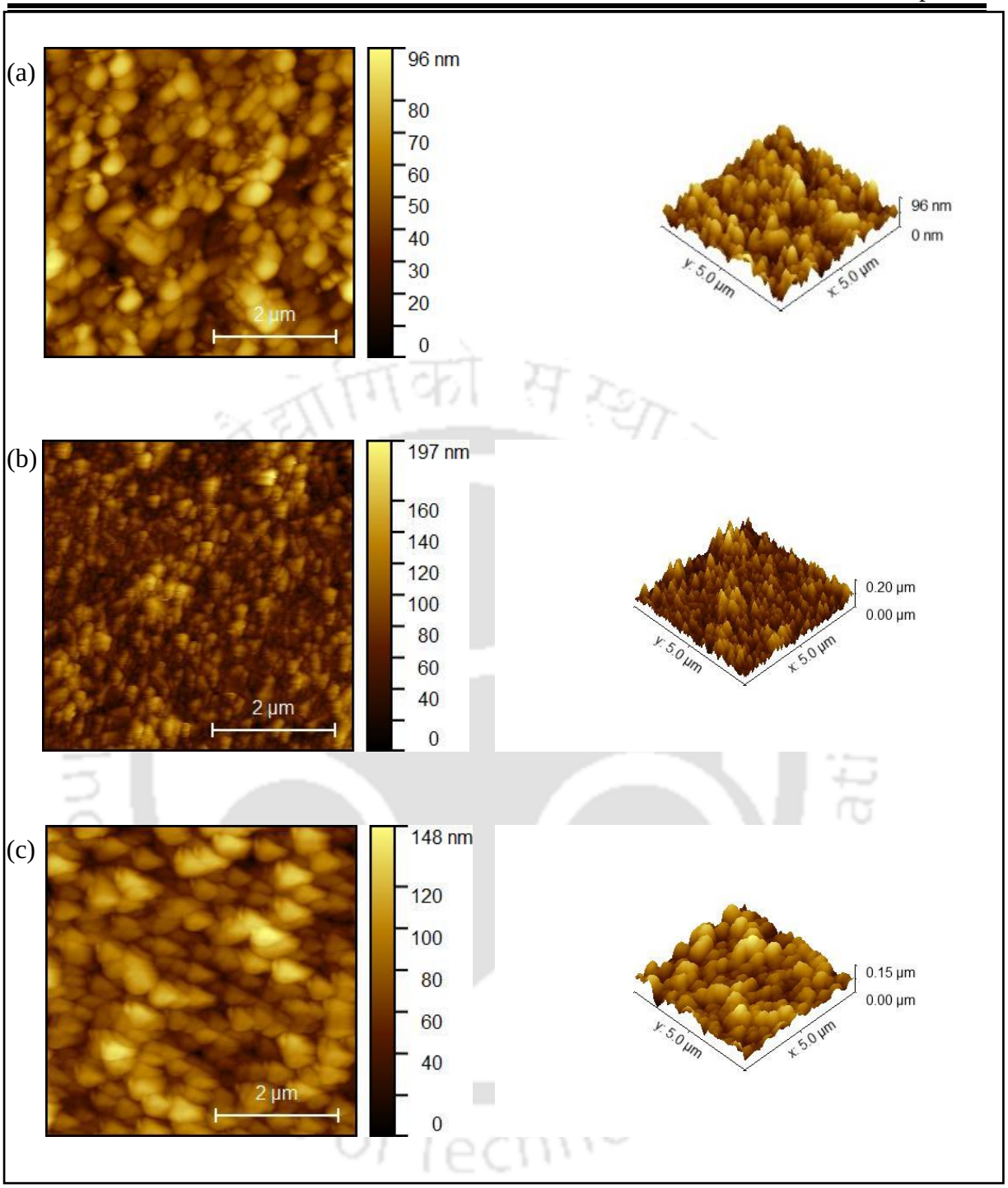

Figure 5.5: 2D (left) and 3D (right) image of (a) nanocrystalline TiO_2 thin film, (b) sputtered Ag thin film and (c) thermally deposited Ag thin film.

Although the images taken from AFM were sufficient to carry out analsysis and to draw results, but a visual confirmation could further reinforce the aforesaid results by analysing better morphological details from the magnified images taken from FESEM.

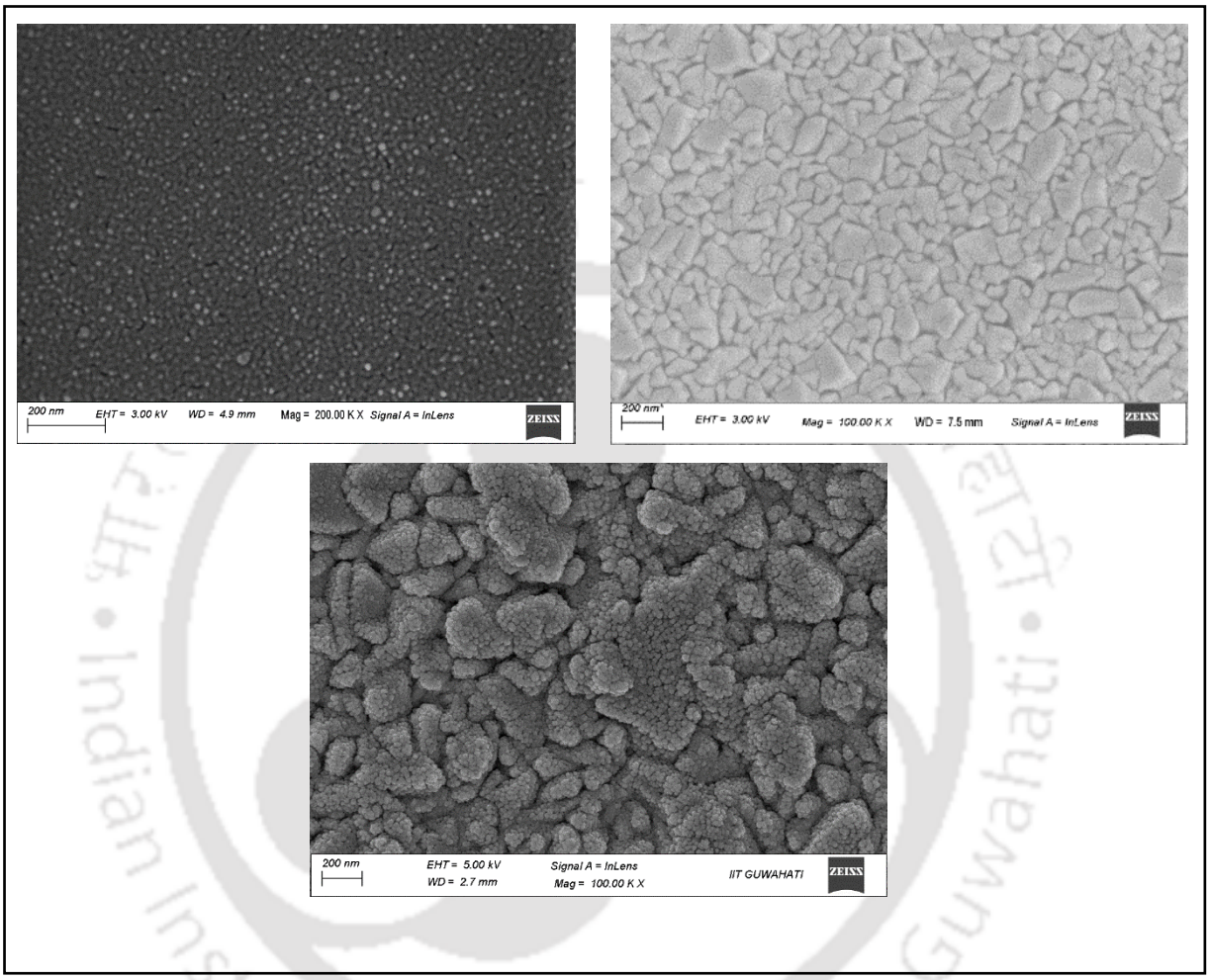

Figure 5.6: FESEM image of (a) nanocrystalline TiO_2 thin film, (b) sputtered Ag thin film and (c) thermally deposited Ag thin film.

Figure 5.6 (a) dispalyed FESEM image of nanocrystalline TiO_2 thin film whereas Figure 5.6 (b) and (c), dispalyed FESEM image of Ag thin film deposited over TiO_2 by thermal vapour deposition technique and sputtering technique, respectively. From this image, it was therefore re-confirmed that the deposited TiO_2 thin films was compact type morphology. Whereas with regard to Ag thin film, it was further re-confirmed that grain sizes noticeably larger of the sample resulted from the thermal vapour deposition technique.

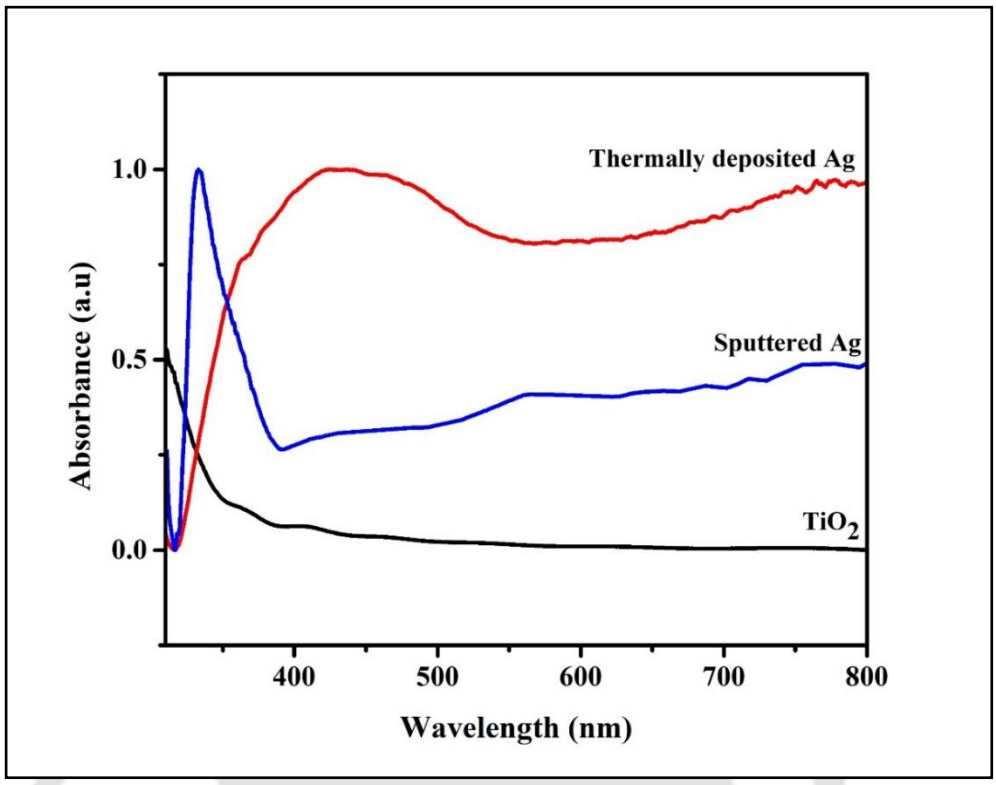

Figure 5.7: Absorption spectra of nanocrystalline TiO_2 thin film (black), sputtered Ag thin film (blue) and thermally deposited Ag thin film (red).

In order to examine optical behaviours of the nanoparticles, the values obtained from the UV-Vis spectrophotometer were plotted in the absorption spectra and analysed. In the Figure 5.7, black curve represents absorption spectra of the TiO_2, blue curve represents absorption spectra of the Ag thin film deposited by sputtering technique and red curve represents absorption spectra of the Ag thin film thermal vapour deposition technique. By examining absorption spectra of the TiO_2, it is clearly noticed that nanocrystalline TiO_2 thin film does not absorb any light within the visible range of light (400 – 700 nm). On the other hand, the performance of Ag nanostructure thin films are influenced by many factors, such as the shape of nanostructures, their size, fluctuations in the electronic structure, or the dielectric function of the medium in which such nanostructures are dispersed (Khan et al., 2019; Kozioł et al., 2020). So, absorption spectra of the Ag thin film obtained via sputtering exhibits maximum absorption in UV range with its peak at 300nm and drops suddenly at the onset of the visible range of light and slightly increases towards the extreme end of the visible range. Whereas absorption spectra of the Ag thin film obtained via thermal vapour deposition exhibits maximum absorption in the visible range of light with its peak at 430 nm and

maintains its absorbance throughout the visible range with minor fluctuations. However, it is evident that absorbance of Ag thin film obtained via thermal vapour deposition is superior over absorbance of Ag thin film obtained via sputtering.

5.5 Testing of Fabricated Device

The J-V curves obtained from the solar simulator, as detailed in the characterization section, were examined.

These findings hold the potential to advance the creation of solid-state plasmonic photovoltaic cells. Figure 5.8 shows the J – V curve of best TiO_2|Ag solid state plasmonic photo-electric conversion device prepared separately on TiO_2 with thermally deposited Ag nanoparticles (deposition time of 400 s which is 300 nm thickness).

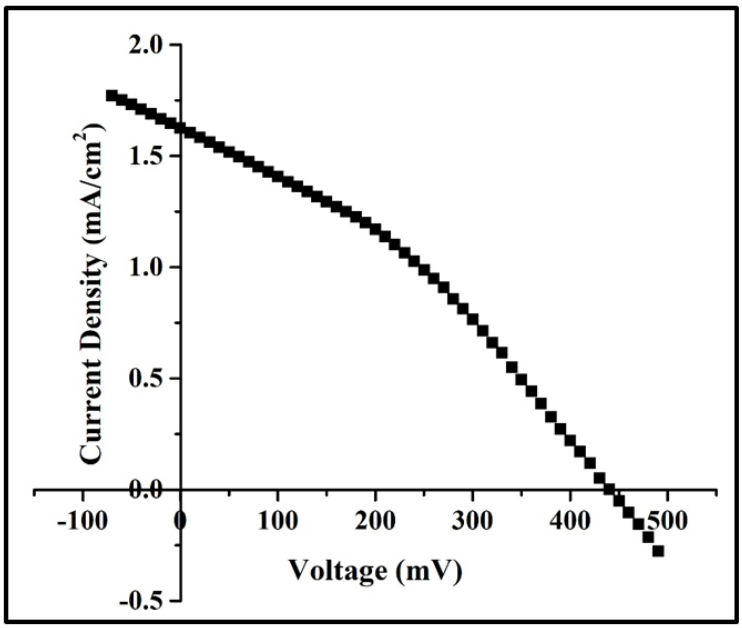

Figure 5.8: J-V curves of best performance TiO_2|Ag plasmonic energy harvesting device.

The best cell performances were observed with thermally deposited Ag nanoparticles which gives a short circuit current of 1.6 mA cm^{-2} and open circuit voltage of 440 mV, with a fill factor of 0.3 and efficiencies of 0.2 % (all these measurements are calculated in the solar simulator itself). These photocurrent levels represent the highest reported value for TiO_2|Ag solar cells as we know so far.

5.6 Working Principle

The suggested energy band diagrams for both pristine TiO_2 and the TiO_2|Ag independent plasmonic photo-electric conversion device are illustrated in Figure 5.9 (a and b) respectively.

These band diagrams were derived based on KPFM measurements and the band gap calculation obtained from UV measurements data. The TiO_2 band gap was determined as 3.47 eV using UV-Vis absorption data as described in chapter 4.

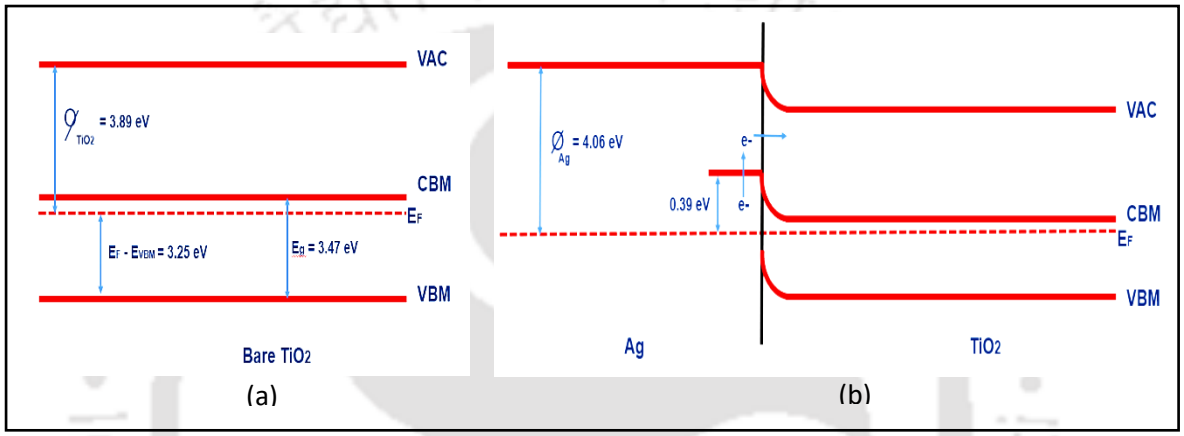

Figure 5.9: (a) Energy band diagram of the bare TiO_2, showing that the TiO_2 is highly n-doped. (b) Energy band alignment diagram of the TiO_2|Ag plasmonic energy harvesting device. The TiO_2 has a band bending that is larger than 390 meV, which corresponds to the Voc values.

For bare TiO_2, the energy difference between the Fermi level (E_f) and the valence band maximum (VBM), denoted as $E_f - E_{VBM}$, was determined to be 3.25 eV, in agreement with earlier findings (Pfeifer et al., 2013). This energy gap situates the Fermi level roughly 0.2 eV below the conduction band minimum (CBM) in the case of bare TiO_2, signifying a substantially n-doped layer of TiO_2. The energy band alignment of the independent plasmonic solar cell TiO_2|Ag is presented in Figure 5.9(b)

In order to explore the functioning mechanism of these solar cells, we executed measurements using Kelvin probe force microscopy. Following tip-based calibration, the work function was identified as 4.22 eV, leading to subsequent adjustments in all measurements accordingly. Evaluations of the Ag nanoparticles exhibited a work function of

4.06 eV, while the Fermi level of the TiO_2 thin film registered at 3.89 eV. These measurements collectively imply the presence of a Schottky barrier height measuring 0.39 eV between the Ag nanoparticles and the TiO_2 layer.

To overcome the Schottky barrier, the hot electrons need to possess energy levels surpassing 0.39 eV. As the Localized Surface Plasmon Resonance (LSPR) undergoes a non-radiative decay process, the energy transferred to the hot electron typically ranges from 1 eV to 4 eV. This range is contingent upon factors such as particle size, shape, and composition (Linic et al., 2011b; Sönnichsen et al., 2002)(Linic et al., 2011b). Consequently, the high energy state of the hot electrons originating from the Ag nanoparticles empowers them to conquer this obstacle and infuse into the TiO_2 conduction band. Simultaneously, the hole created within the Ag nanoparticle is compensated for by the FTO film. In detail, the hot electrons, energized to a significant degree, originating from the conduction band of the Ag nanoparticles acquire enough energy to surpass the Schottky barrier positioned between the Ag nanoparticles and the TiO_2 layer. The mechanism through which these hot electrons are injected into the TiO_2 is enabled by the substantial density of states (DOS) present within the conduction band of the TiO_2 layer (Clavero, 2014).

In the TiO_2|Ag solar cells, the Ag, direct thermally deposited onto the rough TiO_2 surface, serves a triple purpose. Firstly, it establishes a Schottky barrier junction with the TiO_2 layer. Secondly, acting as the rear contact material, it facilitates the conduction of the generated holes within the solar cells towards the electrical contacts. Lastly, the incoming light is absorbed by the Ag nanoparticles, inducing SPR. During the decay of SPR to its ground state, "hot" non-equilibrium electrons are generated, capable of being injected into the TiO_2 layer, thereby generating photocurrent and photovoltaic activity.

It is worth noting that the process of "hot" electron injection into the TiO_2 happens rapidly. Research involving gold nanoparticles in the absence of a hole transport layer has indicated that 'hot' electron injection transpires within 50 femtoseconds (fs) after their generation (Du et al., 2013). In the case of silver nanoparticles, the generation of 'hot' electrons occurs even more rapidly, unfolding in under 30 femtoseconds (fs), (Voisin et al., 2001) subsequently followed by electron-electron scattering and thermalization in approximately 100 fs (Clavero, 2014). Drawing from these documented timeframes, it is

proposed that within our solar cells, which do not incorporate a hole transport layer, the injection of 'hot' electrons from Ag into TiO_2 transpires within time intervals spanning from 30 to 100 fs.

Incorporating a hole transport material has the potential to enhance the efficiency of our TiO_2|Ag solar cells, possibly leading to shortened injection times and mitigating the recombination of 'hot' electrons in Ag with oxidized silver atoms in close proximity.

5.7 Conclusion

In summary, this investigation has examined the properties and potential applications of nanocrystalline TiO_2 and Ag thin films. Through a combination of analytical techniques including XRD, Raman spectroscopy, and FESEM, we have gained a thorough understanding of the structural characteristics of these films. Our findings unequivocally confirm the presence of pure anatase-phase TiO_2 in the fabricated thin films, while also demonstrating the formation of metallic silver nanoparticles in the Ag thin films over TiO_2 films. The structural analysis further revealed essential parameters such as crystallite size, dislocation density, microstrain, and stacking fault probability, shedding light on the films' integrity and quality. Moreover, AFM and FESEM showcased the compact nature of the TiO_2 films and the larger grain sizes in the Ag films produced via thermal vapor deposition over sputtering deposition. The optical properties assessment has highlighted that the TiO_2 thin films exhibit minimal absorption in the visible light spectrum, making them suitable for transparent applications. Conversely, the Ag thin films exhibited distinct absorption characteristics, with the thermally deposited Ag film displaying superior absorbance within the visible range. The performance of the plasmonic photo electric conversion device fabricated by incorporating these thin films was evaluated, and promising results were achieved. The best-performing TiO_2|Ag plasmonic photo electric conversion device demonstrated short-circuit currents of up to 1.6 mA cm^{-2} and open-circuit voltages of approximately 440 mV, yielding an efficiency of 0.2%. These findings underscore the potential for the development of cost-effective and structurally simple solid-state plasmonic photovoltaic cells with two-dimensionally distributed photosensitizers. The working principle of these plasmonic photo electric conversion device, elucidated through energy band diagrams and Kelvin probe force microscopy measurements, revealed the presence of a Schottky barrier height between Ag

nanoparticles and the TiO_2 layer. Importantly, it was determined that high-energy hot electrons originating from Ag nanoparticles can surmount this barrier, infusing into the TiO_2 conduction band and generating photocurrent.

In short, this study has not only deepened our understanding of the structural and optical properties of nanocrystalline TiO_2 and Ag thin films but has also demonstrated their potential for use in solar cell applications. These findings offer valuable insights into the development of advanced photovoltaic technologies and underscore the importance of further research in harnessing the unique properties of these materials for sustainable energy generation.

CHAPTER 6

SYNTHESIS AND CHARACTERIZATION OF SILVER-GRAPHENE HYBRID NANOCOMPOSITES

CHAPTER 6

SYNTHESIS AND CHARACTERIZATION OF SILVER-GRAPHENE HYBRID NANOCOMPOSITES

6.1 Overview

Graphene is a carbon sheet of single atom thickness made from layers of two dimensional sp^2 bonded carbon in a honeycomb style crystal structure (Geim & Novoselov, 2007). This nanomaterial is extremely thin and it exhibits very interesting properties such as high mechanical stiffness (Balandin et al., 2008), extraordinary electronic transport properties (Li et al., 2008a) and excellent antibacterial activity (Hu et al., 2010) that can be utilized for many carbon-based device architectures. There are certain approaches by which graphene can be fabricated promisingly, some of which can be named are mechanical exfoliation ("Scotch-tape" method) of bulk graphite (Novoselov et al, 2016), epitaxial chemical vapour deposition on substrates (Berger et al., 2006) and chemical vapour deposition starting from carbon precursors (Soldano et al., 2010). Although these methods are useful for precise device assembly, they become less effective for large-scale manufacturing. However, in recent years, much attention has been paid on the chemical efforts, involving exfoliation starting from the oxidation of graphite and post-reduction, due to its ability to produce graphene in a large-scale (Li & Kaner, 2008)(Zhao et al., 2010).

Moreover, graphene inspite of having unique nanostructure and fascinating properties, when decked with various inorganic nanoparticles, such as platinum (Qian et al., 2011) , gold (Xu et al., 2008), silver (Yang et al., 2011), cadmium-selenide (Gao et al., 2012), titanium-dioxide (Liu, et al., 2011), ferric-oxide (Zhou et al., 2010), and zinc-oxide (Yahiya et al., 2021), are very remarkable contenders for electrochemistry, electronics, catalysis and optics etc. Among above mentioned nanocomposites, silver graphene nanocomposites performs remarkably well (Hranisavljevic et al., 2002)(Nanoclusters et al., 2004). In fact, it is known that silver-graphene nanocomposite is a very effective and promising material due to its potential applications in various fields. In this regard, some researchers had already carried out synthesis which came to our attention. Pasricha *et al.* (Pasricha et al., 2009) has presented preparation process of GNS/AgNPs in just two simple stages, whereby, at first, GO/AgNPs were produced and later, hydrazine was introduced to remove the oxygen. Shen

et al. (Shen et al., 2010) also presented a process of fabricating silver graphene nanocomposites with the help of chemical agents, whereby, chemical reduction of silver ions were achieved from the suspension of chemically converted graphene (CCG) by mixing reducing agents such as, $NaBH_4$ and ethylene glycol. It was also later revealed that the free AgNPs present in those nanocomposites exhibited the same quality of antibacterial properties. From this finding, it suggested that these nanocomposites could be effectively utilized in the area of graphene-based biomaterials. Moreover, Liu *et al.* (S. Liu et al., 2011) presented preparation process of GNS/AgNPs using a new reduction technique supported by microwave from GO and $AgNO_3$ using DMF as a reducing agent and solvent, in which the resultant compounds displayed a profound catalytic action through reduction of hydrogen peroxide. Chao Lu *et al.* (C. Lu & Chen, 2021) reported silver nanoparticles decorated graphene composites as electrode materials for efficient electrochemical energy storage and used ammonia water and hydrazine as reducing agent. However, all these aforesaid methods of synthesis are complicated, time-consuming as well as reducing agents of highly toxic in nature were used which in turn harm the environment, that limits their further practical applications. Therefore, it becomes necessary to look into a new reducing agent which causes less harm to environment for producing silver graphene nanocomposites in large quantity.

Herein, a comparatively simpler and less expensive process has been reported to synthesise silver graphene hybrid nanocomposites using a non-toxic as well as very environment friendly reducing agent, sodium citrate. A systematic study on the structural, morphological and optical properties of the synthesized nanocomposites was carried out through various characterization techniques like XRD, Raman spectroscopy, UV visible spectroscopy, FTIR and FESEM. Detailed accounts on the findings are reported here.

6.2 Experimental Approaches

6.2.1 Materials

Sourcing the right material is the most significant part of this experiment as the desired result of this experiment is depended on it. So, it is very important to source an analytical grade material from a reliable supplier. Graphite powders with an average particle size of less than 20 μm, H_2O_2 (30%), $KMnO_4$, $C_6H_5O_7Na_3 \cdot 2H_2O$, $AgNO_3$ and ethanol were procured from Sigma Aldrich (India). Hydrochloric acid (HCl - 37%), Sulphuric acid (H_2SO_4

- 98%) and Phosphoric acid (H_3PO_4-85%) were procured from Thermo Fischer scientific, India.

6.2.2 Preparation of Graphene Oxide (GO)

GO was synthesized using Improved Hummer's method (Marcano et al., 2010). Figure 6.1 explains the preparation of GO. Graphite powder (3 gm) was added to 400 ml of 9:1 mixture of H_2SO_4 and H_3PO_4 solution. 18 gm of $KMnO_4$ was added to the mixture slowly while stirring with a glass rod. The flask was kept in an ice bucket as the reaction is exothermic. The mixture was vigorously stirred for up to 10 hrs on a magnetic stirrer. After that 400 ml of millipore water was added and simultaneously 3ml of H_2O_2 was added in order to cease the reaction. The mixture was then filtered over a PTFE membrane of 0.45 μm pore size using vacuum filtration unit. The filtrate was subsequently washed with millipore water until pH7 solution was obtained. The precipitate was further washed with few drops of HCl (conc. 37%) so as to remove any metal impurity and later it was again washed with 200 ml of ethanol for two times successively. The filtrate was then left to dry in a hot air oven

Graphite powder and $KMnO_4$ were added to H_2SO_4: H_3PO_4(9:1) solution. (Exothermic)

- Vigorously stir the mixture for 10 hrs.
- Then add millipore water to the solution for oxidation.
- Simultaneously add H_2O_2 to stop the reaction

Filter the solution over a PTFE membrane with 0.45µm pore size.

Dry the precipitate in hot air oven

Graphene oxide

Figure 6.1: Experimental procedure for synthesizing graphene oxide.

6.2.3 Preparation of Silver Graphene Hybrid Nanocomposites

Step-1- Three solutions each consisting of 50 mg GO were dispersed in 25 ml water using ultra sonification for 1 hr in equally size conical flasks termed as flask-A, B and C.

Step-2- 50 mg of $AgNO_3$ was added in flask-A making 1:1 ratio of GO and $AgNO_3$. Similarly, 100 mg of $AgNO_3$ was added in flask-B making 1:2 ratio of GO and $AgNO_3$. Finally in flask-C, 150 mg of $AgNO_3$ was added making 1:3 ratio of GO and $AgNO_3$. Later, all the three flasks were kept on a magnetic stirrer and stirred.

Step-3- 1 gm of sodium citrate was added and stirred the mixture for 30 minutes.

Step-4- The mixtures were transferred to a hot water bath shaker and maintained at 95^{o}C for 10 hrs in a constant stirring condition. The mixture was allowed to cool down naturally and later it was washed with ethanol and millipore water using centrifugation. The final product was left to dry in a vacuum concentrator at 60^{o}C for 2 hrs.

➢ Graphene Oxide + H_2O
(3 solutions were prepared in 3 separate flask)

➢ Ultrasonification for 1 hour

$AgNO_3$ (50 mg, 100 mg, 150 mg) and 1g of sodium citrate is added successively to each solution respectively and stir the mixture for 30 minutes

The solution is transferred to a hot water bath shaker and kept at 95^oC for 10 hrs

The mixture is cooled down naturally then washed with ethanol and DI water

The precipitate is dried in a vacuum concentrator at 60^oC for 2 hrs

The final product silver graphene hybrid nanocomposites

Figure 6.2: Experimental procedure for preparing silver-graphene hybrid nanocomposites

6.3 Characterization Techniques

To perform characterization of freshly formed silver-graphene hybrid nanocomposites, various measurements were taken using XRD. The operating voltage of XRD was 45 kV at 200 mA current. Also, a diffractometer of Rigaku SmartLab with Cu-Kα radiation (λ = 1.54 Å) was used for scanning purpose. The scanning of hybrid nanocomposites was performed within the range starting from 5° to 80° of 2θ at a rate of 5°/min. An Integrated X-Ray Diffraction Software, PDXL, was used in order to further analyse the results. For analysis of XRD pattern and benchmarking, ICDD (International Centre for Diffraction Data) PDF files were used. For taking Raman spectroscopy, a Spectrophotometer of Horiba Jobin Vyon make LabRam HR model was used and excitation was carried out with an Argon ion laser of 633 nm with 50X zoom. The time taken for acquisition was 10 seconds. For measuring spectral absorbance, a UV-Visible spectrophotometer of Cary 5000 UV-VIS-NIR of Agilent Technologies was used at wavelengths ranging between 300 and 800 nm. Fourier transform infra-red (FTIR) spectra were recorded with a PerkinElmer, Singapore make Spectrum two model of FTIR Spectrometer. For examining the morphology of the hybrid nanocomposites, a FESEM of Ziess make Sigma 300 model and FETEM of Jeol make 2100F model was used.

6.4 Results and Analysis

6.4.1 X-Ray Diffraction Analysis

In this section, the method of analysis and its results were presented in detail, for silver-graphene hybrid nanocomposites in X-ray diffraction. X-ray diffraction patterns of the G, GO and AgNPs/GNS hybrid nanocomposites are presented in Figure. 6.3. By analysing the XRD pattern of G indicated by Figure. 6.3(a), a characteristic peak (0 0 2) of graphite was observed at 26.5^{o} which correspond to the crystalline nature of the material (PDF Card No.: 00-041-1487).

This position peak of native graphite powder (0 0 2) at 26.5^{o} disappeared after oxidation which was indicated by Figure. 6.3(b), and at the same time, it was also noticed that the diffraction peak of GO (0 0 1) appeared at 10.24^{o} that correspond to 8.5 Å interlayer spacing against 3.35 Å interlayer spacing of graphite powder. This significant increase in the interlayer distance from 3.25 Å to 8.5 Å was as a result of the chemical oxidation. Meanwhile,

by analysing, XRD pattern of the AgNPs/GNS represented by Figure. 6.3(c), (d) and (e), four main peaks were noticed at 2θ = 38.08◦, 44.26◦, 64.45◦, 77.42◦, which are associated with the (PDF No.: 00- 004-0783) cubic Ag crystal planes (1 1 1), (2 0 0), (2 20) and (3 1 1) respectively. This was a clear indication of the formation of metallic silver nanoparticles.

For further analysis, the Bragg's law equation (6.1) was used to calculate the corresponding d-spacing values of the silver nanoparticles

$$n\lambda = 2d \sin\theta \tag{6.1}$$

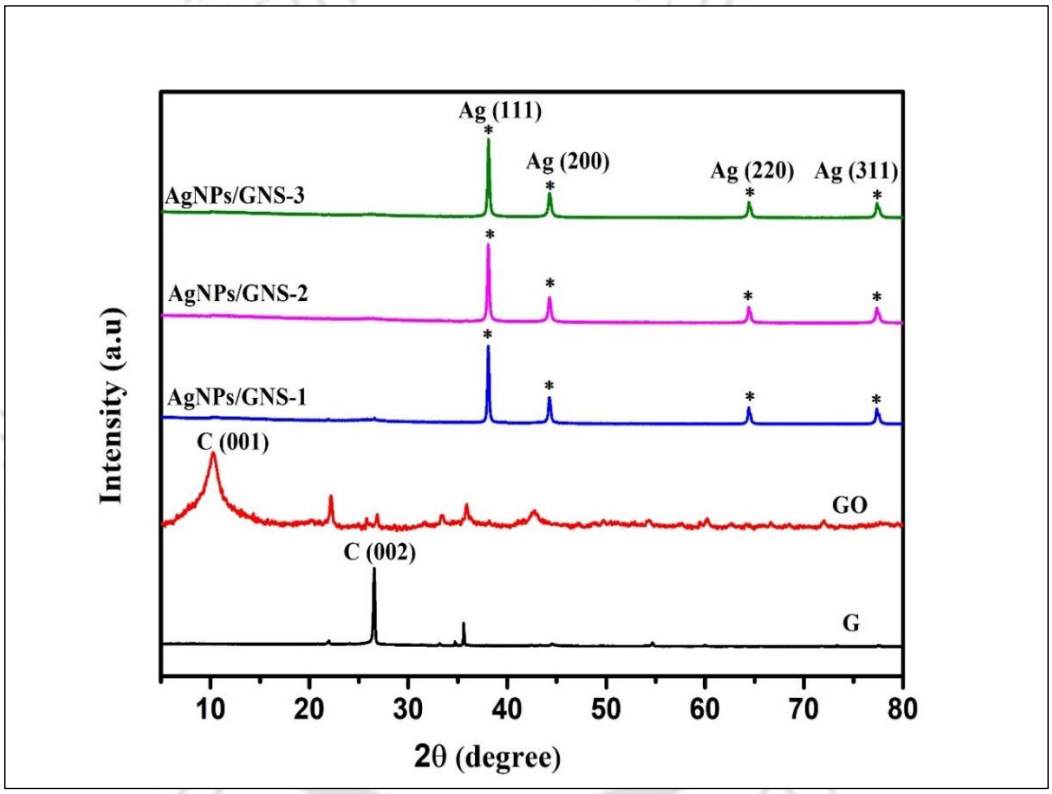

Figure 6.3: XRD pattern of (a) G, (b) GO, (c) AgNPs/GNS-1, (d) AgNPs/GNS-2 and (e) AgNPs/GNS-3.

A comparison of the calculated d-values of the silver nanoparticles with the standard value of PDF No.: 00- 004-0783 was carried out and found that they were very much congruent with the standard d-values of cubic Ag crystal, as also can be seen in Table 6.1. Moreover, it was also noticed that the d-spacing value of the silver nanoparticles which were synthesized in dissimilar dosage of the $AgNO_3$ was remained nearly alike for every crystallographic plane.

Table 6.1: Crystallographic data of the cubic Ag crystals.

2θ (degree)		**d-spacing (Å)**	
Observed	**Standard**	**Calculated Value**	**Standard**
38.09	38.12	2.361	2.359
44.28	44.28	2.044	2.044
64.45	64.43	1.445	1.445
77.42	77.47	1.232	1.231

Furthermore, in Table 6.2, microstructural properties of some (hkl) planes of silver nanoparticles were summarized. Determination of such microstructural properties were achieved with the help of following equations.

6.4.2 Crystallite Size of the Silver Nanoparticles (D)

The crystallite size of the silver nanoparticles was determined from the integral width of the diffraction peaks using the well-known Debye-Scherrer's formula (Devi et al., 2022)

$$D = \frac{k\lambda}{\beta\cos\theta} \tag{6.2}$$

Where:

k = 0.94,

λ = 1.5407Å,

β = Full Width Half Maximum (FWHM)

θ = Diffracting angle.

6.4.3 Dislocation Density

A dislocation is a defectiveness in a crystal. In other word, when there is defectiveness within the lattice structure of the crystal, it leads to the creation of dislocations. The dislocation density is the measurement of dislocation lines per unit volume of the crystal.

Dislocation density values 'δ' was determined by using the equation (Devi et al., 2022).

$$\delta = \frac{n}{D^2} \tag{6.3}$$

Where;

$'n'$ is the factor which is equal to unity for minimum dislocation density, and

'D' is the crystallite size in 'nm'.

6.4.4 Microstrain

Any displacements from the normal position of unit cells resulted into so called lattice microstrain. In Ag crystal, formation of microstrain is caused by the presence of three types of imperfections such as dislocation, stacking fault probability and lattice distortion.

The microstrain was calculated by using equation (Devi et al., 2022)

$$\mu = \frac{\beta}{4 \tan \theta} \tag{6.4}$$

Where;

$'\beta'$ is the full width half wave maximum of the (1 0 1) peak, and

'θ' is the Bragg angle.

6.4.5 Stacking Fault Probability

The slight peak shift which can be seen while comparing the standard 2θ value with the observed 2θ value is due to stacking fault. Usually in a crystal, the fraction of layers where sequential stacking faults are taking place is denoted by stacking fault probability (α). The stacking fault probability (α) can be determined by the equation (Kite et al., 2019)

$$\alpha = \frac{2\pi^2}{45\sqrt{3\,tan\,\theta}} \times \beta \tag{6.5}$$

Table 6.2: Microstructural properties of some hkl planes of the cubic Ag crystals.

2θ	(hkl)	d-spacing (Å)	FWHM (rad)	Crystallite size (nm)	Microstrain ($\mu \times 10^{-3}$)	Dislocation density (line/m^2)	Stacking fault ($\alpha \times 10^{-3}$)
38.09	(1 1 1)	2.361	0.0039	34.5	2.9	0.84×10^{15}	1.7
44.28	(2 0 0)	2.044	0.0049	27.1	3	1.36×10^{15}	1.9
64.45	(2 2 0)	1.445	0.0056	21.8	2.2	2.11×10^{15}	1.7
77.42	(3 1 1)	1.232	0.0072	15.6	2.2	4.11×10^{15}	2

6.4.6 Raman Spectra Analysis

While looking for a direct and non-destructive characterization technique, Raman spectroscopy was found suitable as it caused minimum or no distortion to the specimens. So, it was used for analysing the changes between GO and freshly synthesized AgNPs/GNS hybrid nanocomposites. Figure. 6.4 (a, b and c) represents Raman spectra of parent graphite (G), GO and freshly formed AgNPs/GNS hybrid nanocomposites respectively.

From the Raman spectra of graphite (G) shown below in Figure. 6.4(a), two distinct peaks were observed at 1326 cm^{-1} (D band) and at 1571 cm^{-1} (G band) and as we understand they correspond to the breathing mode of Ҡ-point phonons of A_{1g} symmetry and the E_{2g} phonon of C sp^2 atoms, respectively (Ferrari et al., 2006). Whereas in the Raman spectra of GO shown in Figure. 6.4(b), the aforementioned peaks of both D band and G band were widened and shifted to 1358 cm-1 and 1593 cm-1 respectively. The Raman spectrum of AgNPs/GNS shown in Figure. 6.4(c), its corresponding D band and G band were observed at 1330 cm^{-1} and 1597 cm^{-1}respectively.

Later a comparison was made between the ratio of the D and G bands (I_D/I_G), of GO with that of parent graphite, and observed an increment in the value from 0.84 to 1.04. This was an indication of disorder at a high level and the presence of a higher number of defects in GO layers.

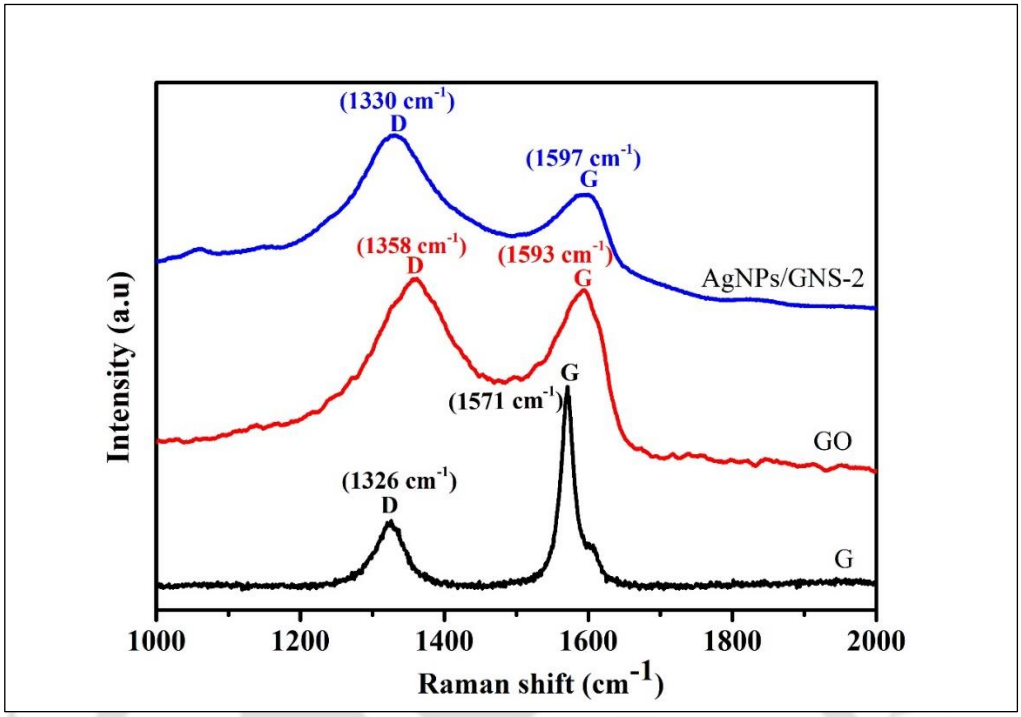

Figure 6.4: Raman spectra (633nm excitation) of (a) G, (b) GO, (c) AgNPs/GNS-2.

Similarly, when comparing the I_D/I_G ratio of AgNPs/GNS hybrid nanocomposites material with that of GO, a further increment in the value from 1.04 to 1.40 was noticed. This was due to the fact that during the reduction process, most of the oxygen-containing groups were escaped from the sample, and in their places, conjugated G network (sp^2 carbon) was then re-established, but, this re-established G network was smaller in size than the original one, therefore, it led to increment in the I_D/I_G ratio (Stankovich et al., 2007).

The D band position, G band position and ratio of the intensities of the D and G bands (I_D/I_G) of each specimen are presented in Table 6.3.

Table 6.3: Raman data of G, GO and AgNPs/GNS-2.

Sample	**D band position (cm^{-1})**	**G band position (cm^{-1})**	**I_D/I_G**
G	1326.03	1571.10	0.84
GO	1358.73	1593.46	1.04
Ag/G-2	1329.86	1596.69	1.40

From this phenomenon of increase in the I_D/I_G ratio, the following two conclusions can be realized:

I. It indicates the presence of a reduction procedure of GO.

II. The peak intensity of silver graphene hybrid nanocomposites is significantly higher than that of both GO and graphite, which is due to SERS, which resulted from a strong local electromagnetic field of Ag nanoparticles and is also accompanied by its plasmon resonance (Li & Liu, 2010).

6.4.7 FT-IR Spectra Analysis

The freshly synthesized GO and AgNPs/GNS hybrid nanocomposites samples were further analysed using FTIR spectroscopy and the results were presented in Figure. 6.5. From Figure. 6.5(a), which represents the FTIR spectrum of GO, the exhibited peaks at 1715 cm^{-1}, 1620 cm^{-1}, 1568 cm^{-1}, 1391 cm^{-1} and 1063 cm^{-1} correspond to C=O stretching vibration, skeletal vibration of unoxidized graphitic domains, skeletal vibration of graphene sheets, O-H deformations of the C-OH groups and sp^3 C-O stretching vibrations, respectively (Guo et al., 2009).

Whereas in Figure 6.5(b) which represents the FTIR spectrum of silver graphene hybrid nanocomposites, the exhibited peaks at 1063 cm^{-1}, 1391 cm^{-1},1715 cm^{-1} and 1620 cm^{-1} were becoming considerably weak. Moreover, a new absorption peak was noticed around 1385cm^{-1} which was associated with the O-H deformation vibration, and a new absorption band was also noticed at 1576 cm^{-1} which was associated with the skeletal vibration of the graphene sheets (Nethravathi & Rajamathi, 2008).

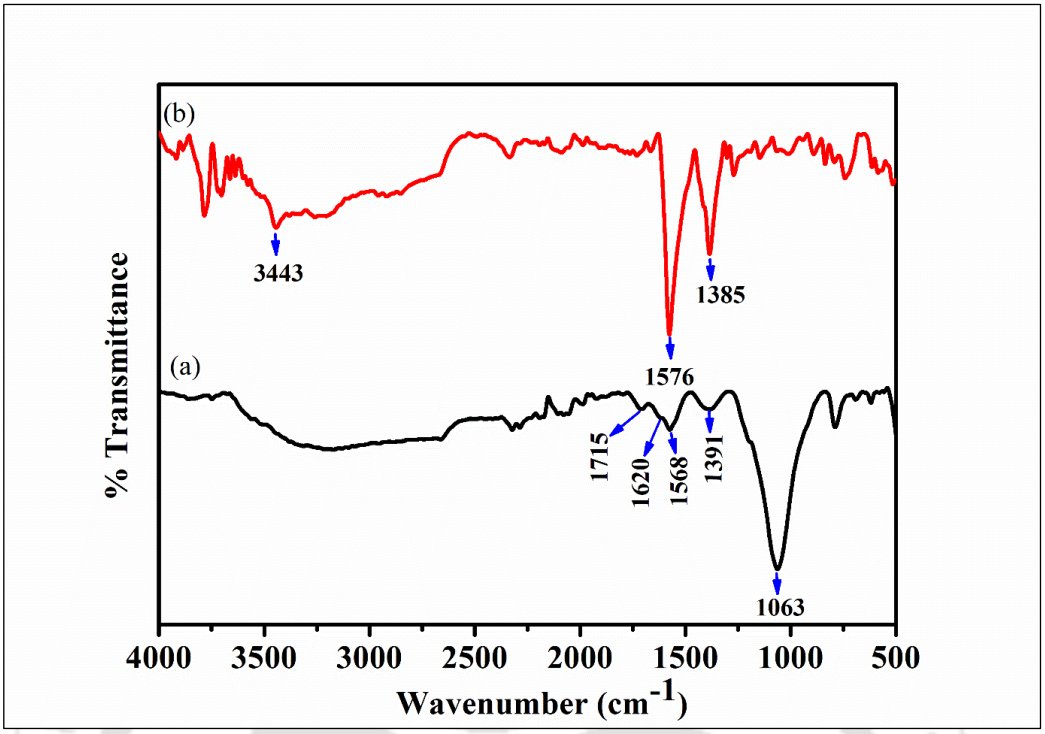

Figure 6.5: FT-IR spectra of (a) GO, (b) AgNPs/GNS-2.

Therefore, from the analysis of the FTIR results, it is clearly understood that the GO was effectively exfoliated and later reduced to graphene nanosheets, and strong connections were noticed to present between silver nanoparticles and the residual surface hydroxyl groups (Hull et al., 2006).

6.4.8 UV-Visible Spectra Analysis

Optical analysis of GO and AgNPs/GNS hybrid nanocomposites was carried out using UV visible spectroscopy. UV-Vis absorption spectra exhibited by GO have a peak and a hump as shown in Figure. 6.6(a). The peak at 226 nm correlates to π-π* transitions of aromatic C–C bonds, and the hump at 306 nm correlates to n-π* transitions of C=O bonds (Paredes et al., 2008).

Figure 6.6(b) shows the UV-Vis absorption spectra of AgNPs/GNS hybrid nanocomposites and it exhibits two distinct peaks at 292 nm and 420 nm. The C-C bond of GO at 226 nm was redshifted towards 292 nm in AgNPs/GNS hybrid nanocomposites, which was due to the treatment of sodium citrate and hot water bath thermal reduction that were used while doping Ag into GO.

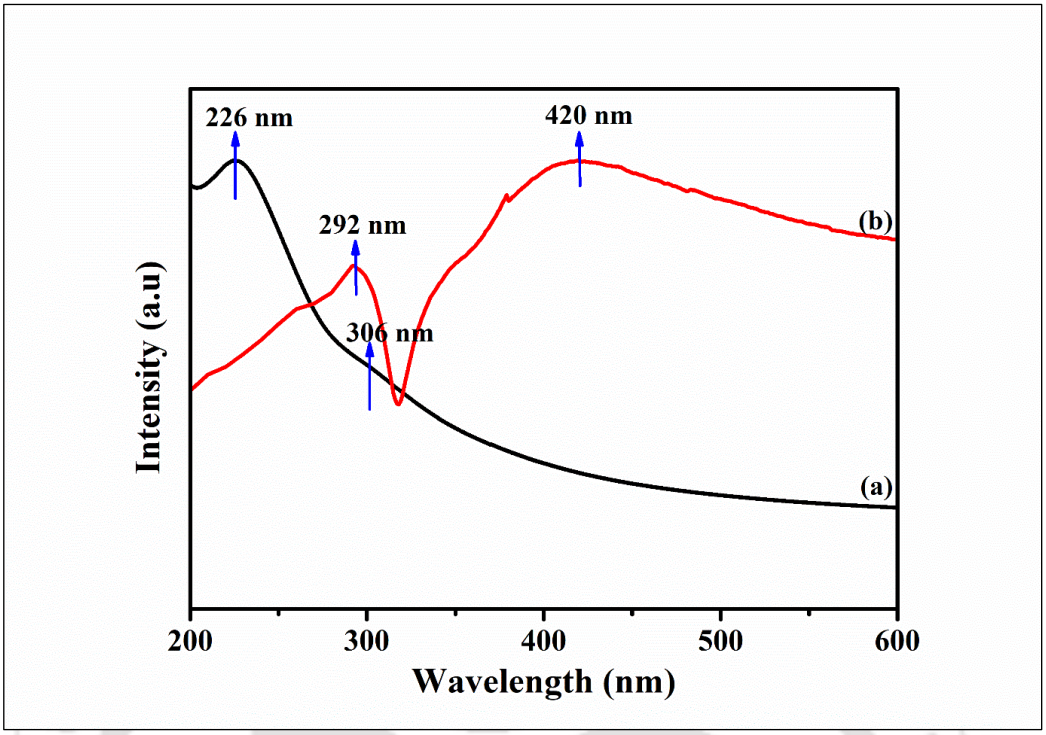

Figure 6.6: UV-Vis absorption spectra of (a) GO and (b) AgNPs/GNS hybrid nanocomposites.

This is a significant indication of the complete restoration of the electronic conjugation within the graphene sheets (Li et al., 2008b). Meanwhile, the hump which corresponds to C=O bonds of GO at 306 nm disappeared in the case of AgNPs/GNS hybrid nanocomposites and a new absorption peak at 420 nm appeared.

The appearance of this new peak at 420 nm was due to the presence of Ag nanoparticles. However, from various literature, (Zang et al., 1993) (Granbohm et al., 2018) the surface plasmon band of pure Ag nanoparticles (ca. 10 nm) fabricated with the help of a reduction process was usually found at 390 nm. But, the red shifting of the surface plasmon band of Ag nanoparticles from 390 nm to 420 nm in the case of AgNPs/GNS hybrid nanocomposites was mainly due to the influence of graphene sheets.

6.4.9 FESEM and FETEM analysis

Figure 6.7 (a, b and c) shows the FESEM image, TEM image and SAED pattern of AgNPs/GNS hybrid nanocomposites respectively. From the Figure. 6.7(a), the deposition of Ag nanoparticles on the surface of graphene sheets was visible. This insertion of Ag nanoparticles keeps the neighbouring graphene sheets discrete.

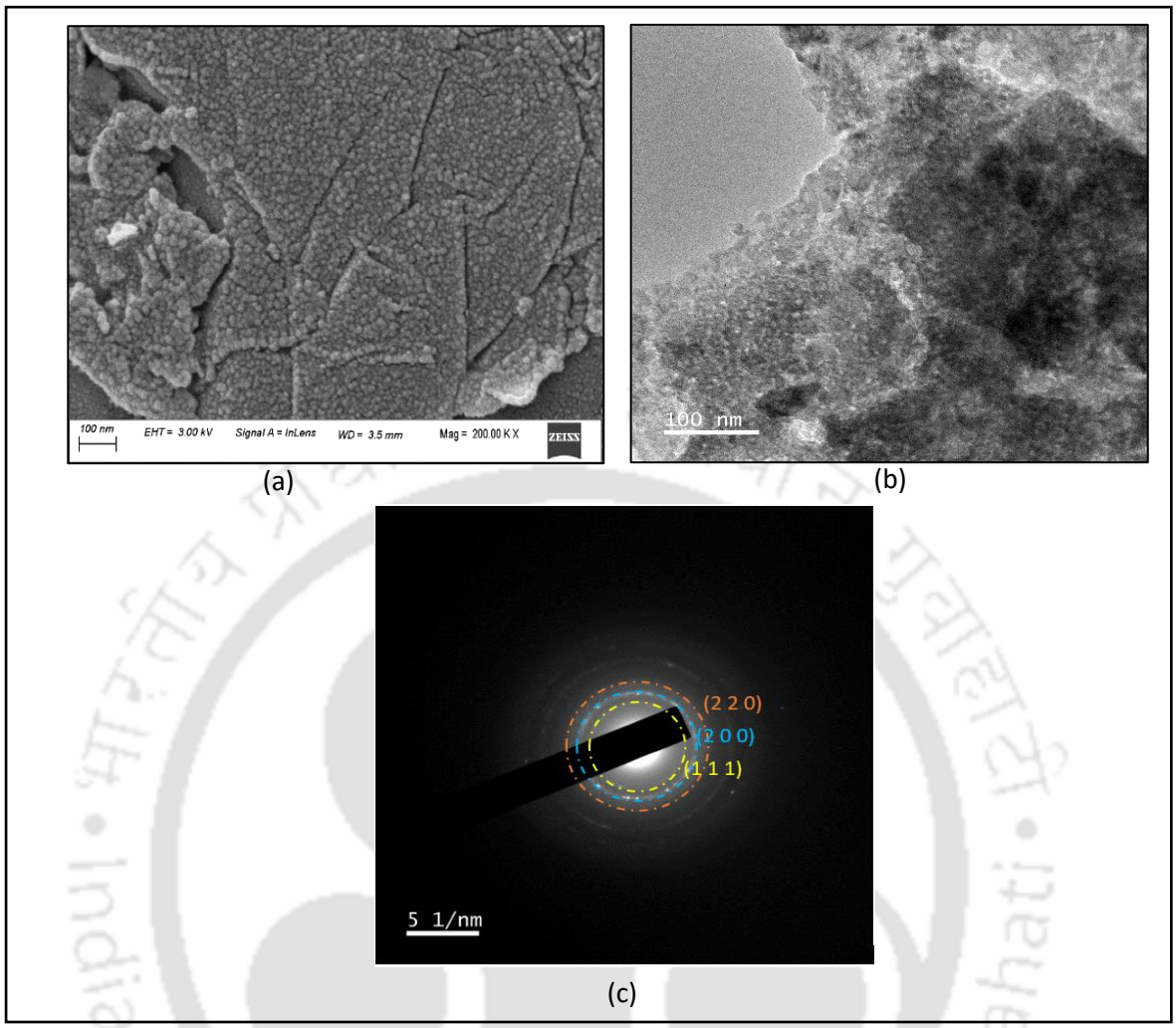

Figure 6.7: (a) FESEM image, (b) TEM image and (c) SAED pattern of silver-graphene hybrid nanocomposites.

Moreover, a frizzy and grooved morphology is clearly visible. And the shape of the Ag nanoparticles is spherical and size varies from 10-12 nm. From the typical SAED pattern Figure. 6.7(c) of the nanocomposites, we observed bright circular rings which correspond to the (1 1 1), (2 0 0) and (2 2 0) h k l planes which is similar to that of XRD analysis. This shows that the nanoparticles obtained are of crystalline Ag nanoparticles.

6.5 Conclusion

To sum up, this comprehensive analysis has provided valuable insights into the structural, morphological, and optical characteristics of silver graphene hybrid nanocomposites. XRD analysis confirmed the successful formation of metallic silver

nanoparticles within the graphene nanosheets. The congruence of the calculated d-spacing values with standard cubic Ag crystal values further supported the crystalline nature of these nanoparticles, regardless of the dosage of $AgNO_3$ used in their synthesis. Microstructural properties, including crystallite size, dislocation density, microstrain, and stacking fault probability, were also determined, providing crucial information about the quality and integrity of the nanocomposites. Raman spectroscopy revealed significant changes in the graphene structure during the synthesis process. The I_D/I_G ratio increased with each step-graphite to GO to AgNPs/GNS hybrid nanocomposites, indicating the presence of a reduction procedure of graphite and suggesting the restoration of a conjugated graphene network. The enhanced peak intensity in the Raman spectra of AgNPs/GNS hybrid nanocomposites was attributed to SERS, resulting from the strong local electromagnetic field of Ag nanoparticles and their plasmon resonance. Furthermore, FT-IR spectroscopy confirmed the reduction of GO to graphene nanosheets and the establishment of strong connections between silver nanoparticles and residual surface hydroxyl groups. UV-Vis absorption spectra revealed red-shifted peaks and the appearance of new absorption bands, indicating the successful incorporation of Ag nanoparticles into the graphene sheets. The morphological analysis through FESEM and TEM confirmed the deposition of spherical Ag nanoparticles on the graphene surface. The SAED pattern corroborated the crystalline nature of the Ag nanoparticles.

In summary, this multifaceted analysis has not only characterized the structural and morphological properties of silver graphene hybrid nanocomposites but has also shed light on the role of graphene in influencing the optical properties and surface-enhanced Raman scattering. These findings contribute to the understanding of these nanocomposites' potential applications in various fields, including sensors, catalysis, and nanoelectronics (plasmonic devices), and pave the way for further research in harnessing their unique properties for innovative technologies. Some of the potential applications of silver-graphene hybrid materials are –

- Plasmonic Devices: Utilizing the plasmonic properties of silver nanoparticles embedded in graphene matrices for applications in sensors, photodetectors, and optoelectronic devices (Paria, D. et al. 2018).

- Antibacterial Coatings: Leveraging the antibacterial properties of silver nanoparticles combined with the mechanical strength and flexibility of graphene for antimicrobial coatings in medical devices, textiles, and packaging materials (Gurunathan, S. et al. 2013).
- Catalysis: Employing silver-graphene hybrids as catalysts in various chemical reactions due to the high surface area and unique electronic properties of graphene combined with the catalytic activity of silver nanoparticles (Tran, X. T. et al. 2020).
- Flexible Electronics: Integrating silver-graphene hybrid materials into flexible and transparent electrodes for applications in flexible displays, wearable electronics, and flexible solar cells (Bae, S. et al. 2010).
- Energy Storage: Utilizing silver-graphene hybrids in electrodes for supercapacitors and batteries to enhance energy storage capacity and cycling stability (Tuichai, W. et al. 2020).
- Water Purification: Employing silver-graphene composites for water purification applications due to their excellent antibacterial properties and adsorption capabilities (Keshvardoostchokami, M. et al. 2018).

CHAPTER 7

CONCLUSION AND FUTURE PERSPECTIVE

CHAPTER 7

CONCLUSION AND FUTURE PERSPECTIVE

7.1 Conclusion

Our research aims to design and create a solid-state plasmonic energy harvesting device. To attain this goal, initially, we conducted numerical modelling using a FEM to analyze plasmonic modes and properties of noble metal nanoparticles. The simulations showed that Ag nanoparticles were more sensitive to size variations than gold, leading us to choose silver for our research. Next, we synthesized nanocrystalline TiO_2 thin films as a semiconductor substrate using Sol-Gel employing spin-coating technique. These films exhibited homogeneity, uniformity, and band gaps suitable for solar energy applications. With these preparations, we successfully fabricated solid-state plasmonic energy harvesting devices featuring a thin, tunable Ag layer as the light-absorbing material over the TiO_2 layer. Our study also explored a simplified approach called, Thermal Vapor Deposition (TVD), to deposit Ag nanoparticles over the semiconductor layers. In the final stages of our research, we developed an environmentally friendly method for synthesizing silver-graphene nanocomposites, opening new possibilities for further enhancing plasmonic device performance.

The key findings and implications of this research work are:

7.1.1 Numerical Study of Noble Metals Plasmonic Nanoparticles (Ag And Au) and its Experimental Validation

- Our exploration of plasmonic resonance in metallic nanoparticles, focusing on silver (Ag) and gold (Au) nanoparticles, has yielded valuable insights.
- The remarkable agreement between our simulations and experimental data for single isolated Ag nanoparticles demonstrates the reliability of our approach, with deviations of less than 2% in plasmonic resonance peak wavelengths.
- We have explored the effects of size and shape variations on plasmon resonance, uncovering intriguing phenomena such as red-shifting, broadening of resonance peaks, and the emergence of quadrupole resonance in larger silver nanoparticles.
- Ag nanoparticles were more sensitive to size variations than gold nanoparticles.

7.1.2 Experimental Study on Fabrication of Nanocrystalline TiO_2 Thin Films and its Characterization

- Our work introduces Sol-Gel and spin-coating technique for producing homogeneous and uniform nanocrystalline TiO_2 thin films with varying band gaps.
- The structural analyses confirm the presence of anatase-phase TiO_2, while optical analyses reveal their transparency in the visible spectrum, making them promising for solar energy harvesting devices.
- The band gap variations in these films are associated with annealing temperature and crystalline structure, opening doors for innovative applications.

7.1.3 Design and Development of TiO_2|Ag Plasmonic Solar Energy Harvesting Device

- This investigation has examined the properties of nanocrystalline TiO_2 and Ag thin films through various analytical techniques.
- We have confirmed the presence of pure anatase-phase TiO_2 in the fabricated thin films and demonstrated the formation of metallic silver nanoparticles in the Ag thin films over TiO_2.
- Structural analysis revealed essential parameters that shed light on film integrity and quality, while optical properties assessment highlighted their potential for transparent applications.
- The best-performing TiO_2|Ag plasmonic photo electric conversion device demonstrated short-circuit currents of up to 1.6 mA cm^{-2} and open-circuit voltages of approximately 440 mV, yielding an efficiency of 0.2%.
- Incorporating these films into plasmonic photoelectric conversion devices yielded promising results, hinting at the potential for cost-effective solid-state photovoltaic cells with unique photosensitizer distributions.

7.1.4 Synthesis and Characterization of Silver-Graphene Hybrid Nanocomposites

- Our comprehensive analysis has provided valuable insights into the structural, morphological, and optical characteristics of silver-graphene hybrid nanocomposites.

- The successful formation of metallic silver nanoparticles within graphene nanosheets was confirmed, regardless of the $AgNO_3$ dosage used.
- We observed changes in the graphene structure during synthesis, indicating the presence of a reduction procedure and the restoration of a conjugated graphene network.
- SERS was evident in AgNPs/GNS hybrid nanocomposites, driven by the strong local electromagnetic field of Ag nanoparticles and their plasmon resonance.
- These findings contribute to our understanding of potential applications in sensors, catalysis, and nanoelectronics such as plasmonic photo-electric conversion device, emphasizing the importance of further research in harnessing these unique properties.

In summary, this multifaceted research has expanded our understanding of plasmonic resonance, nanomaterial fabrication, and the development of innovative materials for solar energy harvesting and various other applications. These findings underscore the significance of continued exploration in these fields to advance technology, sustainability, and energy generation.

Table 7.1: Comparative analysis of our work with other previous published work.

Device Structure / Material	**Open Circuit Voltage (V_{oc}) (Volts)**	**Short Circuit Current (I_{sc}) (mA/cm^2)**	**Efficiency (η)**	**References**
ITO | Au | TiO_2	0.1	1	-	Takahashi & Tatsuma, (2011)
FTO|TiO_2|Al_2O_3|Ag	0.48	0.14	0.03%	Arquer et al.(2013)
Au@ITO|Au NR's|TiO_2	0.21	0.026	-	Mubeen et al. (2014)
TiO_2|Au|NiO	0.56 (without annealing) 0.73 (with annealing)	0.108 (without annealing) 0.04 (with annealing)	0.033% (without annealing) 0.011 (with annealing)	Nakamura et al.(2016)
ITO | Au| TiO_2	0.1	1	-	Ginsburg et al.(2018)
FTO|TiO_2|Ag	***0.44***	***1.6***	***0.2%***	***Our work***

7.2 Future Scope

Looking ahead, the future perspective of this research is highly promising. Simplified and efficient deposition methods for metallic nanoparticles, as demonstrated in this work, can contribute to the advancement of plasmonic solar cells. Continued research efforts can further optimize device architectures, explore new materials, and enhance the overall efficiency of these cells. Additionally, the combination of graphene with silver nanoparticles, as outlined in this work, opens up exciting opportunities for various applications in electronics, optics, electrochemistry, catalysis, and more.

In the coming years, researchers can focus on:

- Scaling Up Production: Efforts can be directed towards scaling up the production of these advanced materials and devices to make them accessible for practical applications.
- Material Diversification: Exploring the combination of other materials with nanoparticles and graphene to create hybrid nanocomposites with even more exceptional properties.
- Device Optimization: Further optimizing the design and performance of plasmonic solar cells to achieve higher efficiencies and stability.
- Environmental Considerations: Ensuring that the synthesis and use of these materials and devices are environmentally friendly and sustainable.
- Interdisciplinary Research: Encouraging interdisciplinary collaboration to explore a wider range of applications, including energy storage, sensors, and catalysis.

In conclusion, this research provides a significant step forward in the development of advanced materials and devices with potential transformative impacts on clean energy generation and various technological fields. The future holds exciting possibilities for continued innovation and practical implementation of these discoveries

LIST OF PUBLICATIONS

Papers

- Ksh Priyalakshmi Devi, Pranab Goswami, Harsh Chaturvedi, "Optimization of Metal Nanoparticles dimensions for Efficient Energy Harvesting Device Using Localized Surface Plasmon Resonance", Proc. of SPIE Vol. 11904 119040U-6, https://doi.org/10.1117/12.2601280

- Ksh Priyalakshmi Devi, Pranab Goswami, Harsh Chaturvedi, "Fabrication of nanocrystalline TiO2 thin films using Sol-Gel spin coating technology and investigation of its structural, morphology and optical characteristics", Applied Surface Science, Elsevier, Volume 591, 30 July 2022, https://doi.org/10.1016/j.apsusc.2022.153226

- Ksh Priyalakshmi Devi, Pranab Goswami, Harsh Chaturvedi, "Plasmon enhanced silver graphene hybrid nanocomposites and investigation of its structural, morphology and optical characteristics", Scientific Reports, Springer (under review)

- Ksh Priyalakshmi Devi, Pranab Goswami, Harsh Chaturvedi, "Energy harvesting from metal-semiconductor schottky barrier junction through hot electron injection", (manuscript under preparation)

Book Chapter

- Ksh Priyalakshmi Devi, Harsh Chaturvedi, "An overview of nanotechnology in water treatment applications and combating climate change ", Water Conservation in the Era of Global Climate Change (pp.191-212), Elsevier January 2021, http://dx.doi.org/10.1016/B978-0-12-820200-5.00004-X

Conferences

- Ksh Priyalakshmi Devi, Pranab Goswami, Harsh Chaturvedi, "Solid state Ag|TiO_2|FTO for efficient plasmonic photoelectric energy conversion ", ACS Spring

2021, https://doi.org/10.1021/scimeetings.1c00246 (President recommended symposia)

- Ksh Priyalakshmi Devi, Pranab Goswami, Harsh Chaturvedi, "Synthesis and characterization of Silver Graphene Nanocomposites for New Class of Plasmonic Photo Electric Conversion Device", 7th International Conference on Advanced Nanomaterials and Nanotechnology (ICANN2021), IIT Guwahati.

- Ksh Priyalakshmi Devi, Pranab Goswami, Harsh Chaturvedi, "Optimization of metal nanoparticle dimensions for efficient energy harvesting device using localized surface plasmon resonance"SPIE/COS Photonics Asia 10-12 October 2021 Nantong, Jiangsu, China (online mode)

- Ksh Priyalakshmi Devi, Pranab Goswami, Harsh Chaturvedi, "Green and facile synthesis of silver graphene hybrid nanocomposites and investigation of its structural, morphology and optical characteristics", 1st International Conference on Emerging trends in Science and Technology, Vedanta PG Girls College, Reengus, Sikar Rajasthan, 29th -31st March 2022.

- Ksh Priyalakshmi Devi, Pranab Goswami, Harsh Chaturvedi, "Performance analysis and optimization of a refractive index surface plasmon resonance D-type optical fibre sensor using thin films of nanocomposites", 2nd International Conference on Innovations in Clean Energy Technologies (ICET-2023) at Energy Centre, Maulana Azad National Institute of Technology, Bhopal, Madhya Pradesh, India from 8th - 10th April 2023.

Poster

- Ksh Priyalakshmi Devi, Pranab Goswami, Harsh Chaturvedi, "Metal-Insulator-Semiconductor Structure for Efficient Plasmonic Photoelectric Energy Conversion", 6th International Conference on Advanced Nanomaterial and Nanotechnology, IIT Guwahati 2019

REFERENCES

Abou-Helal, M. O., & Seeber, W. T. (2002). Preparation of TiO2 thin films by spray pyrolysis to be used as a photocatalyst. *Applied Surface Science*, *195*(1–4), 53–62. https://doi.org/10.1016/S0169-4332(02)00533-0

Alsawafta, M., Wahbeh, M., & Truong, V. Van. (2012). Plasmonic modes and optical properties of gold and silver ellipsoidal nanoparticles by the discrete dipole approximation. *Journal of Nanomaterials*, *2012*. https://doi.org/10.1155/2012/457968

Amendola, V., Bakr, O. M., & Stellacci, F. (2010). A study of the surface plasmon resonance of silver nanoparticles by the discrete dipole approximation method: Effect of shape, size, structure, and assembly. *Plasmonics*, *5*(1), 85–97. https://doi.org/10.1007/s11468-009-9120-4

Arıer, Ü. Ö. A., & Tepehan, F. Z. (2011a). Influence of heat treatment on the particle size of nanobrookite TiO2 thin films produced by sol–gel method. *Surface and Coatings Technology*, *206*(1), 37–42. https://doi.org/10.1016/j.surfcoat.2011.06.039

Arıer, Ü. Ö. A., & Tepehan, F. Z. (2011b). Influence of heat treatment on the particle size of nanobrookite TiO2 thin films produced by sol–gel method. *Surface and Coatings Technology*, *206*(1), 37–42. https://doi.org/10.1016/j.surfcoat.2011.06.039

Asano, S., & Yamamoto, G. (1975). Light Scattering by a Spheroidal Particle. *Applied Optics*, *14*(1), 29. https://doi.org/10.1364/AO.14.000029

Ashkarran, A. A., & Bayat, A. (2013). Surface plasmon resonance of metal nanostructures as a complementary technique for microscopic size measurement. *International Nano Letters*, *3*(1). https://doi.org/10.1186/2228-5326-3-50

Balandin, A. A., Ghosh, S., Bao, W., Calizo, I., Teweldebrhan, D., Miao, F., & Lau, C. N. (2008). Superior thermal conductivity of single-layer graphene. *Nano Letters*, *8*(3), 902–907. https://doi.org/10.1021/nl0731872

Barad, H.-N., Ginsburg, A., Cohen, H., Rietwyk, K. J., Keller, D. A., Tirosh, S., Bouhadana, Y., Anderson, A. Y., & Zaban, A. (2016). Hot Electron-Based Solid State TiO_2|Ag Solar Cells. *Advanced Materials Interfaces*, *3*(7), 1500789. https://doi.org/10.1002/admi.201500789

Barbé, C. J., Arendse, F., Comte, P., Jirousek, M., Lenzmann, F., Shklover, V., & Grätzel, M. (2005). Nanocrystalline Titanium Oxide Electrodes for Photovoltaic Applications. *Journal of the American Ceramic Society*, *80*(12), 3157–3171. https://doi.org/10.1111/j.1151-2916.1997.tb03245.x

Bensouici, F., Bououdina, M., Dakhel, A. A., Tala-Ighil, R., Tounane, M., Iratni, A., Souier, T., Liu, S., & Cai, W. (2017). Optical, structural and photocatalysis properties of Cu-

doped TiO 2 thin films. *Applied Surface Science*, *395*, 110–116. https://doi.org/10.1016/j.apsusc.2016.07.034

Berger, C., Wu, X., Brown, N., Naud, C., Li, X., Song, Z., Mayou, D., Li, T., Hass, J., Marchenkov, a., Conrad, E. H., First, P. N., & De Heer, W. a. (2006). Electronic Confinement and. *Science*, *312*(May), 1191–1196.

Chashechnikova, I. T., Vorotyntsev, V. M., Borovik, V. V., Golodets, G. I., Plyuto, I. V., & Shpak, A. P. (1993). Strong metal-carrier interaction in cobalt- and nickel-titanium dioxide co-hydrogenation catalysts. *Theoretical and Experimental Chemistry*, *28*(3), 176–178. https://doi.org/10.1007/BF00529413

Chenaina, H., Messaadi, C., Jalali, J., & Ezzaouia, H. (2021a). Study of structural, optical and electrical properties of SnO2 doped TiO2 thin films prepared by a facile Sol-Gel route. *Inorganic Chemistry Communications*, *124*(November 2020), 108401. https://doi.org/10.1016/j.inoche.2020.108401

Chenaina, H., Messaadi, C., Jalali, J., & Ezzaouia, H. (2021b). Study of structural, optical and electrical properties of SnO2 doped TiO2 thin films prepared by a facile Sol-Gel route. *Inorganic Chemistry Communications*, *124*. https://doi.org/10.1016/j.inoche.2020.108401

Chigane, M., Shinagawa, T., & Tani, J. ichi. (2017). Preparation of titanium dioxide thin films by indirect-electrodeposition. *Thin Solid Films*, *628*, 203–207. https://doi.org/10.1016/j.tsf.2017.03.031

Choi, H., Nahm, C., Kim, J., Moon, J., Nam, S., Jung, D. R., & Park, B. (2012). The effect of TiCl 4-treated TiO 2 compact layer on the performance of dye-sensitized solar cell. *Current Applied Physics*, *12*(3), 737–741. https://doi.org/10.1016/j.cap.2011.10.011

Clavero, C. (2014). Plasmon-induced hot-electron generation at nanoparticle/metal-oxide interfaces for photovoltaic and photocatalytic devices. *Nature Photonics*, *8*(2), 95–103. https://doi.org/10.1038/nphoton.2013.238

Cushing, S. K., Li, J., Meng, F., Senty, T. R., Suri, S., Zhi, M., Li, M., Bristow, A. D., & Wu, N. (2012). Photocatalytic Activity Enhanced by Plasmonic Resonant Energy Transfer from Metal to Semiconductor. *Journal of the American Chemical Society*, *134*(36), 15033–15041. https://doi.org/10.1021/ja305603t

Douketis, C., Wang, Z., Haslett, T. L., & Moskovits, M. (1995). Fractal character of cold-deposited silver films determined by low-temperature scanning tunneling microscopy. *Physical Review B*, *51*(16), 11022–11031. https://doi.org/10.1103/PhysRevB.51.11022

Duan, Z., Zhao, Z., Luo, D., Zhao, M., & Zhao, G. (2016). A facial approach combining photosensitive sol□gel with self-assembly method to fabricate superhydrophobic TiO2 films with patterned surface structure. *Applied Surface Science*, *360*, 1030–1035. https://doi.org/10.1016/j.apsusc.2015.11.114

Du, L., Furube, A., Hara, K., Katoh, R., & Tachiya, M. (2013). Ultrafast plasmon induced electron injection mechanism in gold–TiO2 nanoparticle system. *Journal of Photochemistry and Photobiology C: Photochemistry Reviews*, *15*, 21–30. https://doi.org/10.1016/j.jphotochemrev.2012.11.001

Dussan, A., Bohórquez, A., & Quiroz, H. P. (2017a). Effect of annealing process in TiO 2 thin films: Structural, morphological, and optical properties. *Applied Surface Science*, *424*, 111–114. https://doi.org/10.1016/j.apsusc.2017.01.269

Dussan, A., Bohórquez, A., & Quiroz, H. P. (2017b). Effect of annealing process in TiO 2 thin films: Structural, morphological, and optical properties. *Applied Surface Science*, *424*, 111–114. https://doi.org/10.1016/j.apsusc.2017.01.269

Ferrari, A. C., Meyer, J. C., Scardaci, V., Casiraghi, C., Lazzeri, M., Mauri, F., Piscanec, S., Jiang, D., Novoselov, K. S., Roth, S., & Geim, A. K. (2006). Raman spectrum of graphene and graphene layers. *Physical Review Letters*, *97*(18), 1–4. https://doi.org/10.1103/PhysRevLett.97.187401

Fisher, P., Maksimov, O., Du, H., Heydemann, V. D., Skowronski, M., & Salvador, P. A. (2006). Growth, structure, and morphology of TiO2 films deposited by molecular beam epitaxy in pure ozone ambients. *Microelectronics Journal*, *37*(12), 1493–1497. https://doi.org/10.1016/j.mejo.2006.05.010

Fox, M. (2001). *Optical properties of Solids*. Oxford University Press, New York.

Furube, A., Du, L., Hara, K., Katoh, R., & Tachiya, M. (2007). Ultrafast plasmon-induced electron transfer from gold nanodots into TiO2 nanoparticles. *Journal of the American Chemical Society*, *129*(48), 14852–14853. https://doi.org/10.1021/ja076134v

Gao, Z., Liu, N., Wu, D., Tao, W., Xu, F., & Jiang, K. (2012). Graphene-CdS composite, synthesis and enhanced photocatalytic activity. *Applied Surface Science*, *258*(7), 2473–2478. https://doi.org/10.1016/j.apsusc.2011.10.075

Gapale, D. L., Arote, S. A., Palve, B. M., & Borse, R. Y. (2018a). Influence of precursor solution concentration on the structural, optical and humidity sensing properties of spray-deposited TiO 2 thin films. *Journal of Semiconductors*, *39*(12), 122003. https://doi.org/10.1088/1674-4926/39/12/122003

Gapale, D. L., Arote, S. A., Palve, B. M., & Borse, R. Y. (2018b). Influence of precursor solution concentration on the structural, optical and humidity sensing properties of spray-deposited TiO $_2$ thin films. *Journal of Semiconductors*, *39*(12), 122003. https://doi.org/10.1088/1674-4926/39/12/122003

García de Arquer, F. P., Mihi, A., Kufer, D., & Konstantatos, G. (2013). Photoelectric Energy Conversion of Plasmon-Generated Hot Carriers in Metal–Insulator–Semiconductor Structures. *ACS Nano*, *7*(4), 3581–3588. https://doi.org/10.1021/nn400517w

García De Arquer, F. P., Mihi, A., Kufer, D., & Konstantatos, G. (2013). Photoelectric energy conversion of plasmon-generated hot carriers in metal-insulator-semiconductor structures. *ACS Nano*, *7*(4), 3581–3588. https://doi.org/10.1021/nn400517w

Geim, A. K., & Novoselov, K. S. (2007). The rise of graphene. *Nature Materials*, *6*(3), 183–191. https://doi.org/10.1038/nmat1849

Ginsburg, A., Priel, M., Barad, H. N., Keller, D. A., Borvick, E., Rietwyk, K., Kama, A., Meir, S., Anderson, A. Y., & Zaban, A. (2018). Solid state ITO|Au-NPs|TiO2 plasmonic based solar cells. *Solar Energy Materials and Solar Cells*, *179*, 254–259. https://doi.org/10.1016/j.solmat.2017.12.012

Gonçalves, M. R. (2014). Plasmonic nanoparticles: fabrication, simulation and experiments. *Journal of Physics D: Applied Physics*, *47*(21), 213001. https://doi.org/10.1088/0022-3727/47/21/213001

Govindasamy, G., Murugasen, P., & Sagadevan, S. (2016). Investigations on the Synthesis, Optical and Electrical Properties of TiO2 Thin Films by Chemical Bath Deposition (CBD) method. *Materials Research*, *19*(2), 413–419. https://doi.org/10.1590/1980-5373-MR-2015-0411

Granbohm, H., Larismaa, J., Ali, S., Johansson, L. S., & Hannula, S. P. (2018). Control of the size of silver nanoparticles and release of silver in heat treated SiO2-Ag composite powders. *Materials*, *11*(1), 1–17. https://doi.org/10.3390/ma11010080

Grimes, Craig A. Mor, G. K. (2009). *TiO 2 Nanotube Arrays*. 379.

Guo, H. L., Wang, X. F., Qian, Q. Y., Wang, F. Bin, & Xia, X. H. (2009). A green approach to the synthesis of graphene nanosheets. *ACS Nano*, *3*(9), 2653–2659. https://doi.org/10.1021/nn900227d

Haase, M. A., Qiu, J., Depuydt, J. M., & Cheng, H. (1991). Blue-green laser diodes Blue-green laser diodes. *Citation: Applied Physics Letters J. Appl. Phys. J. Vac. Sci. Technol. B Today Phys. Lett. J. Vac. Sci. Technol. B*, *591*(10), 1272–2480.

H.C. Van de Hulst. (1958). Light scattering by small particles. By H. C. van de Hulst. New York (John Wiley and Sons), London (Chapman and Hall), 1957. Pp. xiii, 470; 103 Figs.; 46 Tables. 96s. *Quarterly Journal of the Royal Meteorological Society*, *84*(360), 198–199. https://doi.org/10.1002/qj.49708436025

Hranisavljevic, J., Dimitrijevic, N. M., Wurtz, G. A., & Wiederrecht, G. P. (2002). Photoinduced charge separation reactions of J-aggregates coated on silver nanoparticles. *Journal of the American Chemical Society*, *124*(17), 4536–4537. https://doi.org/10.1021/ja012263e

Hull, R. V., Li, L., Xing, Y., & Chusuei, C. C. (2006). Pt nanoparticle binding on functionalized multiwalled carbon nanotubes. *Chemistry of Materials*, *18*(7), 1780–1788. https://doi.org/10.1021/cm0518978

Hu, W., Peng, C., Luo, W., Lv, M., Li, X., Li, D., Huang, Q., & Fan, C. (2010). Graphene-based antibacterial paper. *ACS Nano*, *4*(7), 4317–4323. https://doi.org/10.1021/nn101097v

Ivanova, N., Gugleva, V., Dobreva, M., Pehlivanov, I., Stefanov, S., & Andonova, V. (2016). Effect of Size, Shape and Environment on Optical Response of Metallic Nanoparticles. *Intech*, *i*(tourism), 13.

Jain, P. K., Huang, W., & El-Sayed, M. A. (2007). On the universal scaling behavior of the distance decay of plasmon coupling in metal nanoparticle pairs: A plasmon ruler equation. *Nano Letters*, *7*(7), 2080–2088. https://doi.org/10.1021/nl071008a

Kääriäinen, M. L., Kääriäinen, T. O., & Cameron, D. C. (2009). Titanium dioxide thin films, their structure and its effect on their photoactivity and photocatalytic properties. *Thin Solid Films*, *517*(24), 6666–6670. https://doi.org/10.1016/j.tsf.2009.05.001

Karunagaran, B., Rajendra Kumar, R. T., Mangalaraj, D., Narayandass, S. K., & Mohan Rao, G. (2002). Influence of thermal annealing on the composition and structural parameters of DC magnetron sputtered titanium dioxide thin films. *Crystal Research and Technology*, *37*(12), 1285–1292. https://doi.org/10.1002/crat.200290004

Kavita, K., & Verma, R. K. (2021). Simulation of Localized Surface Plasmon Resonance of Silver Nanoparticles with Graphene Coating Utilizing Maxwell-Garnett Theory. *Journal of Nano- and Electronic Physics*, *13*(2), 02022-1-02022–02024. https://doi.org/10.21272/jnep.13(2).02022

Kazuma, E., Sakai, N., & Tatsuma, T. (2011). Nanoimaging of localized plasmon-induced charge separation. *Chemical Communications*, *47*(20), 5777–5779. https://doi.org/10.1039/c1cc10936g

Kelly, K. L., Coronado, E., Zhao, L. L., & Schatz, G. C. (2003a). The optical properties of metal nanoparticles: The influence of size, shape, and dielectric environment. *Journal of Physical Chemistry B*, *107*(3), 668–677. https://doi.org/10.1021/jp026731y

Kelly, K. L., Coronado, E., Zhao, L. L., & Schatz, G. C. (2003b). The optical properties of metal nanoparticles: The influence of size, shape, and dielectric environment. *Journal of Physical Chemistry B*, *107*(3), 668–677. https://doi.org/10.1021/jp026731y

Khan, I., Saeed, K., & Khan, I. (2019). Nanoparticles: Properties, applications and toxicities. In *Arabian Journal of Chemistry* (Vol. 12, Issue 7, pp. 908–931). Elsevier B.V. https://doi.org/10.1016/j.arabjc.2017.05.011

Khan, R., Ali-Löytty, H., Saari, J., Valden, M., Tukiainen, A., Lahtonen, K., & Tkachenko, N. V. (2020). Optimization of Photogenerated Charge Carrier Lifetimes in ALD Grown TiO2 for Photonic Applications. *Nanomaterials*, *10*(8), 1567. https://doi.org/10.3390/nano10081567

Khlebtsov, N. G., Trachuk, L. A., & Mel'nikov, A. G. (2005a). The effect of the size, shape, and structure of metal nanoparticles on the dependence of their optical properties on the refractive index of a disperse medium. *Optics and Spectroscopy*, *98*(1), 77–83. https://doi.org/10.1134/1.1858043

Khlebtsov, N. G., Trachuk, L. A., & Mel'nikov, A. G. (2005b). The effect of the size, shape, and structure of metal nanoparticles on the dependence of their optical properties on the refractive index of a disperse medium. *Optics and Spectroscopy (English Translation of Optika i Spektroskopiya)*, *98*(1), 77–83. https://doi.org/10.1134/1.1858043

Kite, S. V, Sathe, D. J., Patil, S. S., Bhosale, P. N., & Garadkar, K. M. (2018a). Nanostructured TiO $_2$ thin films by chemical bath deposition method for high photoelectrochemical performance. *Materials Research Express*, *6*(2), 026411. https://doi.org/10.1088/2053-1591/aaed81

Kite, S. V, Sathe, D. J., Patil, S. S., Bhosale, P. N., & Garadkar, K. M. (2018b). Nanostructured TiO 2 thin films by chemical bath deposition method for high photoelectrochemical performance. *Materials Research Express*, *6*(2), 026411. https://doi.org/10.1088/2053-1591/aaed81

Kite, S. V., Sathe, D. J., Patil, S. S., Bhosale, P. N., & Garadkar, K. M. (2019). Nanostructured TiO2 thin films by chemical bath deposition method for high photoelectrochemical performance. *Materials Research Express*, *6*(2). https://doi.org/10.1088/2053-1591/aaed81

Kluczyk, K., & Jacak, W. (2016). Damping-induced size effect in surface plasmon resonance in metallic nano-particles: Comparison of RPA microscopic model with numerical finite element simulation (COMSOL) and Mie approach. *Journal of Quantitative Spectroscopy and Radiative Transfer*, *168*, 78–88. https://doi.org/10.1016/j.jqsrt.2015.08.021

Kochuveedu, S. T., Jang, Y. H., & Kim, D. H. (2013). A study on the mechanism for the interaction of light with noble metal-metal oxide semiconductor nanostructures for various photophysical applications. *Chemical Society Reviews*, *42*(21), 8467–8493. https://doi.org/10.1039/c3cs60043b

Kozioł, R., Łapiński, M., Syty, P., Koszelow, D., Sadowski, W., Sienkiewicz, J. E., & Kościelska, B. (2020). Evolution of Ag nanostructures created from thin films: UV–vis absorption and its theoretical predictions. *Beilstein Journal of Nanotechnology*, *11*, 494–507. https://doi.org/10.3762/bjnano.11.40

K. S. Novoselov et al. (2016). *Electric Field Effect in Atomically Thin Carbon Films*. *306*(5696), 666–669.

Kumar, P. M., Badrinarayanan, S., & Sastry, M. (1999). Nanocrystalline TiO 2 studied by optical, FTIR and X-ray photoelectron spectroscopy: correlation to presence of surface states. *Thin Solid Films*. www.elsevier.com/locate/tsf

Lalhriatpuia, C., Tiwari, A., Shukla, A., Tiwari, D., & Lee, S. M. (2016). Nanopillars TiO2 thin film photocatalyst application in the remediation of aquatic environment. *Korean Journal of Chemical Engineering*, *33*(12), 3367–3373. https://doi.org/10.1007/s11814-016-0191-6

Lassiter, J. B., Sobhani, H., Fan, J. A., Kundu, J., Capasso, F., Nordlander, P., & Halas, N. J. (2010). Fano resonances in plasmonic nanoclusters: Geometrical and chemical tunability. *Nano Letters*, *10*(8), 3184–3189. https://doi.org/10.1021/nl102108u

Lester, S. D., Ponce, F. A., Craford, M. G., & Steigerwald, D. A. (1995). High dislocation densities in high efficiency GaN-based light-emitting diodes. *Applied Physics Letters*, *1249*(August 1998), 1249. https://doi.org/10.1063/1.113252

Liao, C., Li, Y., & Tjong, S. C. (2020). Visible-light active titanium dioxide nanomaterials with bactericidal properties. *Nanomaterials*, *10*(1). https://doi.org/10.3390/nano10010124

Liaw, J.-W. (2006). *Simulation of surface plasmon resonance of metallic nanoparticles by the boundary-element method*.

Li, D., & Kaner, R. B. (2008). *Graphene-Based Materials*. *320*(May).

Li, D., Müller, M. B., Gilje, S., Kaner, R. B., & Wallace, G. G. (2008a). Processable aqueous dispersions of graphene nanosheets. *Nature Nanotechnology*, *3*(2), 101–105. https://doi.org/10.1038/nnano.2007.451

Li, D., Müller, M. B., Gilje, S., Kaner, R. B., & Wallace, G. G. (2008b). Processable aqueous dispersions of graphene nanosheets. *Nature Nanotechnology*, *3*(2), 101–105. https://doi.org/10.1038/nnano.2007.451

Li, J., & Liu, C. Y. (2010). Ag/Graphene heterostructures: Synthesis, characterization and optical properties. *European Journal of Inorganic Chemistry*, *8*, 1244–1248. https://doi.org/10.1002/ejic.200901048

Lind, A. C., & Greenberg, J. M. (1966). Electromagnetic Scattering by Obliquely Oriented Cylinders. *Journal of Applied Physics*, *37*(8), 3195–3203. https://doi.org/10.1063/1.1703184

Linic, S., Christopher, P., & Ingram, D. B. (2011a). Plasmonic-metal nanostructures for efficient conversion of solar to chemical energy. In *Nature Materials* (Vol. 10, Issue 12, pp. 911–921). Nature Publishing Group. https://doi.org/10.1038/nmat3151

Linic, S., Christopher, P., & Ingram, D. B. (2011b). Plasmonic-metal nanostructures for efficient conversion of solar to chemical energy. *Nature Materials*, *10*(12), 911–921. https://doi.org/10.1038/nmat3151

Liu, C., Geng, L., Xiao, T., Liu, Q., Zhang, S., Ali, H. M., Sharifpur, M., & Zhao, J. (2023). Recent advances of plasmonic nanofluids in solar harvesting and energy storage. *Journal of Energy Storage*, *72*, 108329. https://doi.org/10.1016/j.est.2023.108329

Liu, J., Liu, L., Bai, H., Wang, Y., & Sun, D. D. (2011). Gram-scale production of graphene oxide-TiO2 nanorod composites: Towards high-activity photocatalytic materials. *Applied Catalysis B: Environmental*, *106*(1–2), 76–82. https://doi.org/10.1016/j.apcatb.2011.05.007

Liu, J., Zhao, X., Duan, L., Cao, M., Sun, H., Shao, J., Chen, S., Xie, H., Chang, X., & Chen, C. (2011). Influence of annealing process on conductive properties of Nb-doped TiO2 polycrystalline films prepared by sol–gel method. *Applied Surface Science*, *257*(23), 10156–10160. https://doi.org/10.1016/j.apsusc.2011.07.009

Liu, K., Bi, Y., Qu, S., Tan, F., Chi, D., Lu, S., Li, Y., Kou, Y., & Wang, Z. (2014). Efficient hybrid plasmonic polymer solar cells with Ag nanoparticle decorated TiO2 nanorods embedded in the active layer. *Nanoscale*, *6*(11), 6180–6186. https://doi.org/10.1039/c4nr00030g

Liu, S., Tian, J., Wang, L., & Sun, X. (2011). Microwave-assisted rapid synthesis of Ag nanoparticles/graphene nanosheet composites and their application for hydrogen peroxide detection. *Journal of Nanoparticle Research*, *13*(10), 4539–4548. https://doi.org/10.1007/s11051-011-0410-3

Livraghi, S., Votta, A., Paganini, M. C., & Giamello, E. (2005). The nature of paramagnetic species in nitrogen doped TiO2 active in visible light photocatalysis. *Chemical Communications*, *4*, 498–500. https://doi.org/10.1039/b413548b

Lu, C., & Chen, X. (2021). Silver decorated graphene nanocomposites toward electrochemical energy storage. *Chemical Physics Letters*, *771*(December 2020), 138534. https://doi.org/10.1016/j.cplett.2021.138534

Lu, Q., Lu, Z., Lu, Y., Lv, L., Ning, Y., Yu, H., Hou, Y., & Yin, Y. (2013). Photocatalytic synthesis and photovoltaic application of Ag-TiO2 nanorod composites. *Nano Letters*, *13*(11), 5698–5702. https://doi.org/10.1021/nl403430x

Manisha, Kumar, V., & Kumar Sharma, D. (2021a). Fabrication of dimensional hydrophilic TiO2 nanostructured surfaces by hydrothermal method. *Materials Today: Proceedings*, *46*, 2171–2174. https://doi.org/10.1016/j.matpr.2021.02.690

Manisha, Kumar, V., & Kumar Sharma, D. (2021b). Fabrication of dimensional hydrophilic TiO2nanostructured surfaces by hydrothermal method. *Materials Today: Proceedings*, *46*, 2171–2174. https://doi.org/10.1016/j.matpr.2021.02.690

Marcano, D. C., Kosynkin, D. V., Berlin, J. M., Sinitskii, A., Sun, Z., Slesarev, A., Alemany, L. B., Lu, W., & Tour, J. M. (2010). Improved synthesis of graphene oxide. *ACS Nano*, *4*(8), 4806–4814. https://doi.org/10.1021/nn1006368

McMahon, J. M., Henry, A. I., Wustholz, K. L., Natan, M. J., Freeman, R. G., Van Duyne, R. P., & Schatz, G. C. (2009). Gold nanoparticle dimer plasmonics: Finite element method calculations of the electromagnetic enhancement to surface-enhanced raman

spectroscopy. *Analytical and Bioanalytical Chemistry*, *394*(7), 1819–1825. https://doi.org/10.1007/s00216-009-2738-4

Mie, G. (1908). Beiträge zur Optik trüber Medien, speziell kolloidaler Metallösungen. *Annalen Der Physik*, *330*(3), 377–445. https://doi.org/10.1002/andp.19083300302

Mishchenko, M. I., Hovenier, J. W., & Travis, L. D. (2000). *Light Scattering by Nonspherical Particles: Theory, Measurements, and Applications*. Academic Press.

Mohan, L., Durgalakshmi, D., Geetha, M., Sankara Narayanan, T. S. N., & Asokamani, R. (2012). Electrophoretic deposition of nanocomposite (HAp + TiO 2) on titanium alloy for biomedical applications. *Ceramics International*, *38*(4), 3435–3443. https://doi.org/10.1016/j.ceramint.2011.12.056

Morales, J., Sánchez, L., Martín, F., Ramos-Barrado, J. R., & Sánchez, M. (2004). Synthesis, Characterization, and Electrochemical Properties of Nanocrystalline Silver Thin Films Obtained by Spray Pyrolysis. *Journal of The Electrochemical Society*, *151*(1), A151. https://doi.org/10.1149/1.1632476

Mubeen, S., Lee, J., Lee, W., Singh, N., Stucky, G. D., & Moskovits, M. (2014). On the Plasmonic Photovoltaic. *ACS Nano*, *8*(6), 6066–6073. https://doi.org/10.1021/nn501379r

Nakamura, K., Oshikiri, T., Ueno, K., Wang, Y., Kamata, Y., Kotake, Y., & Misawa, H. (2016a). Properties of Plasmon-Induced Photoelectric Conversion on a TiO $_2$ /NiO p–n Junction with Au Nanoparticles. *The Journal of Physical Chemistry Letters*, *7*(6), 1004–1009. https://doi.org/10.1021/acs.jpclett.6b00291

Nakamura, K., Oshikiri, T., Ueno, K., Wang, Y., Kamata, Y., Kotake, Y., & Misawa, H. (2016b). Properties of Plasmon-Induced Photoelectric Conversion on a TiO2/NiO p-n Junction with Au Nanoparticles. *Journal of Physical Chemistry Letters*, *7*(6), 1004–1009. https://doi.org/10.1021/acs.jpclett.6b00291

Nanoclusters, D. S., Sun, X., Dong, S., & Wang, E. (2004). One-Step Preparation and Characterization of Poly (propyleneimine). *Macromolecules*, *37*, 7105–7108.

Nethravathi, C., & Rajamathi, M. (2008). Chemically modified graphene sheets produced by the solvothermal reduction of colloidal dispersions of graphite oxide. *Carbon*, *46*(14), 1994–1998. https://doi.org/10.1016/j.carbon.2008.08.013

Nishijima, Y., Ueno, K., Kotake, Y., Murakoshi, K., Inoue, H., & Misawa, H. (2012). Near-Infrared Plasmon-Assisted Water Oxidation. *The Journal of Physical Chemistry Letters*, *3*(10), 1248–1252. https://doi.org/10.1021/jz3003316

Nishijima, Y., Ueno, K., Yokota, Y., Murakoshi, K., & Misawa, H. (2010). Plasmon-assisted photocurrent generation from visible to near-infrared wavelength using a Au-nanorods/TiO2 electrode. *Journal of Physical Chemistry Letters*, *1*(13), 2031–2036. https://doi.org/10.1021/jz1006675

Noguez, C. (2007). Surface plasmons on metal nanoparticles: The influence of shape and physical environment. *Journal of Physical Chemistry C*, *111*(10), 3606–3619. https://doi.org/10.1021/jp066539m

Ohsaka, T., Izumi, F., & Fujiki, Y. (1978). Raman spectrum of anatase, TiO2. *Journal of Raman Spectroscopy*, *7*(6), 321–324. https://doi.org/10.1002/jrs.1250070606

Oh, S. H., Kim, D. J., Hahn, S. H., & Kim, E. J. (2003). Comparison of optical and photocatalytic properties of TiO2 thin films prepared by electron-beam evaporation and sol–gel dip-coating. *Materials Letters*, *57*(26–27), 4151–4155. https://doi.org/10.1016/S0167-577X(03)00281-7

Okuya, M., Prokudina, N. A., Mushika, K., & Kaneko, S. (1999). TiO2 thin films synthesized by the spray pyrolysis deposition (SPD) technique. *Journal of the European Ceramic Society*, *19*(6–7), 903–906. https://doi.org/10.1016/S0955-2219(98)00341-0

Paredes, J. I., Villar-Rodil, S., Martínez-Alonso, A., & Tascón, J. M. D. (2008). Graphene oxide dispersions in organic solvents. *Langmuir*, *24*(19), 10560–10564. https://doi.org/10.1021/la801744a

Pasricha, R., Gupta, S., & Srivastava, A. K. (2009). A facile and novel synthesis of Ag-graphene-based nanocomposites. *Small (Weinheim an Der Bergstrasse, Germany)*, *5*(20), 2253–2259. https://doi.org/10.1002/smll.200900726

Pathak, N. K. (2020). Plasmonic Nanostructures for Energy Application. *Frontiers in Mechanical Engineering*, *6*. https://doi.org/10.3389/fmech.2020.00053

Patrocínio, A. O. T., Paniago, E. B., Paniago, R. M., & Iha, N. Y. M. (2008). XPS characterization of sensitized n-TiO 2 thin films for dye-sensitized solar cell applications. *Applied Surface Science*, *254*(6), 1874–1879. https://doi.org/10.1016/j.apsusc.2007.07.185

P. B. Johnson and R. W. Christy. (1972). Optical Constant of the Nobel Metals. *Physical Review B*, *6*(12), 4370–4379.

Pfeifer, V., Erhart, P., Li, S., Rachut, K., Morasch, J., Brötz, J., Reckers, P., Mayer, T., Rühle, S., Zaban, A., Mora Seró, I., Bisquert, J., Jaegermann, W., & Klein, A. (2013). Energy Band Alignment between Anatase and Rutile TiO $_2$. *The Journal of Physical Chemistry Letters*, *4*(23), 4182–4187. https://doi.org/10.1021/jz402165b

Pomoni, K., Vomvas, A., & Trapalis, Chr. (2005). Transient photoconductivity of nanocrystalline TiO2 sol–gel thin films. *Thin Solid Films*, *479*(1–2), 160–165. https://doi.org/10.1016/j.tsf.2004.12.005

Pradhan, A. K., Holloway, T., Mundle, R., Dondapati, H., & Bahoura, M. (2012). Energy harvesting in semiconductor-insulator-semiconductor junctions through excitation of surface plasmon polaritons. *Applied Physics Letters*, *100*(6). https://doi.org/10.1063/1.3684833

Priyalakshmi Devi, K., Goswami, P., & Chaturvedi, H. (2022). Fabrication of nanocrystalline TiO2 thin films using Sol-Gel spin coating technology and investigation of its structural, morphology and optical characteristics. *Applied Surface Science*, *591*(March), 153226. https://doi.org/10.1016/j.apsusc.2022.153226

Qian, Y., Wang, C., & Le, Z. G. (2011). Decorating graphene sheets with Pt nanoparticles using sodium citrate as reductant. *Applied Surface Science*, *257*(24), 10758–10762. https://doi.org/10.1016/j.apsusc.2011.07.093

Qin, L., Wang, G., & Tan, Y. (2018). Plasmonic Pt nanoparticles—TiO2 hierarchical nano-architecture as a visible light photocatalyst for water splitting. *Scientific Reports*, *8*(1), 1–13. https://doi.org/10.1038/s41598-018-33795-z

Quan, X., Yang, S., Ruan, X., & Zhao, H. (2005). Preparation of titania nanotubes and their environmental applications as electrode. *Environmental Science and Technology*, *39*(10), 3770–3775. https://doi.org/10.1021/es048684o

Quiroz, H. P., & Dussan, A. (2016a). Synthesis of self-organized TiO2 nanotube arrays: Microstructural, stereoscopic, and topographic studies. *Journal of Applied Physics*, *120*(5). https://doi.org/10.1063/1.4958940

Quiroz, H. P., & Dussan, A. (2016b). Synthesis of self-organized TiO2 nanotube arrays: Microstructural, stereoscopic, and topographic studies. *Journal of Applied Physics*, *120*(5). https://doi.org/10.1063/1.4958940

Rajendra Prasad, M. B., Tamboli, P. S., Bhalekar, V. P., Kadam, V., Abraham, J. T., Rajesh, C., & Pathan, H. M. (2018). Impact of composition of polysulphide electrolyte on the photovoltaic performance in quantum dot sensitized solar cells. *Materials Research Express*, *5*(6). https://doi.org/10.1088/2053-1591/aacdb5

Ranjitha, A., Muthukumarasamy, N., Thambidurai, M., Balasundaraprabhu, R., & Agilan, S. (2013a). Effect of annealing temperature on nanocrystalline TiO2 thin films prepared by sol–gel dip coating method. *Optik*, *124*(23), 6201–6204. https://doi.org/10.1016/j.ijleo.2013.04.085

Ranjitha, A., Muthukumarasamy, N., Thambidurai, M., Balasundaraprabhu, R., & Agilan, S. (2013b). Effect of annealing temperature on nanocrystalline TiO2 thin films prepared by sol–gel dip coating method. *Optik*, *124*(23), 6201–6204. https://doi.org/10.1016/j.ijleo.2013.04.085

Raza, S., Kadkhodazadeh, S., Christensen, T., Di Vece, M., Wubs, M., Mortensen, N. A., & Stenger, N. (2015). Multipole plasmons and their disappearance in few-nanometre silver nanoparticles. *Nature Communications*, *6*(May). https://doi.org/10.1038/ncomms9788

Risović, D., Poljaček, S. M., Furić, K., & Gojo, M. (2008). Inferring fractal dimension of rough/porous surfaces-A comparison of SEM image analysis and electrochemical impedance spectroscopy methods. *Applied Surface Science*, *255*(5 PART 2), 3063–3070. https://doi.org/10.1016/j.apsusc.2008.08.106

Sampaio, M. J., Silva, C. G., Marques, R. R. N., Silva, A. M. T., & Faria, J. L. (2011). Carbon nanotube-TiO2 thin films for photocatalytic applications. *Catalysis Today*, *161*(1), 91–96. https://doi.org/10.1016/j.cattod.2010.11.081

Sarwar, S., Park, S., Dao, T. T., Lee, M. soo, Ullah, A., Hong, S., & Han, C. H. (2020). Scalable photoelectrochromic glass of high performance powered by ligand attached TiO2 photoactive layer. *Solar Energy Materials and Solar Cells*, *210*(January), 110498. https://doi.org/10.1016/j.solmat.2020.110498

Scherrer, P. (1918a). Bestimmung der Größe und der inneren Struktur von Kolloidteilchen mittels Röntgenstrahlen. *Nachrichten von Der Gesellschaft Der Wissenschaften Zu Göttingen, Mathematisch-Physikalische Klasse*, *1918*, 98–100.

Scherrer, P. (1918b). Bestimmung der Größe und der inneren Struktur von Kolloidteilchen mittels Röntgenstrahlen. *Nachrichten von Der Gesellschaft Der Wissenschaften Zu Göttingen, Mathematisch-Physikalische Klasse*, *1918*, 98–100.

Sen, S., Mahanty, S., Roy, S., Heintz, O., Bourgeois, S., & Chaumont, D. (2005). Investigation on sol–gel synthesized Ag-doped TiO2 cermet thin films. *Thin Solid Films*, *474*(1–2), 245–249. https://doi.org/10.1016/j.tsf.2004.04.004

Senthil, T. S., Muthukumarasamy, N., Agilan, S., Thambidurai, M., & Balasundaraprabhu, R. (2010). Preparation and characterization of nanocrystalline TiO2 thin films. *Materials Science and Engineering B: Solid-State Materials for Advanced Technology*, *174*(1–3), 102–104. https://doi.org/10.1016/j.mseb.2010.04.009

Shams-Nateri, A., Kazemian, S., & Piri, N. (2020). Nano-TiO2 coated cotton fabrics with temperature regulating properties. *Journal of the Textile Institute*, *111*(8), 1223–1230. https://doi.org/10.1080/00405000.2019.1690916

Shen, J., Shi, M., Li, N., Yan, B., Ma, H., Hu, Y., & Ye, M. (2010). Facile synthesis and application of Ag-chemically converted graphene nanocomposite. *Nano Research*, *3*(5), 339–349. https://doi.org/10.1007/s12274-010-1037-x

Şilik, E., Pat, S., Özen, S., Mohammadigharehbagh, R., Yudar, H. H., Musaoğlu, C., & Korkmaz, Ş. (2017). Electrochromic properties of TiO 2 thin films grown by thermionic vacuum arc method. *Thin Solid Films*, *640*, 27–32. https://doi.org/10.1016/j.tsf.2017.07.073

Sivaprakash, V., & Narayanan, R. (2020). Synthesis of TiO2 nanotubes via electrochemical anodization with different water content. *Materials Today: Proceedings*, *37*(Part 2), 142–146. https://doi.org/10.1016/j.matpr.2020.04.657

Sivaprakash, V., & Narayanan, R. (2021). Synthesis of TiO2 nanotubes via electrochemical anodization with different water content. *Materials Today: Proceedings*, *37*, 142–146. https://doi.org/10.1016/j.matpr.2020.04.657

Soldano, C., Mahmood, A., & Dujardin, E. (2010). Production, properties and potential of graphene. *Carbon*, *48*(8), 2127–2150. https://doi.org/10.1016/j.carbon.2010.01.058

Sönmezoğlu, S., Çankaya, G., & Serin, N. (2012). Influence of annealing temperature on structural, morphological and optical properties of nanostructured TiO_2 thin films. *Materials Technology*, *27*(3), 251–256. https://doi.org/10.1179/1753555712Y.0000000008

Sönnichsen, C., Franzl, T., Wilk, T., von Plessen, G., Feldmann, J., Wilson, O., & Mulvaney, P. (2002). Drastic Reduction of Plasmon Damping in Gold Nanorods. *Physical Review Letters*, *88*(7), 077402. https://doi.org/10.1103/PhysRevLett.88.077402

Sosa, I. O., Noguez, C., & Barrera, R. G. (2003a). Optical properties of metal nanoparticles with arbitrary shapes. *Journal of Physical Chemistry B*, *107*(26), 6269–6275. https://doi.org/10.1021/jp0274076

Stankovich, S., Dikin, D. A., Piner, R. D., Kohlhaas, K. A., Kleinhammes, A., Jia, Y., Wu, Y., Nguyen, S. B. T., & Ruoff, R. S. (2007). Synthesis of graphene-based nanosheets via chemical reduction of exfoliated graphite oxide. *Carbon*, *45*(7), 1558–1565. https://doi.org/10.1016/j.carbon.2007.02.034

Sun, H., Wang, C., Pang, S., Li, X., Tao, Y., Tang, H., & Liu, M. (2008). Photocatalytic TiO2 films prepared by chemical vapor deposition at atmosphere pressure. *Journal of Non-Crystalline Solids*, *354*(12–13), 1440–1443. https://doi.org/10.1016/j.jnoncrysol.2007.01.108

Takahashi, Y., & Tatsuma, T. (2010). Electrodeposition of thermally stable gold and silver nanoparticle ensembles through a thin alumina nanomask. *Nanoscale*, *2*(8), 1494–1499. https://doi.org/10.1039/c0nr00230e

Takahashi, Y., & Tatsuma, T. (2011). Solid state photovoltaic cells based on localized surface plasmon-induced charge separation. *Applied Physics Letters*, *99*(18). https://doi.org/10.1063/1.3659476

Tian, G., Dong, L., Wei, C., Huang, J., He, H., & Shao, J. (2006). Investigation on microstructure and optical properties of titanium dioxide coatings annealed at various temperature. *Optical Materials*, *28*(8–9), 1058–1063. https://doi.org/10.1016/j.optmat.2005.06.007

Tian, Y., & Tatsuma, T. (2004). Plasmon-induced photoelectrochemistry at metal nanoparticles supported on nanoporous TiO2. *Chemical Communications*, *16*, 1810. https://doi.org/10.1039/b405061d

Tian, Y., & Tatsuma, T. (2005). Mechanisms and Applications of Plasmon-Induced Charge Separation at TiO_2 Films Loaded with Gold Nanoparticles. *Journal of the American Chemical Society*, *127*(20), 7632–7637. https://doi.org/10.1021/ja042192u

Trapalis, C., Todorova, N., Anastasescu, M., Anastasescu, C., Stoica, M., Gartner, M., Zaharescu, M., & Stoica, T. (2009). Atomic force microscopy study of TiO2 sol–gel films thermally treated under NH3 atmosphere. *Thin Solid Films*, *517*(23), 6243–6247. https://doi.org/10.1016/j.tsf.2009.02.070

Vishwas, M., Narasimha Rao, K., & Chakradhar, R. P. S. (2012a). Influence of annealing temperature on Raman and photoluminescence spectra of electron beam evaporated TiO2 thin films. *Spectrochimica Acta Part A: Molecular and Biomolecular Spectroscopy*, *99*, 33–36. https://doi.org/10.1016/j.saa.2012.09.009

Vishwas, M., Narasimha Rao, K., & Chakradhar, R. P. S. (2012b). Influence of annealing temperature on Raman and photoluminescence spectra of electron beam evaporated TiO2 thin films. *Spectrochimica Acta - Part A: Molecular and Biomolecular Spectroscopy*, *99*, 33–36. https://doi.org/10.1016/j.saa.2012.09.009

Voisin, C., Christofilos, D., Del Fatti, N., & Vallée, F. (2001). Femtosecond surface plasmon resonance dynamics and electron-electron interactions in silver nanoparticles. *The European Physical Journal D*, *16*(1), 139–144. https://doi.org/10.1007/s100530170078

Wang, J., Zhao, Y., Xu, X., Feng, X., Yu, J., & Li, T. (2015a). A facile interfacial assembling strategy for synthesizing yellow TiO $_2$ flakes with a narrowed bandgap. *RSC Advances*, *5*(72), 58176–58183. https://doi.org/10.1039/C5RA08101G

Wang, J., Zhao, Y., Xu, X., Feng, X., Yu, J., & Li, T. (2015b). A facile interfacial assembling strategy for synthesizing yellow TiO 2 flakes with a narrowed bandgap . *RSC Advances*, *5*(72), 58176–58183. https://doi.org/10.1039/c5ra08101g

Wang, X., Wu, G., Zhou, B., & Shen, J. (2013). Thermal annealing effect on optical properties of binary TiO2-SiO2 sol-gel coatings. *Materials*, *6*(1), 76–84. https://doi.org/10.3390/ma6010076

Xu, C., Wang, X., & Zhu, J. (2008). Graphene - Metal particle nanocomposites. *Journal of Physical Chemistry C*, *112*(50), 19841–19845. https://doi.org/10.1021/jp807989b

Yahiya, L. Z., Dhahir, M. K., & Faris, R. A. (2021). *Fabrication and characterization of zinc oxide nanorods coated by graphene oxide ZnO-NR@GO as a potential hybrid material photocatalyst*. 100006. https://doi.org/10.1063/5.0066062

Yakovlev, V. V., Scarel, G., Aita, C. R., & Mochizuki, S. (2000). Short-range order in ultrathin film titanium dioxide studied by Raman spectroscopy. *Applied Physics Letters*, *76*(9), 1107–1109. https://doi.org/10.1063/1.125953

Yang, J., Zang, C., Sun, L., Zhao, N., & Cheng, X. (2011). Synthesis of graphene/Ag nanocomposite with good dispersibility and electroconductibility via solvothermal method. *Materials Chemistry and Physics*, *129*(1–2), 270–274. https://doi.org/10.1016/j.matchemphys.2011.04.002

Yu, J., Li, L., Qian, Y., Lou, H., Yang, D., & Qiu, X. (2018). Facile and Green Preparation of High UV-Blocking Lignin/Titanium Dioxide Nanocomposites for Developing Natural Sunscreens. *Industrial and Engineering Chemistry Research*, *57*(46), 15740–15748. https://doi.org/10.1021/acs.iecr.8b04101

Yun, J., Hwang, S. H., & Jang, J. (2015). Fabrication of Au@Ag core/shell nanoparticles decorated TiO2 hollow structure for efficient light-harvesting in dye-sensitized solar cells. *ACS Applied Materials and Interfaces*, *7*(3), 2055–2063. https://doi.org/10.1021/am508065n

Zahn, W., & Zösch, A. (1999). The dependence of fractal dimension on measuring conditions of scanning probe microscopy. *Fresenius' Journal of Analytical Chemistry*, *365*(1–3), 168–172. https://doi.org/10.1007/s002160051466

Zang, L., Liu, C.-Y., & Ren, X.-M. (1993). Adsorption of carbonate and bicarbonate on colloidal silver particles and accompanying optical effects. *Journal of Photochemistry and Photobiology A: Chemistry*, *74*(2–3), 267–271. https://doi.org/10.1016/1010-6030(93)80125-S

Zhang, M., Xiang, H., Zhang, X., & Lu, G. (2015). *Quantum Electrodynamics and Plasmonic Resonance of Metallic Nanostructures*.

Zhao, J., Pei, S., Ren, W., Gao, L., & Cheng, H. M. (2010). Efficient preparation of large-area graphene oxide sheets for transparent conductive films. *ACS Nano*, *4*(9), 5245–5252. https://doi.org/10.1021/nn1015506

Zhao, J., Pinchuk, A. O., McMahon, J. M., Li, S., Ausman, L. K., Atkinson, A. L., & Schatz, G. C. (2008). Methods for describing the electromagnetic properties of silver and gold nanoparticles. *Accounts of Chemical Research*, *41*(12), 1710–1720. https://doi.org/10.1021/ar800028j

Zhao, L., & Lu, J. (2017). Fabrication and application of mesoporous TiO2 film coated on Al wire by sol-gel method with EISA. *Applied Surface Science*, *402*, 369–371. https://doi.org/10.1016/j.apsusc.2017.01.023

Zhou, G., Wang, D. W., Li, F., Zhang, L., Li, N., Wu, Z. S., Wen, L., Lu, G. Q., & Cheng, H. M. (2010). Graphene-wrapped Fe3O4 anode material with improved reversible capacity and cyclic stability for lithium ion batteries. *Chemistry of Materials*, *22*(18), 5306–5313. https://doi.org/10.1021/cm101532x

Singh, S. V., Hazra, S., Dahiya, S., Pandey, U., Biring, S., & Pal, B. N. (2024). Plasmonic hot-electron induced narrowband photodetector by using in-situ grown Ag/TiO2 nano-heterojunction thin films. *Optical Materials*, *148*, 114874. https://doi.org/10.1016/j.optmat.2024.114874

Song, J., Long, J., Liu, Y., Xu, Z., Ge, A., Piercy, B. D., Cullen, D. A., Ivanov, I. N., McBride, J. R., Losego, M. D., & Lian, T. (2021). Highly Efficient Plasmon Induced Hot-Electron

Transfer at Ag/TiO $_2$ Interface. *ACS Photonics*, *8*(5), 1497–1504. https://doi.org/10.1021/acsphotonics.1c00321

Liu, C., Geng, L., Xiao, T., Liu, Q., Zhang, S., Ali, H. M., ... & Zhao, J. (2023). Recent advances of plasmonic nanofluids in solar harvesting and energy storage. *Journal of Energy Storage*, *72*, 108329

Paria, D., Jeong, H. H., Vadakkumbatt, V., Deshpande, P., Fischer, P., Ghosh, A., & Ghosh, A. (2018). Graphene–silver hybrid devices for sensitive photodetection in the ultraviolet. *Nanoscale*, *10*(16), 7685-7693.

Gurunathan, S., Han, J. W., Dayem, A. A., Eppakayala, V., Park, M. R., Kwon, D. N., & Kim, J. H. (2013). Antibacterial activity of dithiothreitol reduced graphene oxide. *Journal of industrial and engineering chemistry*, *19*(4), 1280-1288.

Tran, X. T., Hussain, M., & Kim, H. T. (2020). Facile and fast synthesis of a reduced graphene oxide/carbon nanotube/iron/silver hybrid and its enhanced performance in catalytic reduction of 4–nitrophenol. *Solid State Sciences*, *100*, 106107.

Bae, S., Kim, H., Lee, Y., Xu, X., Park, J. S., Zheng, Y., ... & Iijima, S. (2010). Roll-to-roll production of 30-inch graphene films for transparent electrodes. *Nature nanotechnology*, *5*(8), 574-578.

Tuichai, W., Karaphun, A., & Ruttanapun, C. (2020). Ag nanomaterials deposited reduced graphene oxide nanocomposite as an advanced hybrid electrode material for Asymmetric Supercapacitor device. *Journal of Alloys and Compounds*, *849*, 156516.

Keshvardoostchokami, M., Bigverdi, P., Zamani, A., Parizanganeh, A., & Piri, F. (2018). Silver@ graphene oxide nanocomposite: synthesize and application in removal of imidacloprid from contaminated waters. *Environmental Science and Pollution Research*, *25*, 6751-6761.